DISS. ETH NO. 21558

Characterizing and Correcting for Imperfect Field Dynamics in Magnetic Resonance Imaging

A dissertation submitted to

ETH ZURICH

for the degree of

Doctor of Sciences

presented by

Signe Johanna Vannesjö

Master of Science in Engineering

Royal Institute of Technology, Stockholm, Sweden

born on November 2nd, 1981

citizen of Sweden

accepted on the recommendation of

Prof. Dr. Klaas P. Pruessmann
Prof. Dr. Robert Turner

2013

Den mätta dagen, den är aldrig störst,
Den bästa dagen är en dag av törst.
Nog finns det mål och mening i vår färd –
men det är vägen, som är mödan värd.

Karin Boye

To my grandparents,
Karin and Erik Lundblad

Table of Contents

Summary

Magnetic Resonance Imaging relies on a stable and homogenous background field upon which time-varying gradient fields are superposed for the encoding of spatial information and signal contrast. Slight deviations to the time-courses of the added gradient fields or fluctuations in the background field can severely disturb the signal encoding. This often results in artifacts and can be detrimental for sensitive applications. Despite ever improving hardware, field imperfections remain a challenge and they are commonly addressed either by application-dependent correction techniques or sequence-by-sequence field measurements. The former, however, generally have a limited domain of applicability and the latter requires specialized field sensors or additional calibration scans. In this thesis, the main focus has been on developing a more generic approach to characterize and correct for reproducible field imperfections. Additionally, non-reproducible field fluctuations caused by subject motion were addressed using concurrent field monitoring.

Gradient and shim system characterization
A first part of this thesis is dedicated to the characterization of gradient and shim field dynamics based on modeling the systems as linear and time-invariant (LTI). An LTI system is fully determined by its impulse response function. In order to measure the gradient or shim impulse response function (GIRF or SIRF), the system is probed with a set of known input pulses and the resulting field responses in the scanner bore

are measured. Field measurements were here performed with a 3rd-order dynamic field camera, based on NMR field probes. A GIRF estimate can then be obtained by a frequency-domain division of the measured response by the known input. Knowing the GIRF of a system, the field response to any input sequence can be predicted, to the degree that the system behaves as an LTI system. The predictions can also include cross-term fields if they were contained in the GIRF measurements.

Care has to be taken in the choice of input pulses to probe the system with, as the noise propagation into the measured GIRFs highly depends on the frequency content of the input pulses. To this purpose, properties of different classes of input functions have been analyzed. In a first approach a combination of short block pulses were used for system characterization. The block pulses are easy to implement on most systems, and a combination of pulses of different lengths can be utilized for a broadband system characterization. More suitable for probing a system over a wide bandwidth, however, is to use frequency-swept pulses. The frequency-swept pulses can be construed to contain arbitrary input energy distributed over any given bandwidth given a sufficient length of the pulse. Based on this property, it was shown that frequency-swept pulses can be designed to achieve any targeted sensitivity profile in the system characterization.

A set of triangular input pulses was used to characterize the gradient performance of a commercial 3T system. A number of system features could be read from the measured GIRFs, such as response bandwidth, low-frequency group delay and oscillatory responses due to coil vibrations. Based on the measured GIRFs the field responses to different input pulses were predicted and compared with directly measured results. The field predictions were shown to agree well with measurements for a set of block pulses and a full echo-planar imaging trajectory.

Furthermore, a broadband characterization of the higher-order shim system of a whole-body 7T scanner was performed using frequency-swept pulses as inputs. For unshielded shim channels, the measured shim impulse response functions (SIRFs) showed a sharp peak centered at zero frequency, representing long-living eddy currents. Moreover, a complicated pattern of resonances and significant responses in cross-term fields were observed. It was shown that shim field

responses to different input pulses could be well predicted by the measured SIRFs, also in the cross-terms.

Pre-emphasis

To some degree, effects of field imperfections can be accounted for with post-acquisitions data correction techniques. This is, however, not applicable e.g. in cases of through-plane dephasing or distorted excitation geometry, stressing the importance of achieving high accuracy in the actual field waveforms. It has long been standard to counteract unwanted field effects from eddy currents by passing the input through a pre-emphasis filter. Typically, the filter has been based on a sum of exponential field terms. Such a model does however not account for the full complexity of field perturbations. Here, novel approaches to pre-emphasis, based on the LTI system characterization described above, have been explored. In one approach, broadband digital pre-emphasis filters were constructed based on the inverse of measured SIRFs. This has the advantage of yielding high flexibility in the design of the resulting system frequency response. The approach has been extended to include also cross-term compensation, by applying pre-emphasis filters between inputs of different field channels. This was shown to considerably suppress frequency-dependent spatially linear field responses to inputs in higher-order shim channels.

The concept of passing the input through a fixed pre-emphasis filter does, however, not necessarily yield the optimal field waveform accuracy the system could be capable of for all inputs. The task of finding the optimal input given a known system frequency response and a set of time-domain hardware constraints, such as amplitude limitations, is inherently a sequence-by-sequence optimization problem. Different formulations of the problem are applicable for different objectives. Here, a few practically useful problem formulations are shown and an iterative optimization algorithm for finding a solution is implemented. It is demonstrated that this can yield improved accuracy for common k-space trajectories on a system with standard eddy current compensation.

GIRF-based image reconstruction

MRI applications relying on fast imaging techniques suffer disproportionately from imperfect gradient waveforms, due to the high demands on the gradient system. If the actual gradient waveforms are known, however, it is generally possible to correct for field deviations in the image reconstruction. As a continuation of the gradient system characterization approach, the feasibility of performing image reconstruction based on GIRF-predicted k-space trajectories was here investigated. Phantom and *in vivo* echo-planar imaging data from a 3T system was reconstructed based on nominal, GIRF-predicted and directly measured trajectories, comparing the resulting images. It was found that reconstruction based on GIRF-predicted trajectories nearly eliminated ghosting and yielded comparable image quality to concurrently monitored trajectories. The technique is not limited to particular k-space sampling patterns and could work as a one-time system calibration.

Physiological field fluctuations

Finally, the effects of non-reproducible field perturbations stemming from subject motion were investigated. It has previously been observed that field fluctuations caused by breathing and limb motion can affect the quality of brain images at high fields. Here the effects of physiological field perturbations on high-resolution T2*-weighted brain images at 7T were examined and a correction technique based on concurrent field monitoring was implemented. The field perturbations yielded artifacts in the form of ghosting, blurring and stripes of intensity modulation over the images. It was shown that artifacts were greatly reduced by including monitored field fluctuations in the image reconstruction. In most cases, a correction based on measured fields up to first-order spherical harmonics was sufficient. Occasionally, however, further visible improvement in the images could be observed when including also measured higher-order fields in the reconstruction.

Conclusion

In conclusion, gradient and shim field dynamics have been characterized based on an assumption of system linearity and time-invariance. The characterization is a fast and easy procedure, and encompasses a

majority of effects influencing field waveforms. It was shown that it could be used to improve pre-emphasis and to correct for field imperfections in the image reconstruction. The approach thus has the potential to reduce the impact of suboptimal field dynamics, which is a long-standing issue in MRI. Non-reproducible field fluctuations, such as caused by subject motion, can be addressed with concurrent field monitoring, as further explored in this work.

Zusammenfassung

Kernspintomographie (Magnetic Resonance Imaging) erfordert für die Kodierung von räumlicher Information und Signalkontrast als Basis ein stabiles und homogenes Magnetfeld, dem dynamische Magnetfeld-Gradienten überlagert werden. Schon kleine Abweichungen vom geforderten zeitlichen Verlauf der Gradientenfelder oder Fluktuationen des Basisfeldes können die Signalkodierung erheblich stören. Solche Unregelmässigkeiten führen oft zu Artefakten, die empfindliche Anwendungen nachteilig beeinflussen. Trotz der ständigen Verbesserungen von Kernspinresonanz Systemen, bleiben Feldabweichungen ein Problem, das normalerweise entweder mit Korrekturen zu beheben versucht wird, die abhängig von der Anwendung sind, oder durch Feldmessungen die für jede einzelne benutzte Sequenz durchgeführt werden. Die Korrekturen haben jedoch im Allgemeinen einen begrenzten Anwendungs-bereich und die direkte Feldmessung erfordert spezielle Sensoren oder zusätzliche Kalibrierungsmessungen. In der vorliegenden Arbeit liegt der Schwerpunkt auf der Entwicklung einer allgemeineren Lösung für die Charakterisierung und Korrektur von reproduzierbaren Abweichungen des tatsächlichen Feldes vom nominellen Feld. Zusätzlich werden Feldfluktuationen, die zum Beispiel durch Bewegungen der untersuchten Personen zustande kommen, durch begleitende Feldmessungen erfasst und korrigiert.

Charakterisierung des Gradienten- und Shimsystems
Im ersten Teil der vorliegenden Arbeit wird die Dynamik des Gradienten- und Shimsystems charakterisiert basierend auf eine Modellierung des Systems als linear und nicht zeitabhängig (LTI –

Linear Time-Invariant). Ein LTI System ist vollständig durch die Impulsantwort des Systems bestimmt. Zur Bestimmung der Impulsantwort des Gradienten- oder Shimsystems (GIRF, Gradient Impulse Response Function, oder SIRF, Shim Impulse Response Function) wird das resultierende Feld im Inneren des Scanners bei definierten Eingangsimpulsen gemessen. Die Feldmessungen wurden hier mit den NMR Feldsensoren einer Feldkamera, für dynamische Feldmessungen von Feldern bis zu dritter Ordnung durchgeführt. Eine GIRF kann so durch eine Division von der gemessenen Feldantwort durch das bekannte Eingangssignal im Frequenzraum bestimmt werden. Mit der gemessenen GIRF kann die Feldantwort zu jedem Eingangssignal vorhergesagt werden, solange das System als ein LTI-System gut beschrieben werden kann. Die Vorhersagen können auch Kreuz-Terme der Felder beinhalten, wenn diese in der GIRF-Messung charakterisiert wurden.

Die Eingangsimpulse müssen sorgfältig ausgewählt werden, weil das Signal-Rausch Verhältnis der gemessenen GIRF stark vom Frequenzspektrum des Eingangsimpulses abhängt. Zu diesem Zweck wurden die Eigenschaften von unterschiedlichen Klassen von Eingangssignalen analysiert. In einem ersten Ansatz wurde eine Kombination von kurzen Rechteckimpulsen zur Charakterisierung des Systems verwendet. Diese können in den meisten Systemen einfach implementiert werden und die Kombination von Impulsen mit unterschiedlicher Impulslänge ermöglicht eine breitbandige Charakterisierung des Systems. Besser geeignet zur Vermessung eines Systems über einen breiten Frequenzbereich eignen sich jedoch frequenzmodulierte Impulse. Solche Impulse erlauben eine frei wählbare Verteilung der Eingangsenergie über eine vorgegebene Bandbreite bei ausreichender Impulslänge. Mit dieser Möglichkeit lassen frequenzmodulierte Impulse die Systemerfassung mit jeder gewünschten Empfindlichkeit zu.

Dreiecksimpulse wurden für die Charakterisierung des Gradienten eines kommerziellen 3T Systems angewendet. Eine Vielzahl von Systemeigenschaften konnte mit Hilfe der gemessenen GIRFs identifiziert werden, wie zum Beispiel Bandbreite, niederfrequente Verzögerungen oder Oszillationen, die durch Vibrationen der Gradientenspulen hervorgerufen werden. Die aus den bestimmten

GIRFs vorhergesagte Feldantwort wurde für unterschiedliche Eingangsimpulse mit direkt gemessenen Werten verglichen. Die Vorhersagen zeigten eine gute Übereinstimmung für eine Reihe von Dreiecksimpulsen und eine komplette Trajektorie von echo-planaren Bildgebungsmessung (EPI, Echo Planar Imaging).

Frequenzmodulierte Impulse wurden zur Charakterisierung eines Shimsystems höherer Ordnung in einem 7T Scanner angewendet. Bei unabgeschirmten Shimkanälen zeigte die Impulsantwort (SIRF) ein ausgeprägtes Maximum im Niederfrequenzbereich, das durch langsam abklingende Wirbelströme erzeugt wird. Darüber hinaus wurde ein komplexes Muster von Resonanzen und starken Feldantworten in Kreuztermen beobachtet. Feldantworten zu verschiedenen Eingangsimpulsen konnten durch die gemessene SIRFs gut vorhergesagt werden, auch in den Kreuz-Termen.

Pre-emphasis

Bis zu einem gewissen Grad können Feldverzerrungen durch die nachträgliche Korrektur der gemessenen Daten kompensiert werden. Solche Verfahren sind jedoch nicht anwendbar im Fall von zum Beispiel Dephasierung innerhalb einer Schicht oder eine gestörte Anregungsgeometrie, weshalb eine hohe Exaktheit der tatsächlichen Feldverläufe von immenser Bedeutung ist. Ein etabliertes Verfahren zur Kompensation von Feldverzerrungen durch Wirbelströme ist eine so genannte Pre-emphasis, das heisst, die Vorfilterung der Eingangsimpulse. Typischerweise setzen sich diese Filter als Summe von Exponentialfunktionen zusammen. Mit solchen Modellierungen lässt sich jedoch die Fülle der komplexen Feldverzerrungen nicht beschreiben. In der vorliegenden Arbeit wurden deshalb neue Ansätze der Signalvorbehandlung unter Zuhilfenahme der oben geschilderten LTI Systembeschreibung untersucht. Zu diesem Zweck wurden breitbandige digitale Vorfilter auf der Basis der invertierten gemessenen SIRF erstellt, die den Vorteil einer hohen Flexibilität in der Gestaltung der resultierenden Frequenzantwort bieten. Dieser Ansatz wurde erweitert um ausserdem Feldverzerrungen in Kreuztermen zu kompensieren, indem diese Filter zwischen den Eingängen verschiedener Feldkanäle verwendet wurden. Damit konnten auch frequenzabhängige, räumlich lineare Feldantworten als Folge von

Eingangsimpulsen der Shimspulen höherer Ordnung unterdrückt werden.

Die Benutzung von fest definierten Vorfiltern kann jedoch nicht für alle denkbaren Eingangssignale die optimale Systemgenauigkeit gewährleisten. Nur durch die Sequenzspezifische Optimierung des Eingangssignals lässt sich das bestgeeignete Signal für eine gegebene Systemimpulsantwort und systemimmanenten Beschränkungen, wie zum Beispiel Amplitudenbegrenzungen, ermitteln. Abhängig von der gewünschten Zielsetzung sind unterschiedliche Lösungsansätze erforderlich. In der vorliegenden Arbeit werden einige in der Praxis nützliche Ansätze behandelt und Algorithmen zur iterativen Optimierung implementiert. Dieses Vorgehen führt zur Steigerung der Genauigkeit von Trajektorien im k-Raum auf einem System mit Standardkompensationen gegen Wirbelströme.

GIRF-basierte Bildrekonstruktion

MRI-Anwendungen, die Bilder in sehr kurzer Zeit erzeugen sollen, werden wegen der hohen Systemanforderungen besonders stark durch Imperfektionen der Feldverläufe, die durch das Gradientensystem erzeugt werden, beeinflusst. Wenn der tatsächliche zeitabhängige Feldverlauf bekannt ist, ist es im Allgemeinen möglich in der Bildrekonstruktion die Effekte der Feldverzerrungen zu kompensieren. In der vorliegenden Arbeit wurde untersucht, inwieweit sich GIRF-basierte Vorhersagen von k-Raum-Trajektorien für die Bildrekonstruktion eignen. Dazu wurden Phantom und in-vivo EPI Daten eines 3T Systems genutzt, um Bildrekonstruktionen basierend auf nominellen, GIRF-bestimmten und gemessenen Trajektorien miteinander zu vergleichen. Es zeigt sich, dass die GIRF-bestimmten Trajektorien sogenannte Ghosting-Artefakte nahezu vollständig eliminieren und eine vergleichbare Bildqualität zu Rekonstruktionen mit gleichzeitig gemessenen Trajektorien ergeben. Diese Technik ist nicht begrenzt auf einzelne k-Raum Muster und kann im Sinne einer einmaligen Systemkalibrierung genutzt werden.

Physiologisch Induzierte Feldfluktuationen

Es ist bekannt, dass Feldfluktuationen durch die Atmung oder Körperbewegung der untersuchten Personen erzeugt werden können, die

damit die Qualität der Bilder des Gehirns bei hohen Feldstärken negativ beeinflussen. In der vorliegenden Arbeit wurde dieser Einfluss auf hochauflösende T2*-gewichtete Bilder des Gehirns in einem 7T Scanner untersucht und Korrekturen mit Hilfe von gleichzeitigen Feldmessungen durchgeführt. Die physiologisch induzierten Feldfluktuationen führten zu Bildartefakten wie Ghosting, Unschärfen und streifenförmigen Intensitäts-modulationen in den Bildern. Diese Bildstörungen konnten durch Korrekturen auf der Basis von gleichzeitigen Feldmessungen erheblich reduziert werden. In den meisten Fällen genügte bereits eine Korrektur mit räumlichen sphärischen harmonischen Basisfunktionen erster Ordnung. In einigen Fällen konnten auch Korrekturen höherer Ordnung sichtbar zur Bildverbesserung beitragen.

Schlussfolgerungen

Die Charakterisierung der Gradienten- und Shimfelddynamik unter der Annahme von Linearität und Zeitunabhängigkeit ist ein schnelles und einfaches Verfahren das eine Mehrheit von Störeffekten einschliesst. Es wurde hier gezeigt dass Pre-emphasis dadurch verbessert werden konnte und dass nachträgliche Korrekturen von durch Feldverzerrungen hervorgerufene Effekte, basierend auf den GIRFs, möglich sind. Das Verfahren bietet eine Grundlage zur weiteren Behandlung von störenden Einflüssen nicht optimaler Felddynamik. Physiologisch bedingte Feldfluktuationen lassen sich durch den Einsatz von gleichzeitigen Feldmessungen kompensieren.

Chapter 1

Introduction

1.1 Background

Since it was first proposed in the 1970's to form images of objects based on nuclear magnetic resonance (1–3), Magnetic Resonance Imaging (MRI) has steadily gained significance and is today both a workhorse in medical diagnostics as well as a tool for cutting-edge research in various fields. The popularity of the technique partly owes to the non-invasive character of the examinations, relying on interactions of the tissue with a strong background magnetic field and electromagnetic waves in the radiofrequency range. Unlike X-ray and Computed Tomography it does thus not require ionizing radiation for the imaging procedure. Another decisive factor for the success of MRI is the excellent depiction of soft tissue and the versatility in the contrast mechanisms that can be generated. Thus a range of different tissue properties can be probed with the technique, rendering it useful for studying anatomy, function and pathophysiology of nearly any bodily organ.

Despite the rapid technical development that MRI has undergone, there are still a few major challenges remaining to be addressed, and ample room for further refinements of the technique. While some MR research aims to explore novel domains of usefulness for the modality, such as new contrast mechanisms, a considerable amount of technical development focuses on improving the basic system components necessary for image formation. Any MR imaging experiment fundamentally requires a background magnetic field to magnetize tissue, electromagnetic waves to excite the magnetized spins and time-varying magnetic field gradients to encode spatial information. The performance of each of these subsystems is crucial for the quality of the acquired data.

In the present thesis, the focus will be on the superposed time-varying fields required for signal localization and frequently also for contrast encoding. It will be investigated how the dynamics of these fields can be characterized, how the characterization can enhance field control and finally how the knowledge of the time-varying fields can be used to improve imaging results.

1.2 NMR – basic principles

In Nuclear Magnetic Resonance (NMR) chemical samples can be observed due to interactions of atomic nuclei with external magnetic fields (4,5). The nuclei have a property called spin, which can assume different values depending on chemical element and isotope. The spins act as tiny magnetic dipoles, which when placed in an external magnetic field tend to align with the field, i.e. the sample gets polarized. Furthermore, the spins precess around the main magnetic field vector with a frequency proportional to the strength of the external field. The proportionality constant, termed gyromagnetic ratio, is a nucleus-dependent property, and hence the precession frequency, i.e. the Larmor frequency, varies with the nucleus under study.

By applying external oscillating fields at the Larmor frequency, transitions between energy states of the spins can be stimulated and a phase coherence between different spins in the sample can be induced. In a classical description of this excitation process, this is regarded as tipping the resultant vector of the spin magnetization away from the direction of the main magnetic field. The magnetization thus acquires a component in the plane transversal to the main magnetic field vector. This transversal magnetization continually precesses about the main magnetic field vector and can be detected by Faraday induction in coils placed in the vicinity of the sample. The frequency content of the detected signal consequently depends on the strength and distribution of the background magnetic field, and the chemical composition of the sample. Most *in vivo* MR experiments target hydrogen nuclei, i.e. protons, of water, due to their natural abundance in the body. At the field strengths of modern MR systems, the Larmor frequency of protons is in the radiofrequency (RF) range, which providentially shows a high degree of penetration in biological tissue.

As the spins gradually relax back into the thermal equilibrium state the resulting detectable signal decays. The spin relaxation is primarily governed by two processes, namely the loss of coherence between spins, termed T2-relaxation, and the recovery of magnetization along the direction of the main magnetic field vector, termed T1-relaxation. The time constants of the relaxation processes depend on

many factors in the environment of the spins in a highly complex fashion.

The detected NMR signal is rich with information on the sample studied. Signal strength is proportional to the magnetization of the sample, which among others depends on spin density. The frequency reveals information on chemical content and magnetic field variations, and relaxation times highly depend on the local environment of the spins. Furthermore, experiments sensitive to motion of the spins, e.g. diffusion, and spin-spin coupling mechanisms can be designed. All of these mechanisms can be utilized to study biological tissue *in vivo*. For imaging, T1- and T2-relaxation times are frequently used sources of image contrast, as these parameters vary considerably between different tissues.

1.3 From NMR to MRI

The principle of NMR was used in chemistry to investigate various molecular and atomic properties, long before the advent of MRI. The key invention that made it possible to perform imaging based on NMR signal was the encoding of spatial information in the signal with the use of magnetic field gradients. The most commonly used imaging strategy today is Fourier encoding in two dimensions, which will therefore be outlined below.

To acquire two-dimensional images of an object, selective excitation of spins within a slice is performed. This can be done by applying a linear magnetic field gradient to the sample while transmitting RF waves for excitation. The gradient field thus induces a position-dependent frequency spread of the spins within the sample, such that only spins within the selected slice precess at frequencies contained in the RF pulse.

The receive coil generally picks up signal from all excited spins within the object. The time-dependent signal, *s(t)*, can thus be written as a sum of the contributions over the whole volume:

$$s(t) = \int_V \rho(\bar{r}) e^{-i\varphi(\bar{r},t)} d\bar{r} \ , \qquad\qquad [1.1]$$

where $\bar{r}$ is the position vector, $\rho(\bar{r})$ represents the spin density of the object, $\varphi(\bar{r},t)$ the phase of the spin precession and V the volume of the excited slice. T1- and T2-relaxation effects are neglected in this formulation of the signal equation, as they are not relevant to understand the principles of spatial encoding in MRI.

The frequency, $\omega(\bar{r},t)$, of the spins is proportional to the strength of the local magnetic field, $B(\bar{r},t)$:

$$\omega(\bar{r},t) = \gamma B(\bar{r},t) \ . \qquad [1.2]$$

The magnetic field can ideally be decomposed into a static uniform component, B_0, and time-varying linear gradient fields in the plane of the slice. Defining the slice to lie in the plane spanned by the x and y coordinates, the gradient field can in a vector notation be written as:

$$\bar{G}(t) = (G_x(t), G_y(t), 0) \ . \qquad [1.3]$$

This yields the magnetic field:

$$B(\bar{r},t) = B_0 + G_x(t)\,x + G_y(t)\,y \qquad [1.4]$$

or in vector notation:

$$B(\bar{r},t) = B_0 + \bar{G}(t) \cdot \bar{r} \ . \qquad [1.5]$$

The resulting spin frequency distribution is:

$$\omega(\bar{r},t) = \omega_0 + \gamma \bar{G}(t) \cdot \bar{r} \qquad [1.6]$$

where

$$\omega_0 = \gamma B_0 \ . \qquad [1.7]$$

The phase of the signal is the time-integral of the frequency since excitation:

$$\varphi(\bar{r},t) = \gamma \int_0^t \omega(\bar{r},\tau)d\tau \ , \qquad [1.8]$$

assuming that the initial phase after excitation is zero. Inserting Eq. [1.5] and demodulating the signal by the carrier frequency, ω_0, yields:

$$\varphi(\bar{r},t) = \gamma \int_0^t \bar{G}(\tau) \cdot \bar{r}d\tau \ . \qquad [1.9]$$

Representing the time-integral of the gradient vector with a vector of phase coefficients:

$$\bar{k}(t) = \gamma \int_0^t \bar{G}(\tau)d\tau \ , \qquad [1.10]$$

where

$$\bar{k}(t) = (k_x(t), k_y(t), 0) \ , \qquad [1.11]$$

the phase distribution of the spins can be described by:

$$\varphi(\bar{r}, t) = \bar{k}(t) \cdot \bar{r} \ . \qquad [1.12]$$

Inserting this representation of the phase into Eq. [1.1] yields the signal equation:

$$s(t) = \int_V \rho(\bar{r}) e^{-i\bar{k}(t) \cdot \bar{r}} \, d\bar{r} \ . \qquad [1.13]$$

Eq. [1.13] is equivalent to a 2-dimensional Fourier Transform of the spin density distribution, $\rho(\bar{r})$, with $\bar{r}$ and $\bar{k}$ being the pair of transform variables (Fig. 1.1). The variable $\bar{k}$ describes the linear phase accumulated over the sample and can be regarded to represent spatial frequencies. The domain spanned by $\bar{k}$ is in MRI often called k-space. Sampling the signal at one point in k-space thus amounts to sampling the corresponding spatial frequency content of the spin distribution of the object. By acquiring enough samples in k-space, a 2-dimensional representation of the Fourier transform of the object emerges. An inverse Fourier transform yields the final image, $v(\bar{r})$:

$$v(\bar{r}) = \int_{V_k} s(\bar{k}) e^{i\bar{k} \cdot \bar{r}} \, d\bar{k} \qquad [1.14]$$
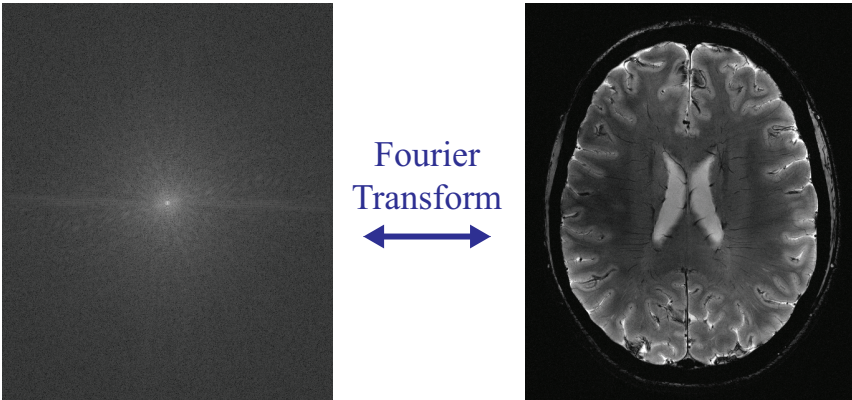
Fig. 1.1: *Brain image (**right**) and its representation in the frequency domain (**left**). The left-side image corresponds to the signal sampled in an MR imaging experiment.*

where V_k is the sampling volume in k-space. The spatial encoding can easily be extended to cover three dimensions by employing also gradient fields in the *z*-direction.

Each sample point in k-space corresponds to sampling the signal at one point in time and the k-space position is determined by the time-integral of the gradient waveforms. The gradient time-courses thus have to be designed such as to cover the desired region of k-space with sufficient density. Many different strategies on how to sample k-space have been developed. The most commonly used is Cartesian sampling, in which samples are acquired on a regular grid in k-space. In many applications, one line of k-space is acquired after each spin excitation. This yields a robust sampling scheme, but a rather slow acquisition as the magnetization has to recover between the readout of each k-space line. In a faster approach, termed echo-planar imaging (EPI), several
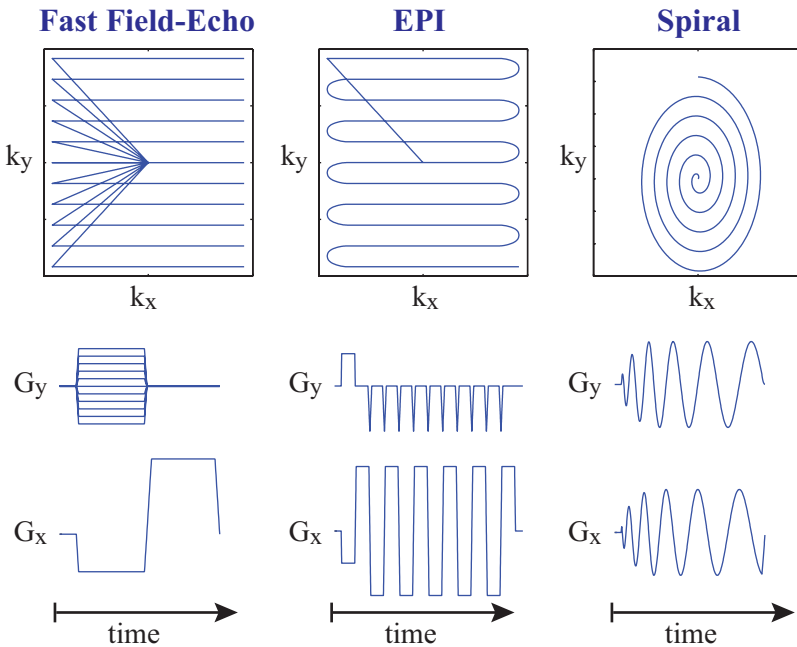
Fig. 1.2: *Common k-space sampling trajectories and their respective gradient time-courses.*

lines in k-space are acquired in each readout, up to covering the full k-space after one spin excitation. Other more advanced sampling strategies include spiral or radial sampling. A few common k-space sampling patterns together with the corresponding gradient time-courses are shown in Figure 1.2.

1.4 Dynamic field imperfections

To successfully reconstruct images based on the acquired signal, it is crucial that the signal time points, $s(t)$, accurately can be assigned to points in k-space, $s(\overline{k})$. This amounts to having very exact knowledge of the time-courses of the applied gradient fields. The magnetic field gradients are generated by running currents through coils that are specifically designed to produce linear field patterns in three orthogonal directions. The control over the gradient time-courses thus goes via control of current time-courses in the gradient coils. The gradient waveforms required for imaging typically lie in the kHz range.

For a number of reasons, the actual time-courses of the fields the sample sees in the bore of the scanner generally deviate from the desired ones. Some of the common mechanisms affecting the temporal characteristics of the gradient fields are:

- *Bandwidth limitations* determined by the frequency response characteristics of the amplifiers driving the currents and by the resistance and self-inductance of the coils.
- *Delays* introduced by timing mismatches between the gradient chain and the receive chain.
- *Eddy currents* generated in conducting structures in the surrounding, e.g. in low-temperature heat shields around the main magnet. The eddy currents give rise to magnetic fields that tend to oppose any field changes in the scanner bore.
- *Mechanical vibrations* of the coils at gradient switching lead to current induction in the coils and consequently also to oscillating gradient fields in the scanner bore.

- *Thermal drifts* can change the state of the main magnet and magnetic materials used for field homogenization, and thereby slowly change the background magnetic field.
- *External field fluctuations* can arise from objects in the surrounding, such as equipment brought into the scanner room or motion of the subject in the scanner.

Performing image reconstruction assuming an ideal k-space sampling pattern in the presence of field imperfections can lead to a range of artifacts in the images. The appearance and severity of the artifacts depend heavily on characteristics of the field deviations in combination with properties of the employed k-space sampling scheme. To understand the nature of the artifacts, one generally has to examine properties of the Fourier transforms. Commonly occurring artifacts for Cartesian sampling schemes are geometrical distortions due to distortions of the k-space trajectory, as can occur due to e.g. slow eddy current fields. A scaling in the k-space domain corresponds to a scaling in the image domain, with the inverse scaling factor (Fig. 1.3B). Correspondingly, a skewing in k-space consequently leads to a skewed image (Fig. 1.3C). For a line-by-line Cartesian sampling scheme, a general shift of the trajectory due to gradient delays produces a linear phase over the image. For EPI trajectories, however, gradient delays can have considerably more severe effects. Since the readout lines are acquired in alternating directions, gradient delays cause a cyclic modulation of the data with a period of every second readout line. A modulation in k-space corresponds to a convolution in image space, thus producing replicas of the object at shifted positions (Fig. 1.3D). These replicas are usually termed ghosts and belong to the most detrimental and persistent artifacts for EPI sampling schemes.

Slow sampling schemes of acquiring k-space line-by-line operate less at the limits of the gradient system, and hence are generally more robust. The long acquisition times, however, render them sensitive to motion of the object and slow fluctuations in the background magnetic field. Such field fluctuations can cause incoherent phase modulation between readout lines, giving rise to both ghosts and blurring in the images. Non-Cartesian sampling schemes, such as spiral trajectories, are generally highly susceptible to artifacts due to gradient
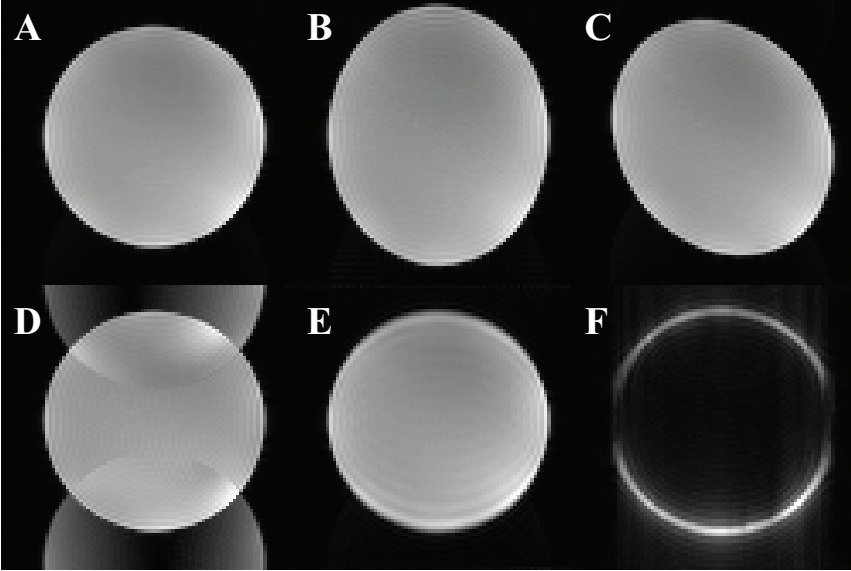
Fig. 1.3: *Image of a spherical phantom reconstructed based on different k-space trajectories. **A** shows the image reconstructed based on a measured k-space trajectory. The same imaging data was reconstructed with a k-space trajectory compressed in one direction (**B**) and skewed in two directions (**C**). Introducing a delay on the trajectory yields the ghosted image in **D**. Utilizing only data from the center of k-space in one direction, results in a lower resolution and ringing artifacts (**E**). Picking the same amount of data as in E, but from the periphery of k-space yields an image where edges only are represented (**F**).*

delays and field imperfections. For spirals, the artifacts often take the form of blurring, which can render images very difficult to interpret.

Many of the artifacts arising from field imperfections can be corrected for if the true gradient time-courses are known. However, when the k-space sampling is so severely affected as to not contain necessary information on the object, this necessarily leads to loss in image quality. This is demonstrated in Figure 1.3EF, with partial sampling of k-space only. In Figure 1.3E only low-frequency components, corresponding to the center of k-space, in one direction

have been sampled. This leads to an acceptable image but with suboptimal resolution in one direction. One can also notice a phenomenon of subtle ringing in the image - an artifact related to insufficient sampling of high spatial frequencies. Conversely, in Figure 1.3F the center of k-space has been left out, leaving the image reconstruction with high-frequency information only. Correspondingly, only features of the image that have a significant high-frequency component, such as sharp edges, are depicted.

Apart from being used for spatial encoding of the object, time-varying linear gradient fields can also be employed for generation of different contrast mechanisms. A prominent example is diffusion-weighted imaging, where gradient fields are used to sense the diffusion of water inside the object. As for spatial encoding, the preparation of contrast often depends on the gradient time waveforms and can therefore be affected by gradient imperfections.

1.5 Static field imperfections

It is of utmost importance in MRI that the background field is static and homogeneous. Commercial MR systems typically have homogeneity specifications on the order of <ppm within a defined volume inside the scanner bore. When an object is introduced into the background field, however, the net magnetic field is altered by the magnetization of the object. The resulting field distribution is a function of object geometry and magnetic susceptibility of the materials within the object. For *in vivo* imaging, the most significant field disturbances arise from interfaces between air and tissue, which differ in magnetic susceptibility by about 9 ppm. This is especially problematic in brain imaging, where the air-filled sinuses and ear canals lie very close to regions of interest in the brain.

In the presence of background field inhomogeneities the signal equation can be written as:

$$s(t) = \int_V \rho(\bar{r}) e^{-i\Delta\omega(\bar{r})t} e^{-i\bar{k}(t)\cdot\bar{r}} d\bar{r} \ , \qquad\qquad [1.15]$$

where $\Delta\omega(\bar{r})$ is the deviation from ω_0, due to static local field deviations. The equation thus no longer perfectly represents a Fourier

Transform. What effect this has on the encoding and in the resulting images depends on a number of factors. The magnitude of the field deviations naturally affects the severity of the problem. So do the timing parameters of the imaging experiment, as the local frequency shifts cause the spins to accrue increasing phase offsets over time. In Cartesian k-space sampling schemes field inhomogeneities frequently lead to geometrical distortions of the images, whereas with spiral sampling they tend to cause image blurring. Furthermore, static field gradients in the direction perpendicular to the slice can be a significant problem as they cause dephasing of the spins within the slice, leading to a loss of signal from affected areas.

In order to homogenize the background field within the object, so called shimming is often performed. This amounts to adding static magnetic fields from the outside such as to neutralize the local field deviations inside the object. Shimming can be performed passively, by placing magnetized materials in the vicinity of the object, or actively by driving currents through coils that produce fields of specific spatial distribution. Many MR systems have, apart from the linear gradient coils, a set of shim coils for this purpose. The shim coils often produce spherical harmonic field terms of 2nd- or higher order.

There is however a fundamental difficulty in trying to counteract field deviations caused by variable magnetization inside an object by fields generated from the outside. The field distribution within the object can generally not be well approximated by a low number of smooth field terms, as are generated by the shim coils. Standardly, shimming aims to homogenize the field over the full volume of interest inside the object. The smaller the volume, however, the better homogeneity can be achieved. From this recognition, the idea has developed to match the shimming to smaller subvolumes instead of to the whole object. Most straightforward is to shim on a single slice only and update the shim settings between acquisitions of different slices. The latter, however, requires the currents through the higher-order shim coils to be driven dynamically, with ideal update times on the order of milliseconds. All effects that influence the field dynamics for the linear gradient fields thus also come into play for the higher-order shim fields. Field imperfections can often be even more pronounced for the shim

system, as the hardware generally has not been optimized for dynamic performance to the degree of the gradients.

Experimentally, fields of higher spatial orders are being used not only for shimming, but also for spatial encoding of the signal. This yields more degrees of freedom in the encoding process, and can have the advantage of increased spatial resolution within regions of interest. Other advantages include the potential to accelerate acquisitions, as well as reducing peripheral nerve stimulation due to high local dB/dt. For successful implementation, however, this requires high dynamic performance of a set of both linear gradient and higher-order field coils.

# 1.6 Spatiotemporal field monitoring

A key step towards developing corrections for dynamic field imperfections is the ability to measure magnetic fields with sufficient temporal resolution and spatial discrimination. There is a variety of methods that can be used for field measurements. In this thesis, an approach based on NMR signal is employed (6,7). This has the advantage that the measurement is governed by the same principles as the experiment to be controlled, thus inherently yielding similar sensitivity to field variations.

Small NMR field probes are employed to sense the magnetic field at selected points in space. Figure 1.4 shows a picture of such a field probe. A thin capillary in the center is filled with an NMR-active liquid and is surrounded by a coil for sample excitation and signal reception. Capillary and coil are embedded in an ellipsoidal epoxy encasing, and the coil wire ends are connected to a tuning/matching electrical circuit to tune the coil to the Larmor frequency of the NMR signal from the probe filling.

Upon excitation of the sample in the probe, signal is generated with a phase, $\varphi(t)$, that is proportional to the integral of the magnetic field since excitation:

$$\varphi(t) = \gamma \int_0^t B(\bar{r}_p, \tau) d\tau + \varphi_0 \ . \qquad [1.16]$$
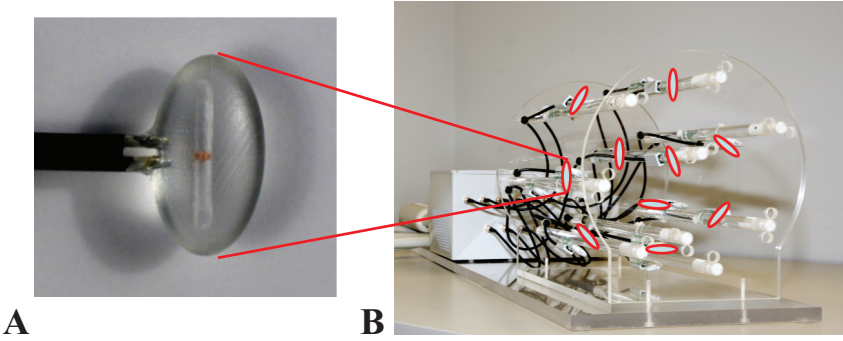
Fig. 1.4: *Picture of an NMR field probe (**A**) and a dynamic field camera (**B**) consisting of a number of probes distributed as on the surface of a sphere. Courtesy of Skope Magnetic Resonance Technologies, Zurich, Switzerland.*

Here $\bar{r}_p$ is the position of the probe and φ_0 is the initial phase after excitation. The magnetic field strength at the probe position can thus be obtained from a time-derivative of the signal phase:

$$\omega(t) = \gamma B(\bar{r}_p, t) \ . \qquad [1.17]$$

The temporal resolution of the measurement is limited by the spectrometer of the receive system only, and is typically on the order of microseconds.

A single field probe thus allows for magnetic field measurements with high temporal resolution at one spatial position. Utilizing several probes it is possible to extract information on the spatial distribution of the magnetic field. Assuming a smooth field originating from outside the volume of interest, the spatial field distribution can be approximated by a low number of basis functions:

$$B(\bar{r}, t) \approx \sum_i c_i(t) \cdot b_i(\bar{r}) \ , \qquad [1.18]$$

where $c_i(t)$ are time-varying coefficients representing the contribution of the spatial basis functions $b_i(\bar{r})$ to the total magnetic field. Neglecting φ_0, the signal phase of a probe at position $\bar{r}_p$ can thus be described as:

$$\varphi_p(t) = \gamma \sum_i \int_0^t c_i(\tau) d\tau \cdot b_i(\overline{r}_p) \ . \qquad [1.19]$$

The integral of the time-varying field coefficient $c_i(t)$, can be replaced by a phase coefficient, $k_i(t)$:

$$k_i(t) = \gamma \int_0^t c_i(\tau) d\tau \ , \qquad [1.20]$$

yielding

$$\varphi_p(t) = \gamma \sum_i k_i(t) \cdot b_i(\overline{r}_p). \qquad [1.21]$$

The signal phase from a number of probes distributed within the volume can thus in a vector-matrix notation be described as:

$$\begin{pmatrix} \varphi_1(t) \\ \vdots \\ \varphi_{np}(t) \end{pmatrix} = \begin{pmatrix} b_1(\overline{r}_1) & \cdots & b_{ni}(\overline{r}_1) \\ \vdots & \ddots & \vdots \\ b_1(\overline{r}_{np}) & \cdots & b_{ni}(\overline{r}_{np}) \end{pmatrix} \begin{pmatrix} k_1(t) \\ \vdots \\ k_{ni}(t) \end{pmatrix} \qquad [1.22]$$

where *ni* is the number of basis functions and *np* the number of probes employed. In a more compact representation this yields:

$$\overline{\varphi}(t) = \mathbf{P}\overline{k}(t) \ , \qquad [1.23]$$

where

$$P_{pi} = b_i(\overline{r}_p) \ . \qquad [1.24]$$

If the signal phase is measured for a number of probes at known positions in space, the phase coefficients, $k_i(t)$, given a set of basis functions, can accordingly be obtained from the pseudo-inverse of the matrix **P**, here denoted by **P**⁺:

$$\overline{k}(t) = \mathbf{P}^+\overline{\varphi}(t) \ . \qquad [1.25]$$

For good conditioning of the measurement, the number of probes utilized must match or exceed the number of basis functions used to approximate the field. The probes should furthermore be placed at appropriate locations depending on the chosen set of basis functions.

The spatial basis functions should be selected such as to describe the actual spatial field distribution as accurately as possible with a low number of basis functions. Assuming there is no source of dynamic magnetic fields within the volume of interest, each component

of the field must fulfill the Laplace equation. As solid spherical harmonics are solutions to the Laplace equation within a ball, these are well suited for the purpose. Table 2.1 lists the real-valued spherical harmonics in Cartesian coordinates up to 3rd order. Up to first order these contain a spatially uniform term and one linear term along each coordinate axes. The phase coefficients for the linear basis functions thus correspond to the k_x, k_y, k_z introduced to represent the integral of gradient fields for spatial encoding. With a set of at least four NMR field probes the actual k-space trajectory can thus be directly measured with high temporal resolution.

As a possible alternative, cylindrical harmonics also fulfill the Laplace equation. As such they are a natural choice for describing fields with boundary conditions given on a cylinder. This property is frequently taken advantage of in the design of gradient and shim coils. Defining the desired target field in cylindrical coordinates, the required current distribution on a cylindrical former can thereby straightforwardly be calculated (8). For field measurements, however, the spherical harmonics yield a more generic description of fields stemming from unknown sources that may not be exclusively of cylindrical geometry. Furthermore, gradient and shim coils are frequently designed to produce field distributions close to single spherical harmonic functions and can therefore generally be well captured by a low number of field terms based on spherical harmonics.

The capability of measuring magnetic field dynamics with high spatial and temporal fidelity is an essential tool for addressing imperfections of field evolution. One straightforward strategy is to measure actual k-space trajectories during individual scans and incorporate this information upon image reconstruction. However, this approach alone is both rather demanding and limited. It is demanding in that it requires high-performing concurrent field sensing hardware to be available for each individual scan. Such equipment will likely remain an excessive investment for many routine uses of MRI, calling for ways of characterizing imperfect field behavior at the system level rather than on a per-scan basis. The limitations of mere trajectory measurement arise from the fact that it only determines but does not actually mitigate field imperfections. Only a certain range of field imperfections can be successfully addressed at the image reconstruction level. Even with

perfect knowledge of field evolution, substantial imperfections will give rise to ill-posed reconstruction problems, e.g., when sampling density criteria are violated or when data are otherwise irreversibly impaired such as by disruption of steady states, inconsistent volume selection or through-plane dephasing. In these situations, knowledge of imperfect field behavior should rather be leveraged to enhance the accuracy of field dynamics in the first place. To this end, however, it again needs to be put in the context of the properties and control of the hardware that is used to generate the dynamic magnetic fields.

1.7 Thesis outline

The common theme of the work presented in the different chapters of this thesis is the quest for new tools to improve and simplify the characterization of and compensation for dynamic field perturbations in MRI. These goals are pursued by concerted use and advancement of field measurements, system modeling, hardware driving strategies, and image reconstruction.

The main body of the thesis is focused on reproducible field perturbations, with special attention given to effects that can be described by a linear model. Many correction schemes already exist for handling reproducible field imperfections. However, they are generally only valid for specific applications or trajectory types, and typically require a calibration measurement for each trajectory. One of the aims of this thesis has been to develop a more generic approach to know and to correct for reproducible field perturbations.

To this end, a method for characterization of the dynamic properties of a gradient or shim system, based on modeling the system as linear and time-invariant, is presented in Chapter 2 and 3. Chapter 2 describes how to probe a linear time-invariant system with a combination of short block pulses, and discusses how the noise level of the characterization is affected by the input signal. Data from the characterization of the gradient system on a commercial 3T scanner is presented and analyzed. In Chapter 3, the concept is extended to introduce frequency sweeps as probing signals, and a framework for designing frequency-swept pulses for probing the system with

customized sensitivity is developed. The method is applied to characterize the gradients and the higher-order shim system of a whole-body 7T system.

Knowing the system response is a first step towards being able to actively counteract the perturbing fields. In Chapter 4, it is described how this knowledge can be utilized to design pre-emphasis filters to modify input waveforms in order to compensate for undesired field effects, and to achieve a targeted profile of the frequency response of the system. As a further extension to the concept of adjusting the input waveform, an optimization algorithm working to find the ideal input waveform for optimal field fidelity given a known system response and hardware limitations, is outlined.

In Chapter 5, the system response, measured as described in Chapter 2, is utilized to predict the field response to the input gradient sequence of an echo-planar imaging experiment – a widely used sequence for fast imaging in MRI. Images acquired on a 3T system are reconstructed based on trajectories calculated from the estimated field output, and are compared to reconstructions based on the nominal trajectories, as well as trajectories measured directly with concurrent magnetic field monitoring.

Chapter 6 deals with non-reproducible field perturbations, namely fluctuations caused by the physiology of the subject inside the scanner. More specifically, field fluctuations due to breathing and limb movements, and their effects on T2*-weighted high-resolution brain images at 7T are investigated. As these fluctuations cannot be known beforehand, concurrent field monitoring is performed during the scans and the measured field perturbations are included in the reconstruction up to 3rd-order spherical harmonics.

Finally, a brief outlook on possible future applications relating to the work presented in this thesis is given in Chapter 7.

Chapter 2

Gradient System Characterization by Impulse Response Measurements with a Dynamic Field Camera

2.1 Introduction

Time-varying magnetic field gradients are essential for signal preparation and encoding in magnetic resonance imaging and spectroscopy. Most MR methods rely on highly accurate gradient time-courses for correct signal encoding and suffer from artifacts when significant deviations from the prescribed time-courses occur. In practice, effective gradient waveforms usually do differ somewhat from the ideal shapes defined in the underlying pulse sequence. These deviations are largely due to a variety of hardware imperfections including bandwidth limitations of gradient amplifiers, eddy currents induced in gradient coils and in other conducting structures of the scanner (9,10), field fluctuations caused by mechanical vibrations after gradient switching (11,12), and thermal variation in hardware components (13). Slight perturbations can also stem from physiologically induced fields that originate in the subject under examination (14,15), or from magnetic sources and currents external to the MR system.

Besides further hardware optimization, the most common ways of addressing dynamic field imperfections are pre-compensation of gradient waveforms (16–18) and post-correction of acquired data (19). Both of these options are most feasible for mechanisms of perturbation that are reproducible and can be accurately modeled. Physiological and external field contributions as well as thermal effects are challenging to address in this way. However, eddy currents, which are usually the dominant causes of field imperfections, as well as mechanical effects have been successfully modeled and predicted.

Eddy currents arise due to the self- and cross-inductance of gradient coils as well as the cross-inductance between gradient coils and other conductive structures of the scanner, such as shim coils or parts of the cryostat. To model eddy currents, the conductors involved are usually approximated as LR circuits, i.e., as combinations of an inductance and a resistance, in which induced currents decay exponentially (9,10,20). Using linear systems theory, the net step response of a gradient chain can then be modeled as a superposition of an ideal response, i.e., a Heaviside function, and a set of exponentially decaying field terms representing eddy currents of different sources.

Response models of this kind are traditionally used to predict eddy current effects and to determine pre-emphasis settings for a given system (16,17,20,21).

Field oscillations due to mechanical vibrations are a well-known disturbance in MR spectroscopy where they can cause modulation sidebands particularly of unsuppressed water peaks. Similar to eddy current effects, the underlying mechanics and conversion from vibrations to magnetic fields have been viewed as linear mechanisms that contribute to a net linear impulse response (22). Using this approach, mechanically mediated field oscillations have been modeled as exponentially damped sinusoidal responses, which have been used to simulate sideband effects (12,23). Linear systems theory has also been used to characterize the acoustic response of a gradient system, relying on sound pressure measurements in the magnet bore (24–26).

So far, the models of field responses due to eddy currents and mechanical effects have relied on simplifying abstractions. For both mechanisms, it has been assumed that only a limited number of distinct instances occur, which obey an elementary pattern such that they can be represented by small sets of exponentials and exponential sinusoids, respectively. In general, this picture will hold only approximately. Due to the electrical and mechanical complexity of gradient systems and MR systems as a whole, both eddy-current and mechanical behavior may require expansion into very many components of different time constants. Eddy currents may be supported by structures that cannot be fully modeled as mere LR circuits. Moreover, coupling may occur both among structures that can carry eddy currents and among mechanical resonances, giving rise to yet more complex behavior.

To better capture the variety of possible behavior, it is attractive to remove model assumptions on individual eddy-current processes or mechanical resonances and rather characterize a gradient system in terms of its complete impulse response function (27,28). According to linear systems theory, this approach should permit jointly representing all response mechanisms that are linear and time-invariant (LTI). A net gradient impulse response function (GIRF) should hence incorporate all influences on the gradient waveform between the console and the magnet bore. This would include amplifier and coil characteristics as well as eddy currents and vibration-induced fields, without the need to

consider individual underlying mechanisms. Knowledge of the comprehensive GIRF could form the basis of advanced pre-emphasis and serve for quality assurance purposes. It could also yield more accurate estimates of effective k-space trajectories for image reconstruction and of other encoding parameters such as b-values in diffusion imaging or gradient moments in velocity mapping.

The key challenge toward this goal is determining GIRFs accurately, with sufficient bandwidth and frequency resolution, and within reasonable measurement times. Probing the GIRF must generally involve observing a system's response to given gradient input waveforms. This could be achieved with known NMR-based techniques for measuring gradients and k-space trajectories (29–34). Partly, these methods rely on selective excitation of larger phantoms or imaging objects and signal detection with large receiver coils (30–32). Such detection methods offer only limited sensitivity, while the extent of the imaging object makes it prone to de-phasing by potential in-plane gradient responses. Methods that rely on a dedicated small sample are also limited in sensitivity unless the sample is mounted in a tight-fitting detector with a high filling factor (29,33,34). All of these methods have the disadvantage that each measurement needs to be repeated several times either to achieve temporal resolution or to distinguish different spatial field components.

An efficient alternative is to record the field evolution with a dynamic field camera (35), i.e., with an array of miniature NMR probes that are operated simultaneously and positioned such as to distinguish different spatial components of interest (6,7). This approach was recently proposed for monitoring magnetic field evolutions concurrently with image acquisition (36). However, it is equally suited for mere field observations as required for GIRF measurements. Relying on tightly wound detectors around small sample droplets, it combines high sensitivity with robustness against de-phasing. The temporal resolution of the camera measurement is limited only by the acquisition bandwidth of the spectrometer used and the simultaneous recording at different positions immediately yields differentiation of a gradient's self- and cross-responses.

In the present work, it is proposed to determine comprehensive gradient response functions using field observations with a dynamic

field camera. Starting from LTI systems theory, a strategy is derived for obtaining a full GIRF from suitable combinations of input functions. The method is demonstrated by GIRF measurements on a 3T whole-body human MRI system and validated by comparing measured field evolutions with GIRF-based predictions.

2.2 Theory and Methods

Probing an LTI system

For a linear time-invariant system the relation between the input to the system, *i(t)*, and its output, *o(t)*, is determined by the impulse response, *h(t)*, as described by (37):

$$o(t) = \int_{-\infty}^{\infty} i(\tau) \cdot h(t-\tau)\, d\tau \quad \xleftrightarrow{FT} \quad O(\omega) = I(\omega) \cdot H(\omega) \text{, [2.1]}$$

where *t* and ω denote time and angular frequency, and $O(\omega)$, $I(\omega)$, and $H(\omega)$ represent the Fourier transforms (*FT*) of *o(t)*, *i(t)*, and *h(t)*, respectively. Accordingly, the system response to any given input can be predicted based on the impulse response function. Knowing the impulse response function thus amounts to having full information about the behavior of the system, within its range of linearity, and the task of characterizing a linear system amounts to determining its impulse response.

To do so by measurement, the output of the system must be observed for known input, requiring an appropriate measurement technique. The impulse response function can then be obtained by deconvolution of the measured output by the input, which can be efficiently performed by division in the frequency domain. Let $\hat{O}(\omega) = O(\omega) + \eta(\omega)$ denote the observed output, including the measurement noise *η(ω)* of standard deviation *σ(ω)*. Then the resulting estimate of *H(ω)* is

$$\hat{H}(\omega) = \frac{\hat{O}(\omega)}{I(\omega)} = \frac{O(\omega) + \eta(\omega)}{I(\omega)} = H(\omega) + \frac{\eta(\omega)}{I(\omega)} \qquad [2.2]$$

with the signal-to-noise ratio

$$SNR_{\hat{H}}(\omega) = \frac{|H(\omega)| \cdot |I(\omega)|}{\sigma(\omega)} \quad .$$

[2.3]

$I(\omega)$ should therefore be large and ideally contain equal amplitudes of all frequencies in the bandwidth of interest. A perfect Dirac delta function would evenly cover an infinite bandwidth but is not a feasible input for a real-world gradient system. In modern MR systems, the gradient input is typically defined digitally with a finite dwell time and is subject to limitations in terms of the maximum amplitude and slope of the gradient waveform. Under these constraints, a feasible approximation of a Dirac delta function is a short triangle pulse. A triangular function can be described as the convolution of two identical boxcar functions:

$$i(t) = p \cdot \left(box_T * box_T \right)(t) = \begin{cases} p \cdot (T - |t|), & |t| \leq T \\ 0, & |t| > T \end{cases}$$

[2.4]

where box_T has length T and amplitude 1, and p is the slope of the triangle (Fig. 2.1). In the frequency domain, a triangular input thus corresponds to a squared sinc function,

$$I(\omega) \propto p \cdot \frac{\sin^2(\omega T/2)}{\omega^2} \quad ,$$

[2.5]

which has several relevant properties with respect to the choice of its parameters. Firstly, as can be seen from Eq. [2.5], the envelope of the sinc-squared is determined by the slope, p, of the triangle. To optimize the sensitivity of the measurement, the slope should therefore generally be maximized. Secondly, the amplitude of the main lobe of $I(\omega)$ scales with the total moment of the pulse:

$$I(0) \propto \int_{-\infty}^{+\infty} i(\tau) d\tau = p \cdot T^2 \quad ,$$

[2.6]

and thirdly, the sinc-squared input exhibits zeros with a spacing that scales inversely with the length of the triangle:

$$\omega\big|_{I=0} = \frac{2\pi n}{T}, \quad n = \pm 1,2,3... \quad .$$

[2.7]

44

These zeros amount to blind spots in the measurement. Therefore, in the choice of the triangle length, a trade-off needs to be made between the bandwidth covered by the main lobe, which is larger for a shorter pulse, and the sensitivity at low frequencies, which increases strongly with the pulse duration.

This dilemma can be circumvented by employing multiple triangular pulses of different length, giving complementary response information. When using multiple input functions, the data obtained in the different measurements need to be combined in calculating $\hat{H}(\omega)$. A least-squares estimate at each frequency is obtained by

$$\hat{H}(\omega) = \frac{\sum_j I_j^*(\omega) \cdot \hat{O}_j(\omega)}{\sum_j \left| I_j(\omega) \right|^2} = H(\omega) + \frac{\sum_j I_j^*(\omega) \cdot \eta_j(\omega)}{\sum_j \left| I_j(\omega) \right|^2} \text{, [2.8]}$$

where $I^*(\omega)$ denotes the complex conjugate of $I(\omega)$, and the index j counts the different input functions. Assuming equal noise levels and no noise correlation between the different measurements, the variance of the noise term in Eq. [2.8] sums up to

$$\sigma_{\hat{H}}^2(\omega) = \frac{\sigma^2(\omega)}{\sum_j \left| I_j(\omega) \right|^2} \text{,} \qquad [2.9]$$

yielding the net SNR

$$SNR_{\hat{H}}(\omega) = \frac{\left| H(\omega) \right| \cdot \sqrt{\sum_j \left| I_j(\omega) \right|^2}}{\sigma(\omega)} \text{.} \qquad [2.10]$$

As seen from Eq. [2.10], the SNR of the combined measurement is governed by the spectral root-sum-of-squares profile of the set of input functions and by the basic noise level of the individual measurements. Based on this relationship, the specific choice of input waveforms can be made according to the desired sensitivity profile. To boost net sensitivity, certain or all waveforms may be performed
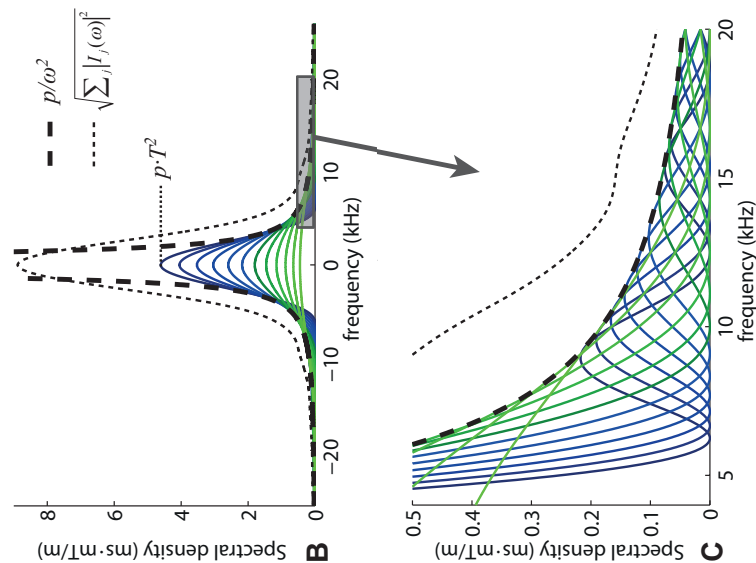
Fig. 2.1: *The set of triangular input functions used for GIRF measurements, shown in the time-domain (A), and corresponding sinc-squared functions in the frequency-domain (B). The frequency-domain plot includes the envelope of the side-lobes falling off with p/ω^2, and the root-sum-of-squares of all inputs, indicating the combined sensitivity of the set of input functions. A zoom of the side-lobes is plotted in (C), showing how the different input functions complement each other in terms of frequency content.*

multiple times, yielding an additional SNR gain by implicit averaging through the summation in Eq. [2.8].

As described so far, the proposed approach is geared to determining the self-response of any actuated field component, which may be a gradient field, a shim field, or else. However, it can readily be extended to incorporate cross-responses of undesired spatial field patterns as well. To this end, the magnetic field response in the magnet bore is expanded into a suitable set of spatial basis functions, which each constitute a separate output channel. Conversely, each control input of the system forms a separate input channel. For a gradient system, three input channels are considered, one each for the x, y and z gradients. On this basis, individual impulse response functions are introduced for each pair of input channel l and output channel m, yielding the complete description

$$o_m(t) = \sum_l \int_{-\infty}^{\infty} i_l(\tau) \cdot h_{l,m}(t-\tau) d\tau$$

$$\xleftrightarrow{\;FT\;}$$

$$O_m(\omega) = \sum_l I_l(\omega) \cdot H_{l,m}(\omega)$$

[2.11]

Given the capability to record the different outputs simultaneously, the multiple-channel impulse response can be determined simply by repeating the response measurements for each input channel. The resulting observations $\hat{O}_{m,j}^{(l)}(\omega)$ yield

$$\hat{H}_{l,m}(\omega) = \frac{\sum_j I_{l,j}^*(\omega) \cdot \hat{O}_{m,j}^{(l)}(\omega)}{\sum_j \left| I_{l,j}(\omega) \right|^2}$$

[2.12]

with SNR as derived in Eq. [2.10].

Dynamic field camera

Measurements of magnetic field responses were performed with a third-order dynamic field camera (35), using the field monitoring methodology described in (7). In short, NMR probes (6,38) are used to sense the magnetic field dynamics at a set of different positions with high temporal resolution. The actual observable of each probe is the

phase of its NMR signal, which is proportional to the integral of the magnetic field magnitude at the probe position. Based on knowledge of the probe positions, the spatiotemporal field evolution is then expressed in terms of the previously chosen spatial basis functions. The resulting time-varying coefficients, $\hat{k}_m(t)$, indicate the observed phase accumulated due to fields of the respective spatial structure. The time-derivative of the phase coefficients gives corresponding field coefficients, which constitute the observed multiple-channel field output according to Eq. [2.11]:

$$\hat{o}_m(t) = \frac{1}{\gamma} \frac{d\hat{k}_m(t)}{dt} \ , \qquad\qquad [2.13]$$

where γ is the gyromagnetic ratio of the NMR-active nucleus in the probes. To fully determine the chosen spatial model, the number of field probes must be equal to or larger than that of basis functions and the probes must be placed appropriately to permit a well-conditioned fit. The temporal resolution of the measurement is limited only by the acquisition bandwidth of the spectrometer used and the length of individual field observations is limited by the signal life-time of the NMR probes.

The dynamic field camera consisted of 16 unshielded transmit-receive NMR probes based on water samples of 0.8 mm in diameter, permitting field observations up to k values of approximately 11,000 rad/m (6,7). The water was doped with 3.3 g/l of $CuSO_4$ to reduce T_1 for fast re-excitation, while keeping T_2 long enough to maintain a signal life-time of about 100 ms. The probes were evenly distributed on the surface of a sphere of 20 cm in diameter. Their positions were determined by measuring NMR frequency shifts under static gradients of 2.5 mT/m in the x, y, and z directions, respectively.

GIRF measurements

In the present work, real-valued spherical harmonics up to full 3rd order were used to represent phase and field responses (Table 2.1). In total, this expansion comprises 16 basis functions, matching the number

Nr	Spherical harmonic	Order
0:	1	0
1:	x	
2:	y	1
3:	z	
4:	xy	
5:	zy	
6:	$2z^2 - (x^2 + y^2)$	2
7:	xz	
8:	$x^2 - y^2$	
9:	$3yx^2 - y^3$	
10:	xyz	
11:	$5yz^2 - y(x^2 + y^2 + z^2)$	
12:	$2z^3 - 3z(x^2 + y^2)$	3
13:	$5xz^2 - x(x^2 + y^2 + z^2)$	
14:	$z(x^2 - y^2)$	
15:	$x^3 - 3xy^2$	

Table 2.1: *Real-valued spherical harmonics used as spatial basis functions*

of available field probes. The single 0th-order function captures the uniform component of phase and field, whereas the three 1st-order harmonics represent linear gradients in the x, y, and z directions. For better readability, the first-order phase ($\hat{k}_1, \hat{k}_2, \hat{k}_3$) and field ($\hat{o}_1, \hat{o}_2, \hat{o}_3$) responses will be equivalently referred to by the common notations k_x, k_y, k_z and G_x, G_y, G_z.

Measurements were performed on a 3T Philips Achieva whole-body system with a maximum gradient strength of 40 mT/m and a slew rate limit of 200 mT/m/ms. Gradient responses were acquired with and without built-in eddy-current compensation and cross-term correction. The dwell time for discrete definition of the gradient waveforms was 6.4 μs. To avoid significant discretization errors, the shortest triangular gradient pulse used had a time-to-peak of 50 μs. Such a pulse has the first spectral zero at 20 kHz where the system response is still non-negligible. Therefore, a combination of different pulse lengths was

necessary. Overall, 12 triangular waveforms were used with a slope of $p = 180$ mT/m/ms and time-to-peak T ranging between 50 μs and 160 μs at increments of 10 μs (Fig. 2.1). The slope was chosen large for high sensitivity while keeping it well within the system's specified range. The moment of the longest pulse was around 1200 rad/m and thus well within the observable range of the NMR field probes.

In each of the response measurements, signal acquisition from the field probes was started 5 ms before the nominal start of the gradient pulse, and had a duration of 68 ms, yielding a frequency resolution of about 14.7 Hz. The primary sampling bandwidth was 398 kHz and thus amply above the expected response bandwidth. The repetition time of the acquisitions was 2 seconds to allow for field settling between the individual measurements. Each of the 12 triangular inputs was performed 50 times per gradient channel. This results in a measurement time of 20 minutes for one gradient channel and a total of one hour for all three gradient channels. From each individual set of probe signals, field outputs were calculated according to Eq. [2.13]. All field outputs were then combined to yield the GIRF using Eq. [2.12]. The whole procedure was performed separately for the x-, y-, and z-gradient channels. To verify the measured GIRFs, they were used to predict field responses to selected gradient inputs according to Eq. [2.11]. The predictions were then compared with direct measurements of the responses to the same gradient inputs. The gradient waveforms used for validation were a set of triangular pulses of 0.05 ms to 3.2 ms time-to-peak and 1 mT/m to 31 mT/m amplitude, and an EPI readout sequence (45 echoes, resolution = 2.5 mm, acquisition time = 62.5 ms). To actually probe the LTI assumption and accuracy of the GIRFs, the lengths of the triangular validation pulses were different from and partly much larger than those used for the GIRF measurement. The EPI was included to confirm that the linear model holds also for a full gradient sequence including both triangular and trapezoidal pulse shapes.

2.3 Results

GIRF measurements

Magnitude and phase plots of the measured GIRFs in the frequency domain are shown in Fig. 2.2. By design, the gradient chains exhibit overall low-pass characteristics. The built-in eddy-current compensation broadens the response plateaus at low frequencies and aligns the responses of the three gradient subsystems. With compensation, the bandwidth at -3 dB is around 4.6 kHz, with the response tapering off toward zero at around 22-25 kHz. As can be seen in the plot, the noise in the GIRF measurement increases considerably toward higher frequencies where the power of the input waveforms is low. The phase response of the x and y gradients around DC is essentially flat up to ~400 Hz, with eddy current compensation. The corresponding z-gradient phase response exhibits a minor slope at low frequencies indicating a residual group delay of -0.5 µs close to DC. The virtual absence of group delay in all three channels reflects appropriate delay calibration, which consists in constant shifts of the nominal time of the gradient chains relative to that of the acquisition subsystem.

At low frequencies, the GIRFs show channel-specific patterns of distinct peaks with amplitudes up to around one percent of the full response. The x and y gradients exhibit several such peaks between 600 Hz and 1800 Hz while the GIRF of the z gradient shows mainly one rather narrow peak at 1300 Hz (Fig. 2.2). Based on their frequency range, amplitudes, and widths, these peaks are ascribed to mechanical resonances of the gradient coils. This interpretation is supported by a preceding acoustic observation of the single resonance at 1300 Hz (35). Acoustic responses at similar frequencies have also previously been noted in the literature (12,25).

The prominent GIRF peaks at 25 kHz reflect the transistor switching frequency of the gradient amplifiers. The switching events cause slight modulation peaks at the switching frequency. However, these modulation peaks are not related to the actual input at 25 kHz, and are consequently misinterpreted in the GIRF calculation. As the input at
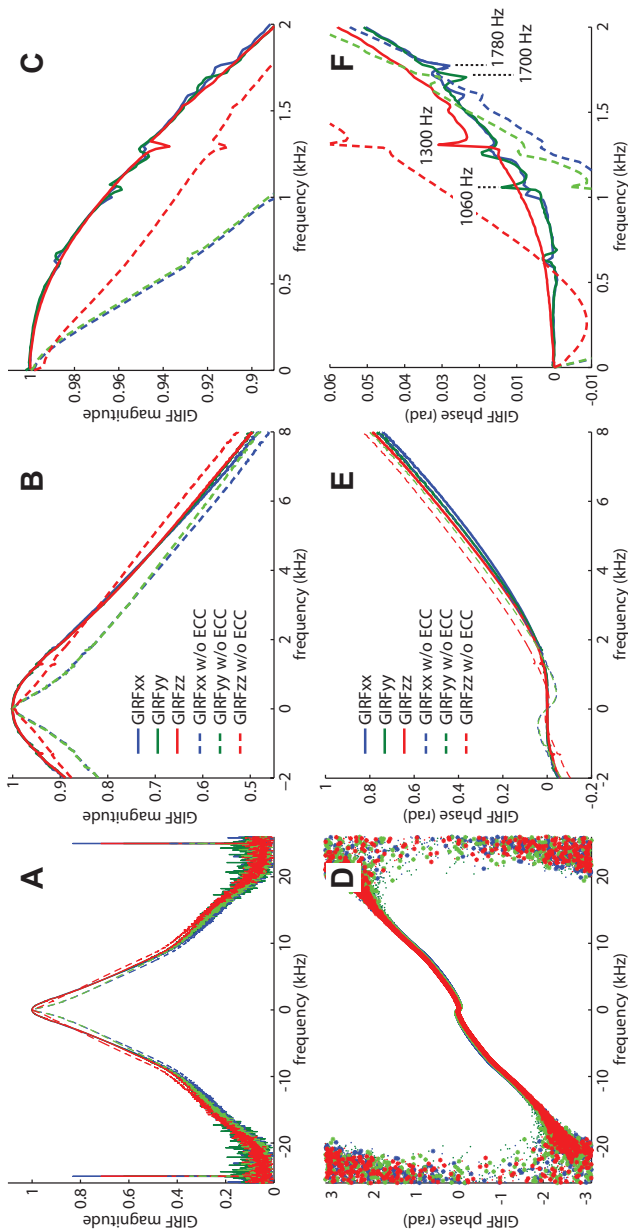
Fig. 2.2: *Magnitude (**A**, **B**, **C**) and phase (**D**, **E**, **F**) of measured GIRFs for all three gradient directions, with and without built-in eddy current compensation (ECC). The low-pass characteristic of the gradient system is apparent in (**A**). Details of the responses in (**B**) show how the eddy current compensation serves to broaden the response plateau and align the responses of the three different gradient channels. In a further zoom of the magnitude (**C**) and phase (**F**) plots, several mechanical resonances are apparent at low frequencies. Flat phase at low frequencies reflects near-zero net delay.*
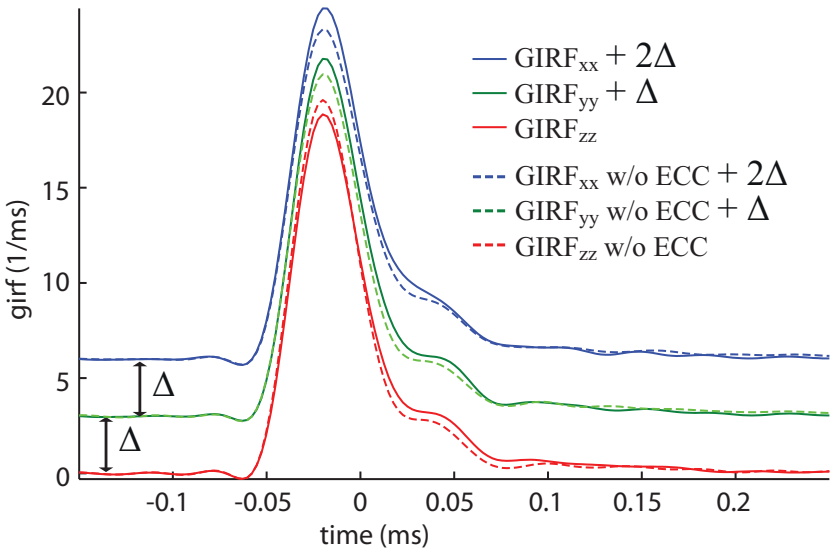
Fig. 2.3: *Time-domain representations of the GIRFs in all three gradient directions, with and without eddy current compensation (ECC). Vertical shifts (Δ) serve for better comparison of the GIRFs of the different gradient channels.*

25 kHz is extremely small, division according to Eq. [2.8] causes the small switching artifact to appear with large amplitude in the GIRF.

Figure 2.3 shows plots of the three impulse responses, with and without eddy current compensation, in the time domain, filtered with a low-pass filter (raised cosine, 60 kHz FWHM, 12 kHz transition band) to reduce high-frequency noise. The response kernels rise slightly more quickly than they fall and exhibit somewhat delayed second lobes, which are more pronounced for the y and z gradients. For the x and y gradients, the peak amplitude of the pre-emphasized responses is somewhat higher than without the eddy current compensation, whereas for the z gradient, the opposite is observed. From this representation, the width of the time-domain kernels was estimated at approximately 40 μs with peaks at around -20 μs. The presence of a gradient response at t<0 implies that a gradient field is observed before the nominal start of the

gradient. This occurs as a result of the MR system's aforementioned delay correction, which advances the nominal gradient time to play out gradient waveforms slightly sooner.

Selected cross-responses are shown in Figure 2.4, scaled to percent of the input. To compare field distributions of different spatial order, the basis functions were normalized to unit maximum field within a sphere of 20 cm diameter, centered at gradient isocenter (39). For instance, a linear field of 10 mT/m amounts to 1 mT in the normalized representation and is thus comparable to a 0th-order field of 1 mT as they both produce the same maximum field shift within the defined sphere.

The cross-responses were generally on the order of 0.1% or less for all three gradient chains, except at specific resonances and in the B_0 term where it reached 1% for x-gradient input. In Fig. 2.4, several distinct cross-peaks can be seen at previously observed mechanical resonance frequencies of the respective gradient channel. In the x response to z-gradient input there is a peak at the 1300 Hz resonance of the z gradient while the B_0 and the higher-order $2z^2 - (x^2 + y^2)$ ($\hat{o}_6$) terms both contain a resonance of the x gradient at 1780 Hz, and the $5yz^2 - y(x^2 + y^2 + z^2)$ ($\hat{o}_{11}$) term shows a resonance of the y gradient at 1700 Hz. The y response to x-gradient input shows peaks at 1060 Hz and 1750 Hz, both of which are less pronounced as resonances of the x gradient, the former however being a strong resonance in the self-response of the y gradient. Peaks at 1060 Hz appear in several higher-order field terms as well (data not shown), however only as responses to x-gradient inputs and not to the y gradient. A speculative explanation for this appearance of a resonance more strongly related to the y gradient than the driving x gradient may lie in the proximity of the two gradients and the shared structure embedding them both. Switching the x gradient may induce vibrations that propagate through the surrounding structure, and decay more slowly in the y-gradient coil than in the x-gradient coil. The details, however, of how different vibrational modes are maintained, and how they affect the field inside the scanner remain to be investigated. The small distinct peaks seen at DC in several of the cross terms largely stem from slow system drifts unrelated to gradient inputs as well as residual susceptibility broadening of the field probe samples (6), which mimics slight field variation at very low frequencies.
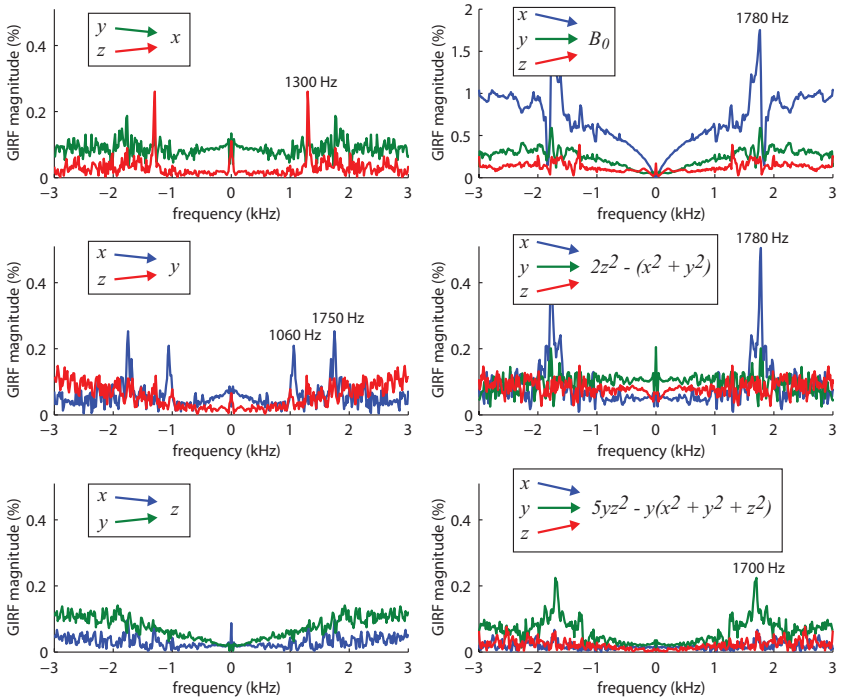
Fig. 2.4: *Measured cross-responses of the x, y, z, B_0, $2z^2$ - $(x^2 + y^2)$ and $5yz^2$ – $y(x^2 + y^2 + z^2)$ field terms due to operating the x- (blue), y- (green) and z-gradients (red), expressed in percent of the input. Several distinct peaks coincide with mechanical resonances previously identified in the self-responses (Fig. 2). Note the different scaling in the B_0 plot.*
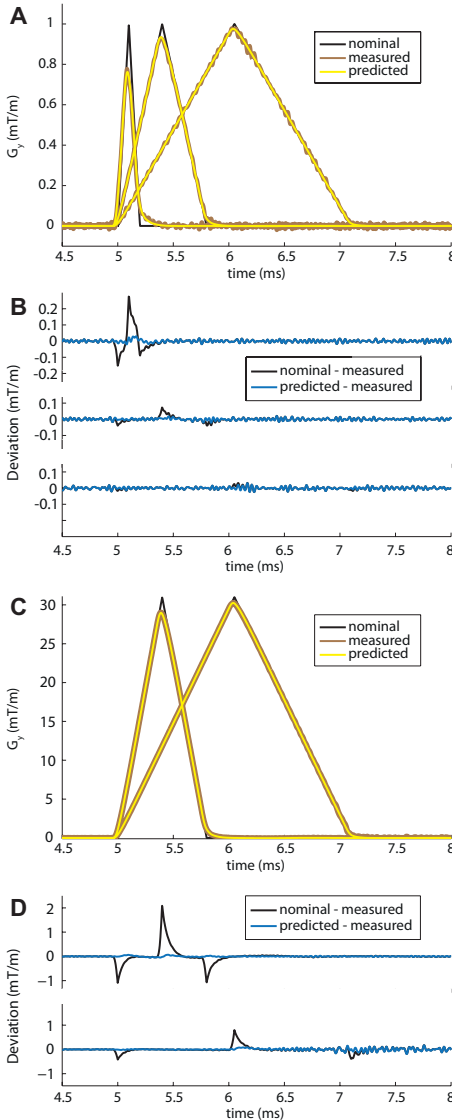
GIRF-based predictions

Figure 2.5 shows predictions of triangular gradient pulses with a time-to-peak T of 0.1, 0.4 & 1.05 ms, and peak amplitudes of 1 mT/m (Fig. 2.5A) and 31 mT/m (Fig. 2.5C), compared to nominal and directly measured (filtered to 60 kHz FWHM) pulses. Error plots of nominal vs. measured, and predicted vs. measured gradients are plotted for each pulse (Fig. 2.5B,D). For shorter pulses, the actual gradient deviates more from the nominal waveform than for longer ones, which is expected due to the weaker response at higher frequencies. The directly measured pulses follow the predictions closely with a maximal prediction error of about 0.2% of the pulse amplitude. Due to different dynamic ranges, the measurement noise appears more prominently in the upper plot. Increased noise toward the end of the 31 mT/m, 1.05 ms pulse, as seen in the error plot (Fig. 2.5D), was caused by nearly complete de-phasing of the field probes in the validation measurement. The size of the NMR field probes thus limits the capability of validating predictions of large gradient pulses by single direct measurements. It does not, however, hinder GIRF-based predictions of large gradients *per se*.

To study subtle long-term features of the gradient response, Fig. 2.6A shows a detail of the first 15 ms after a gradient pulse (30 mT/m amplitude, $T = 0.25$ ms). In the prediction, a distinct oscillatory pattern is seen long after the pulse, reflecting the subtle resonance peaks in the underlying GIRF. The direct measurement, however, was too noisy to confirm the oscillations on this small scale. To see them more clearly, Fig. 2.6B shows the phase accumulated under the same gradient pulse. The underlying integration suppresses high-frequency noise and thus reveals the oscillations also in the direct measurement. It is now apparent that the predicted and the measured patterns again agree closely.

The accumulated phase, expressed as the k-space position, is also the key parameter underlying MR image encoding and reconstruction. In Fig. 2.7, the measured GIRFs are used to predict a whole EPI readout sequence in terms of its effective gradient waveforms (left) and k-space trajectory (right). The directly measured trajectory again shows good accordance with the prediction, following it closely

throughout, including the turns where it deviates significantly from the nominal trajectory.

Fig. 2.5:
*GIRF-based predictions of gradient blips of 1 mT/m peak amplitude, T = 0.1, 0.4, 1.05 ms (**A**) and 31 mT/m peak amplitude, T = 0.4, 1.05 ms (**C**), compared with nominal and directly measured gradient waveforms. For each pulse, the differences between nominal and measured (black) as well as predicted and measured (blue) traces are plotted in (**B**, **D**). The prediction error amounts to maximally 0.2% of the gradient amplitude.*

Fig. 2.6:
Nominal, measured, and predicted waveforms of a triangular gradient pulse (30 mT/m peak amplitude T = 0.25 ms) in field (top) and accumulated-phase (bottom) representation. The zoomed insets on the right show details of the system response over about 15 ms after the pulse. As seen there, the GIRF predicts subtle oscillations after the pulse, which cannot be distinguished from noise in the direct field measurement. They are largely confirmed, however, by plots of the corresponding phase coefficient, k_y, in which high-frequency noise is attenuated by integration over time.
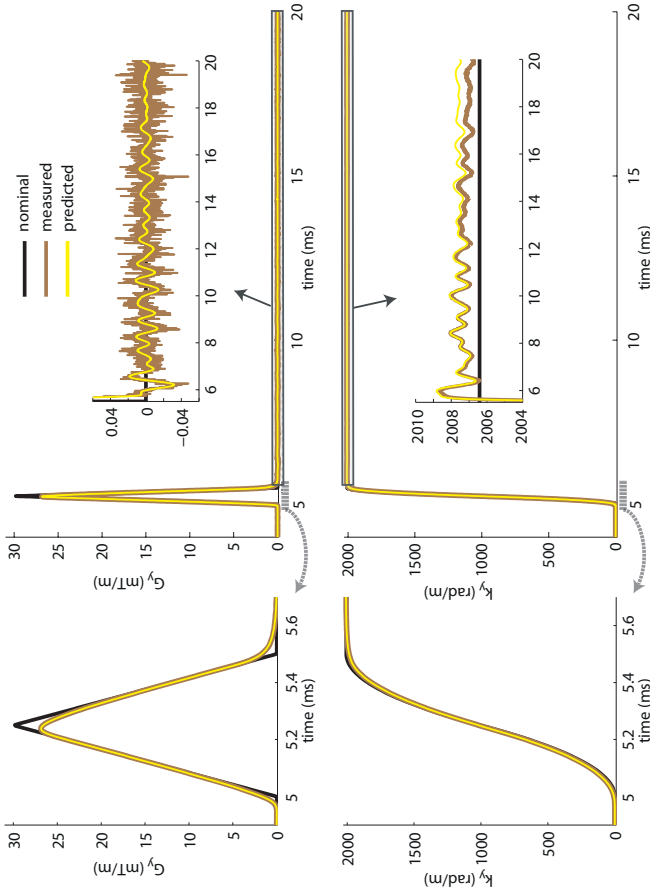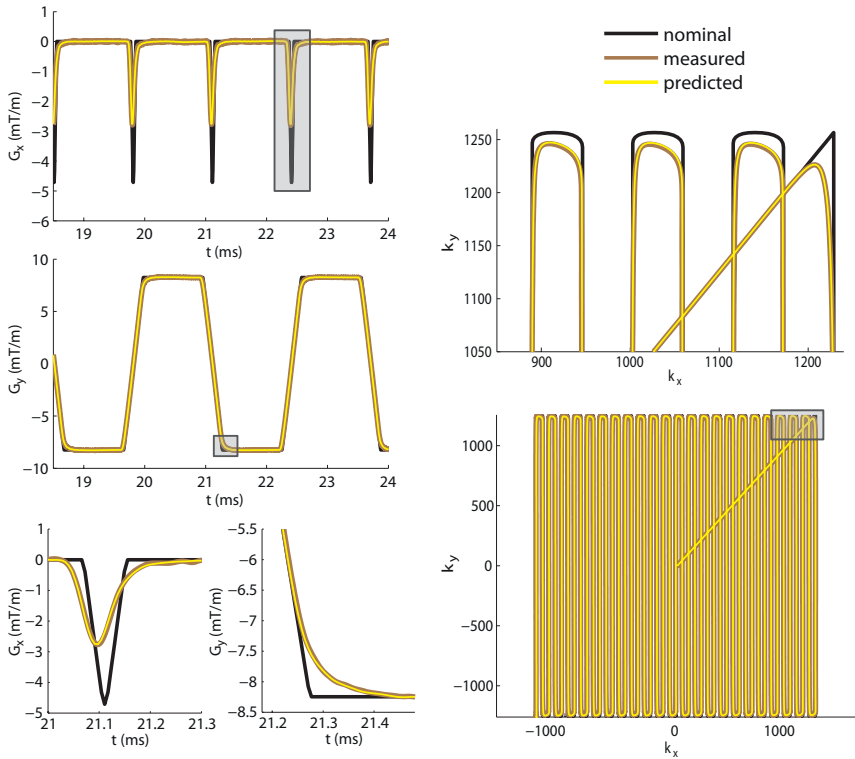
Fig. 2.7: *Nominal, measured, and predicted gradient time-courses during an EPI readout sequence (**left**). Zoomed details show one of the phase-encoding blips and the settling of a frequency-encoding gradient (**bottom left**). The resulting full k-space trajectories are shown on the **right**, including a detail of one of the k-space corners including the end of the pre-phaser gradient*

2.4 Discussion

The impulse response function of a linear time-invariant system is a well-known and much used concept in engineering. Here we have investigated the feasibility of determining the impulse response functions of the gradient chains of an MR system. The investigation concerned each gradient chain as a whole between the two endpoints that are relevant for the user, i.e., between gradient waveform definition at the console and the actual magnetic fields seen by an object placed in the scanner bore. Using a third-order dynamic field camera based on NMR probes and a set of input functions that are easily implemented in standard scanner software, the impulse response measurement has proven a straightforward and fast procedure, yielding highly accurate results.

When defined as above, GIRFs constitute a composite response reflecting all linear distortions that a gradient waveform undergoes between the software interface of the scanner and the resulting magnetic fields. This includes software signal processing, eddy-current compensation, gradient amplifier characteristics, potential cable effects, coil characteristics, coil coupling, eddy currents, and mechanical responses of the gradient system. Several features of the measured GIRFs have been linked to underlying phenomena. To fully understand how each stage of a gradient chain acts upon the waveform, the input and output of that stage would need to be measured. Measuring the combined response, as done here, is a fast and comprehensive way of characterizing how a gradient system performs as one entity.

Applications

Knowledge of the gradient impulse response can be beneficial in a variety of ways. Most immediately, it forms a comprehensive basis of tuning the gradient response by pre-emphasis. Existing methods of eddy current compensation commonly rely on a limited number of exponentially decaying correction terms found by time-domain fitting. With the GIRFs, corresponding fits can be based on a complete picture of the native response in the frequency domain (40), including correction for mechanically induced field oscillations. Knowledge of the

GIRF also permits pre-emphasis by a general filter equal to the frequency-domain ratio of the desired system response and the GIRF. In this fashion, LTI theory can be deployed to shape the net system response comprehensively within the technical limitations of the available gradient hardware.

More generally, fast GIRF measurement may be useful for the calibration and quality assurance of gradient systems and as a diagnostic tool in cases of suboptimal gradient performance. As shown in this work, known GIRFs can also be used to calculate the actual gradient output that is obtained with any given pulse sequence. Given sufficient system stability, image reconstruction may thus be based on actual k-space trajectories and higher-order encoding (33) without the need for sequence-by-sequence field monitoring. Calculated field evolutions may also yield more accurate accounts of specialized signal preparation such as, e.g., in phase-contrast methods (41). In some situations, retrospective correction for field imperfections is not or hardly feasible. This is true, for instance, for spatially selective excitation based on k-space trajectories played out during RF transmission. In these cases, GIRF-based predictions could serve as a basis for designing trajectories such that they can be realized perfectly with a suitable pre-compensated demand.

Model limitations

The LTI approach is only valid to the extent that the system considered is actually linear and time-invariant. Although typically minor, there are a number of influences on gradient responses that are non-linear or vary over time. Power amplifiers generally exhibit non-linear behavior to varying extent and procedures to linearize the output are a standard part of gradient amplifier engineering. Gradient responses also depend somewhat on the thermal state of the system. High-gradient-duty-cycle scans, such as for fMRI or diffusion imaging, heat up the gradient coils and supporting structures. Ensuing changes in electrical and mechanical properties will cause the gradient response to change slightly over time. Likewise, any other structures that support eddy currents may slightly heat up and thus change their eddy current characteristics. In as far as the heating is caused by driving the gradients themselves, it could be

seen as an extension to the response of the system, which will however generally be non-linear. There may also be external factors that influence the net field independently of how the system is driven and are thus inherently non-linear. Any perturbation from the environment, such as fields produced by other electrical equipment, nearby traffic or power lines fall into this class. Nonetheless, as long as these model violations are suitably small, the LTI approach permits useful approximations of the system behavior. In this work, the validity of measured GIRFs and thus of the underlying LTI picture has been demonstrated by predictions of effective gradient waveforms. For a variety of gradient inputs, a high degree of prediction accuracy was achieved with a maximal error on the order of 0.2% of the pulse amplitude. Moreover, preliminary data indicate good stability of the system response over years.

Mechanical oscillations & cross-terms

Among the features that the measured GIRFs capture and predict well are field oscillations due to mechanical vibrations. Judging by the achieved prediction accuracy, such oscillations appear to behave largely linearly. Understanding these effects in more detail will require models of how mechanical displacements in the system translate into field changes. Such studies are beyond the scope of this work. However, the observed agreements in vibration peaks between self-, cross-, and higher-order responses indicate that GIRF measurements will be instrumental in elucidating these mechanisms. Cross-responses via eddy currents are pronounced with unshielded gradient or shim coils, which couple strongly to the cryostat. In this situation, measurements of the cross-responses could form the basis of cross-pre-emphasis and higher-order image reconstruction (39). In the present work, a field camera with 16 NMR probes permitted GIRF measurements of full 3rd order in terms of spherical harmonics. Further discrimination of field responses up to arbitrary spatial order could be readily achieved provided a suitable number and distribution of field probes.

Sensitivity & resolution

The sensitivity of the GIRF measurement has been shown to depend on the set of input functions used and on the noise level of individual field measurements. Triangular pulses offer the highest spectral sensitivity close to DC. Toward higher frequencies, their net sensitivity drops approximately as $1/\omega^2$ as seen from Eq. [5]. The transition from phase data to field data further emphasizes high-frequency noise since taking the temporal derivative corresponds to multiplication by ω in the frequency domain. Jointly, these effects caused the GIRF sensitivity to drop as $1/\omega^3$ overall.

A straightforward way of increasing the overall SNR is to acquire averages of the field response measurements. To specifically increase sensitivity at higher frequencies, sinusoidally modulated pulses could be used in principle, shifting the spectral main lobe away from DC. To keep with slew rate limitations, however, the slope of a pulse to be modulated with a sinusoid would need to be kept lower than the system maximum, thereby reducing the total power of the pulse. For this reason, the sensitivity of a single measurement at a high frequency will necessarily be lower than what can be achieved around DC with the corresponding unmodulated pulse. The optimal choice of input pulses ultimately depends on the desired sensitivity profile for the system to be measured. Equations 8 and 12 describe how to obtain a least-squares estimate of the GIRFs based on the sensitivity profile of each input pulse, and hold for any combination of modulated and unmodulated pulses alike. Combining simple triangular pulses as done here offers the advantage of straightforward implementation on standard MR equipment.

In this work, the gradient response measurements covered 68 ms, yielding a frequency resolution of 14.7 Hz. Particularly for unshielded gradient coils it is known that significant eddy currents may persist for several hundreds of milliseconds (17), thus exceeding the range possible to capture in one single measurement with the field camera used in this work. To overcome this, multiple response measurements with interleaved timing can be acquired (40), which however comes at the expense of increasing the total time required for

the measurements. With hardware able to perform continuous field monitoring, as described by (42), long-living responses could be captured straightforwardly.

Measurement time

The time required for measuring GIRFs with the proposed approach depends on the total number of input pulses and the time allowed for gradient settling between pulses. The aim of the measurements presented here was to elucidate even subtle behavior of the gradient responses, to which end a large number of averages was acquired. For three gradient channels, the total measurement time amounted to approximately one hour. For a coarser measurement, even one observation of each pulse would suffice, reducing the measurement time to about a minute. Initial experience suggests that even such coarser GIRFs yield useful predictions of gradients and trajectories. This is largely due to the fact that common input gradient waveforms have most power at relatively low frequencies where the SNR of the measured GIRF is favorable.

2.5 Conclusion

GIRF measurements with a third-order dynamic field camera enable fast and easy determination of gradient system characteristics. Among others, GIRFs measured in this way readily reveal subtle field oscillations due to mechanical resonances. These have been found to be largely linear and time-independent in experiments without significant gradient heating. GIRFs also permit highly accurate predictions of net system behavior. Such predictions will be useful for image reconstruction and gradient waveform optimization. Notably, suitable sets of field probes straightforwardly yield GIRFs up to high spatial order along with the common gradient responses. This capability renders the proposed approach promising also for the characterization of dynamic shim systems. The GIRF concept assumes linearity and time-independence of the system to be characterized but is otherwise free of mechanistic assumptions. For more advanced models incorporating,

e.g., thermal or non-linear electro-mechanical effects, response measurements with a dynamic field camera will still be instrumental.

Chapter 3

Field Camera Measurements of Gradient and Shim Impulse Responses Using Frequency Sweeps

3.1 Introduction

The use of linear gradient fields that are operated dynamically in the kHz range is one of the core features of MRI. It is primarily needed to encode spatial information and image contrast, and many applications require extremely high precision in the timing and waveform shape of the gradients to avoid artifacts. Several challenges arise when it comes to achieving optimal dynamic performance of the gradient system. The field dynamics are affected by a multitude of factors, including electrical properties of the gradient coils and power amplifiers, eddy currents induced in the cryostat and other conducting structures of the scanner, mechanical vibrations of the coils, coil coupling, etc. Eddy currents, especially, have been among the major challenges in gradient engineering, and efforts to control these have led to actively shielded coils (43–45) and pre-emphasis filters applied to the gradient waveforms (46,17). Despite the work that has gone into improved gradient design, advanced trajectories, such as EPIs and spirals, still suffer from field imperfections (47,48), and eddy currents can cause significant artifacts in applications like diffusion and spectroscopy (19,49). Another important class of field perturbations is field oscillations caused by mechanical vibrations of the gradient coils at gradient switching. These induce side-band artifacts in spectroscopy, and can also affect phase-sensitive applications such as flow measurements (12,41).

In addition to the linear gradient fields, many commercial scanners include 2nd- or higher-order shim coils, intended for semi-static use to compensate for B_0-inhomogeneities within the imaging object. In recent years however, the benefits of driving also higher-order fields dynamically, in order to improve B_0-homogeneity, or to gain degrees of freedom for the signal encoding, are being increasingly explored (50–56). This puts similar requirements on dynamic performance of the higher-order fields as for the gradient fields. Like the gradients, the shim fields are affected by a variety of mechanisms, including amplifier and coil characteristics, eddy currents and mechanical vibrations. In present-day scanners, the higher-order shim coils are generally not shielded, and long-living eddy currents are therefore a major limitation to applications of dynamic shimming (53–55). Shielding, however, comes at the cost of reduced scanner bore width, and is alone not enough to suppress all

relevant eddy currents, as seen for the gradients. Additionally, strong cross-term fields are observed for the higher-order shims, both statically and dynamically, which must be taken into account in the shim calculations (52,54,55).

Thus, there is still a need to address the issues of field fidelity associated with gradient and shim application, be it through hardware modifications, sequence adjustments or through image reconstruction and post-processing techniques. For any of these approaches, a key question is how to characterize the dynamics of the magnetic fields accurately and comprehensively. To this purpose, a technique for broadband characterization of the dynamic performance of a gradient system, based on measurements of the gradient impulse response function (GIRF), has recently been proposed (57,58). This relies on the system being largely linear and time-invariant – a justified assumption as the most significant factors affecting the field are linear by nature.

In this work, we perform a broadband characterization of the higher-order shim system of an MR scanner, using frequency-swept pulses as test functions to measure the shim impulse response functions (SIRFs). The characterization also includes the gradients, since they are used as 1st order shims. As in Ref. (57), the field measurements are performed with a dynamic field camera, yielding information on $0^{th} – 3^{rd}$ order spherical harmonic field terms simultaneously in each measurement. This thus provides a fast way of obtaining measurements of both self- and cross-term field responses to input in one shim channel.

To determine the GIRF/SIRF, a test function is given as input to the system and the field response is measured. Features of this test function, together with the SNR of the field measurement, determine the spectral sensitivity profile of the measurement. Advantages and drawbacks of different input functions to use for probing a linear time-invariant system have been investigated previously in other fields of engineering (59). For the GIRF/SIRF measurements, short triangular pulses and frequency sweeps have been employed successfully so far (57,58,60). Frequency sweeps have a number of advantages, which make them especially suited for the purpose. Here we do a theoretical analysis of properties of frequency-swept pulses for probing a linear time-invariant system. We investigate how the sweep affects the SNR of the determined system response, and put it into the practical context of

measuring the field response of an MR scanner. We further show that it is principally possible to design frequency-swept pulses such as to achieve any desired measurement sensitivity for any desired frequency interval.

3.2 Theory

Impulse response measurements

A linear time-invariant system is characterized by the impulse response function, *h(t)*, of the system. The output, *o(t)*, from the system, in response to any input, *i(t)*, is given by the convolution of *h(t)* with *i(t)*:

$$o(t) = \int_{-\infty}^{+\infty} i(\tau) \cdot h(t - \tau) d\tau \ . \tag{3.1}$$

An unknown *h(t)* can be determined by feeding a known input to the system and measuring the resulting output. The deconvolution can be performed as a division in the frequency domain:

$$\hat{H}(\omega) = \frac{\hat{O}(\omega)}{I(\omega)} \ . \tag{3.2}$$

Here *I(ω)*, *O(ω)* and *H(ω)* denote the Fourier transform of *i(t)*, *o(t)* and *h(t)*, respectively, $\hat{O}(\omega)$ being the measured response including noise, and $\hat{H}(\omega)$ the estimate of the true system impulse response, *H(ω)*. The input, *I(ω)*, is assumed to be noise-free in the following analysis. The noise in $\hat{H}(\omega)$ then scales inversely with the amplitude of the input at the respective frequency, as can be seen from:

$$\hat{H}(\omega) = \frac{O(\omega) + \eta(\omega)}{I(\omega)} = H(\omega) + \frac{\eta(\omega)}{I(\omega)} \ , \tag{3.3}$$

where *η(ω)* is the frequency-domain noise in the measurement of the output. Assuming *η(ω)* to be independent of the input, and be of zero-mean distribution with standard deviation $\sigma_O(\omega)$, the noise in $\hat{H}(\omega)$ will also have zero-mean distribution and a standard deviation of:

$$\sigma_{\hat{H}}(\omega) = \frac{\sigma_O(\omega)}{|I(\omega)|} \ . \tag{3.4}$$

If the system has more than one input and/or output channel, $\hat{H}(\omega)$ must be calculated separately for each combination of input and output channels. More than one pulse per input channel may also be used to probe the system, in which case the responses can be joined to compute $\hat{H}(\omega)$ by least-squares combination as described in (57):

$$\hat{H}_{l,m}(\omega) = \frac{\sum_j I_{l,j}^*(\omega) \cdot \hat{O}_{m,j}^{(l)}(\omega)}{\sum_j |I_{l,j}(\omega)|^2} \ . \tag{3.5}$$

Here, l counts the input channels, m the output channels, and j the separate input pulses. The noise in $\hat{H}(\omega)$ does in this case depend on the root-sum-of-squares of the different input pulses:

$$\sigma_{\hat{H}_{l,m}}(\omega) = \frac{\sigma_{O_m^{(l)}}(\omega)}{\sqrt{\sum_j |I_{l,j}(\omega)|^2}} \ . \tag{3.6}$$

Linear frequency sweeps

As is evident from Eqs. [3.4] and [3.6], $I(\omega)$ should ideally be large at all frequencies of interest, to estimate $H(\omega)$ with high sensitivity. Practically, this means that a broadband pulse with the energy equally distributed over all frequencies is optimal. One approach to achieve a large bandwidth in the input is to use a short delta-like pulse, such as a triangle or boxcar. The shorter the pulse, the wider is the main lobe of the frequency domain representation of the pulse. However, since the time domain amplitude is limited on a physical system, this approach inherently comes with a trade-off between bandwidth and total energy in the input.

Instead of exciting all frequencies simultaneously, as with a delta-like pulse, one can use a frequency-swept pulse to successively excite the different frequencies in the bandwidth. This has the advantage of spreading the energy of the input both in the time and in the frequency domain (Fig. 3.1AB), thereby allowing for arbitrary input
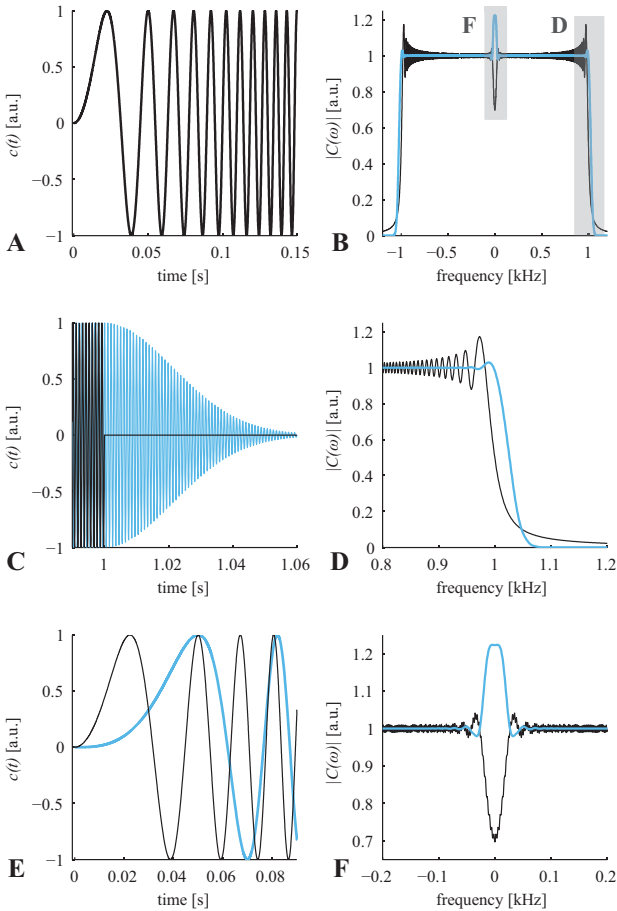
Fig. 3.1: *Comparison of a standard chirp pulse as in Eq. [3.9] (black) vs. a modified chirp (blue) in the time- and frequency domain. (**A**) shows a selection at the beginning of the standard chirp in the time domain, and (B) shows both pulses over the full bandwidth in the frequency domain. In the modified chirp, the amplitude step at the end of the sweep has been smoothed with a Gaussian shape to avoid the ripples in the spectral profile (**C,D**). At the start of the chirp, a frequency modulation with $\omega \propto t^2$ has been used to enhance the input at low frequencies (**E,F**).*

energy and bandwidth to be achieved by a suitably long frequency sweep. In the following paragraphs, the linear frequency sweep (chirp) will be discussed and analyzed for its properties as input function to determine an unknown system response, $h(t)$. A summary of the required steps for a chirp-based system characterization is shown in Table 3.1.

A chirp is a pulse modulated with a linearly increasing/decreasing frequency, $\omega(t)$:

$$\omega(t) = \frac{2\pi \cdot BW}{T_p} t + \omega_0, \quad 0 \leq t \leq T_p \; , \qquad [3.7]$$

where BW is the bandwidth of the frequency modulation, T_p is the pulse length and ω_0 the frequency at the start of the pulse. The sweep speed, β, can be defined as the time-derivative of the frequency modulation:

$$\beta = \frac{d\omega}{dt} = \frac{2\pi \cdot BW}{T_p} \; . \qquad [3.8]$$

On a real-valued system, the chirp, $c(t)$, can thus be written as:

$$c(t) = A \cdot \sin(\int_0^t \omega(\tau) d\tau)$$
$$= A \cdot \sin(\frac{\beta t^2}{2} + \omega_0 t), \quad 0 \leq t \leq T_p \qquad [3.9]$$

where $A(t)$ defines the pulse envelope, which for a regular chirp is generally a rectangular function. The pulse amplitude is limited by the specific hardware and should be chosen as large as possible for maximal sensitivity of the measurement. Amplitude restrictions may however vary with the frequency content of the input pulse. In order to keep with slew rate constraints on a gradient system, for instance, the amplitude must satisfy $A(t) \cdot \omega(t) \leq S_{max}$ at all times.

For a chirp with a rectangular pulse envelope the frequency-domain profile of the pulse is essentially flat. Intuitively, this can be understood as an equal amount of time, Δt, is spent in the vicinity of each frequency, $\Delta \omega$, of the sweep, thus distributing the pulse energy approximately equally over the bandwidth. The slower the sweep speed, the more time per frequency, and consequently more energy is deposited

into each frequency bin. Generally it holds that if the pulse envelope, $A(t)$, is sufficiently smooth, the magnitude of the Fourier transform of $c(t)$, $C(\omega)$, approximately depends on amplitude and sweep speed as (61):

$$\left| C(\omega) \right| \approx A(t_\omega) \cdot \sqrt{\frac{\pi}{2\beta}} \ , \qquad\qquad [3.10]$$

where t_ω is the time point at which the sweep passes through the frequency ω:

$$t_\omega = \frac{\omega - \omega_0}{\beta} \ . \qquad\qquad [3.11]$$

Both amplitude and sweep speed are real-valued, and will hereafter be assumed to be positive without loss of generality.

A slower sweep speed yields more input energy per frequency but also requires a longer pulse length, T_p, to cover the same bandwidth (Eq. [3.8]). The measurement of the system response to the input chirp must naturally cover the pulse length, T_p, plus additionally the length of the impulse response, T_h, to capture the response to the last frequencies in the chirp. The measurement time, T, thus relates to pulse length as:

$$T \geq T_p + T_h \ . \qquad\qquad [3.12]$$

The frequency resolution of the measurement is determined by T and is higher for a longer measurement. Also the total energy of the noise increases with a longer measurement, corresponding to the higher resolution in the frequency domain. A slower sweep therefore yields not only more input energy, but also a higher $\sigma_O(\omega)$. Scaling $\sigma_O(\omega)$ with $1/\sqrt{T}$ yields the square root of the noise power, here denoted by $\sigma_M(\omega)$, a measure independent of pulse length and characteristic for the specific measurement device:

$$\sigma_M(\omega) = \frac{\sigma_O(\omega)}{\sqrt{T}} \ . \qquad\qquad [3.13]$$

Combining Eqs. [3.4], [3.10] and [3.13] to estimate the noise content in $\hat{H}(\omega)$ when $C(\omega)$ is used as input to determine the system response yields:

$$\sigma_{\hat{H}}(\omega) \approx \frac{\sigma_M(\omega)}{A(t_\omega)} \cdot \sqrt{\frac{2\beta T}{\pi}} \qquad [3.14]$$

Seeing that the bandwidth of the pulse is proportional to βT_p (Eq. [3.8]), and using the inequality in Eq. [3.12] gives the following alternative expression for the noise:

$$\sigma_{\hat{H}}(\omega) \geq \frac{\sigma_M(\omega)}{A(t_\omega)} \cdot \sqrt{4BW} \quad, \qquad [3.15]$$

where equality holds when T_p is long compared to T_h, so that T is approximately equal to T_p.

For an estimate of $H(\omega)$ relying on a simple frequency domain division as in Eq. [3.2] with a chirp as input, the noise in $\hat{H}(\omega)$ is thus determined by the bandwidth of the chirp. However, an important point to note here is that the frequency resolution of $\hat{H}(\omega)$ is generally higher than necessary to accurately resolve features of the system response. To gain SNR in $\hat{H}(\omega)$ it is therefore justified to perform a frequency-domain smoothing with a kernel of width $\Delta f \leq 1/T_h$, where T_h is the length of non-negligible system response. This reduces noise by a factor of $\sqrt{\Delta f_T / \Delta f}$, where $\Delta f_T = 1/T$. In the time domain, this corresponds to a multiplication of the estimated system response, $\hat{h}(t)$, with a window of length T_h or longer. As the smoothing procedure is performed as part of the data processing, the optimal Δf may be determined based on features of the measured data itself, and it may be chosen to vary with frequency. A variable Δf corresponds to letting the length of the system response, T_h, depend on frequency. Thus smoothing $\hat{H}(\omega)$ yields a $\sigma_{\hat{H}}(\omega)$ of:

$$\sigma_{\hat{H}}(\omega) \approx \frac{\sigma_M(\omega)}{A(t_\omega)} \cdot \sqrt{\frac{2\beta}{\pi \Delta f(\omega)}} \quad, \qquad [3.16]$$

where $1/T_h \geq \Delta f(\omega) \geq 1/T$.

The approximation in Eq. [3.10] depends on smoothness of $A(t)$. In a chirp pulse with a rectangular envelope, the smoothness assumption of $A(t)$ is violated at the start and at the end of the pulse. This causes ripples in $I(\omega)$ (Fig. 3.1CD), which to a small degree affect the sensitivity of the measurement over different frequencies, and may

make the measurement more susceptible to timing errors. To avoid these ripples, the sweep may be continued slightly outside of the desired frequency interval, while making a smooth transition of the amplitude to zero. Such an extension of the sweep comes at the cost of slightly increased measurement time only. Optimal amplitude and frequency modulations to minimize ripples and obtain sharp spectral profiles have been investigated elsewhere for slice excitation purposes (62,63).

The case is more complicated when the sweep starts or ends at zero frequency, since negative and positive frequencies cannot be separated on a real-valued system. A chirp starting at zero frequency exhibits a dip in the spectrum at DC, but extending the sweep to negative frequency values could lead to cancellation of certain frequencies and is therefore not generally applicable. At the same time, it is often of particular interest to a have high measurement sensitivity close to DC for an accurate low-frequency system characterization. One way to handle this dilemma is to slow down the sweep suitably at the beginning of the pulse, in order to asymmetrically emphasize low frequencies. Heuristically, a sweep with initial frequency modulation proportional to t^n, where $n>1$, can be well adapted to compensate for the DC dip. It can also be used to boost the low-frequency content of the pulse to achieve particularly high measurement sensitivity at DC (Fig 3.1EF).

Variable sweep speed

The chirps provide a straight-forward way of obtaining broad-band input pulses with an essentially flat energy distribution in the frequency domain for probing a system. The noise in the estimated system response, $\sigma_{\tilde{H}}(\omega)$, will then however only be flat if the noise of the response measurement device is evenly distributed as well. For field measurements based on the derivative of the phase of an NMR signal, as used in this work, the noise is increasing approximately linearly with frequency. One may thus wish to modify the input, such as to achieve a uniform spectral noise distribution in the estimated SIRF/GIRF. This could be done by adjusting the sweep speed of the pulse to yield a non-uniform spectral profile of the input, compensating for the non-uniform noise of the response measurement. In principle, the pulse amplitude

could be chosen non-uniformly as well. However, to not use maximally allowed amplitude throughout the pulse would be an inefficient use of measurement time. Apart from flattening the noise, a sweep of variable speed would also be useful in cases where different sensitivity for different frequency bands of the system characterization is desirable. In the following paragraphs it will be described how to design a frequency-swept pulse to meet specific sensitivity requirements of the system characterization, given a known noise profile of the response measurement setup.

A general frequency- and amplitude-modulated pulse, $c(t)$, can be written as:

$$c(t) = A(t) \cdot \sin\left(\int_0^t y(\tau)\,d\tau\right) , \qquad [3.17]$$

with the instantaneous frequency, ω, being a function of time:

$$\omega = y(t) . \qquad [3.18]$$

If $y(t)$ is either monotonically increasing or decreasing, then there exists an inverse function to $y(t)$, and thereby a unique transform between time and frequency:

$$t = y^{-1}(\omega) . \qquad [3.19]$$

Both amplitude, $A(t)$, and sweep speed, $y'(t)$, can thus be determined as functions of frequency, as well as time. Here this is denoted by the functions $A_\omega(\omega)$ and $y'_\omega(\omega)$, which are the composites of $A(t)$ and $y'(t)$, respectively, with $y^{-1}(\omega)$:

$$\begin{aligned} A_\omega(\omega) &= A(y^{-1}(\omega)) = A(t) \\ y'_\omega(\omega) &= y'(y^{-1}(\omega)) = y'(t) \end{aligned} . \qquad [3.20]$$

If furthermore $y'(t)$ and $A(t)$ are continuous and sufficiently smooth, then the magnitude of the Fourier transform of $c(t)$ is approximately:

$$\left|C(\omega)\right| \approx A_\omega(\omega) \cdot \sqrt{\frac{\pi}{2y'_\omega(\omega)}} , \qquad [3.21]$$

as can be deduced from Ref. (61). Using $c(t)$ as input to determine the system impulse response, the noise in $\hat{H}(\omega)$, after smoothing with a kernel of frequency-dependent width $\Delta f(\omega)$, is (Eq. [3.16]):

$$\sigma_{\hat{H}}(\omega) = \frac{\sigma_M(\omega)}{A_\omega(\omega)} \cdot \sqrt{\frac{2y'_\omega(\omega)}{\pi \Delta f(\omega)}} \quad . \qquad [3.22]$$

If the noise of the measurement method, $\sigma_M(\omega)$, is known, any targeted noise, $\sigma_{\hat{H}t}(\omega)$, in the estimation of $\hat{H}(\omega)$, at any frequency resolution, $\Delta f(\omega)$, can be realized in principle:

$$y'_\omega(\omega) = \left(\frac{\sigma_{\hat{H}t}(\omega) \cdot A_\omega(\omega)}{\sigma_M(\omega)} \right)^2 \cdot \frac{\pi \Delta f(\omega)}{2} \quad . \qquad [3.23]$$

To obtain $y(t)$ from $y'_\omega(\omega)$, the fact that there exists a unique transform between t and ω, can be utilized. As the system is invertible, the following relation holds:

$$\frac{dt}{d\omega} = \frac{1}{d\omega/dt} \quad . \qquad [3.24]$$

Inserting Eqs. [3.19] and [3.20] yields:

$$\frac{dy^{-1}(\omega)}{d\omega} = \frac{1}{y'_\omega(\omega)} \quad . \qquad [3.25]$$

Integrating both sides of the equation gives us the time as function of frequency, $y^{-1}(\omega)$:

$$y^{-1}(\omega) = \int \frac{1}{y'_\omega(\omega)} d\omega \quad . \qquad [3.26]$$

From here, $y(t)$, i.e. the frequency as a function of time, can be obtained by taking the inverse of $y^{-1}(\omega)$. Depending on the form of $y^{-1}(\omega)$, the inverse can be calculated either analytically or numerically. Note that only once $y^{-1}(\omega)$ is known, one also knows the pulse length, T_p, required to achieve the desired frequency resolution and measurement sensitivity. In practice, a reasonable pulse length may be decided upon beforehand, and the calculated $y^{-1}(\omega)$ can then be scaled accordingly, to yield the targeted relative sensitivity profile within a practical measurement time. In this way, pulses can be designed for any specific sensitivity requirements there may be.

If $A_\omega(\omega)$ is non-uniform, the amplitude as a function of time, $A(t)$, is given by the composite of $A_\omega(\omega)$ with $y(t)$. As for the standard

chirp, any discontinuity in *A(t)* violates the approximation of smoothness and gives rise to ripples in the frequency domain. This likewise holds for discontinuities in *y'(t)*, and in both cases the ripples can be suppressed by smoothing the transitions.

3.3 Methods

Shim hardware

Shim system characterization was performed on a whole-body 7T Philips Achieva system (Philips Healthcare, Cleveland, USA), with full 3rd-order spherical harmonic shim coils. The shim system included one actively shielded shim coil for 0th-order field (Z0), and two separate channels producing Z^2 field, one with a shielded (Z2sh) and one with an unshielded shim coil (Z2). The gradient coils, which are also shielded, were used for the 1st-order shim channels. All other shim coils were unshielded. Thus in total 17 shim channels were available (Table 3.2).

The 0th- and higher-order shims were controlled via 16-bit, 25 kS/s digital-to-analog converters (DACs) (National Instruments), connected to the analog control input of the shim amplifiers (Resonance Research Inc., Billerica, USA). All amplifiers for the 0th-, 2nd- and 3rd-order shims were of the same model. The DACs were further connected to a PC and programmed with LabView. For the 1st-order shims, i.e. the gradients, DACs with an output rate of 100 kS/s were used to obtain full control over the wider operational bandwidth of the gradient amplifiers. A custom-built analog voltage summation unit added the shim control from the DACs to the gradient sequence control signal from the spectrometer. The maximum amplitude of the gradients operated via the DACs was limited to 2 mT/m. As the gradients, acting as 1st-order shims, were not controlled via the scanner software, the manufacturer's software pre-emphasis was not included in the characterization.

	Chirp	*Design sweep*
1	A) Choose *BW*, starting frequency (ω_0) and pulse length (T_P) – longer pulse yields better SNR when combined with frequency smoothing B) Set amplitude to maximum allowed (e.g. $A(t)\cdot\omega(t) \leq S_{max}$ & $A(t) \leq G_{max}$) C) Calculate chirp with Eqs. [3.8] & [3.9]	A) Determine measurement noise ($\sigma_M(\omega)$) B) Choose targeted noise ($\sigma_{\hat{H}t}(\omega)$) and frequency resolution ($\Delta f(\omega)$) C) Set amplitude ($A_\omega(\omega)$) to maximum allowed D) Calculate sweep with Eqs. [3.23] & [3.26] and taking the inverse of $y^{-1}(\omega)$
2	*Optionally* smooth amplitude at pulse edges to avoid ripples	
3	*Optionally* slow down sweep close to DC ($\omega(t) \propto t^2$ or t^3)	
4	Measure field response to chosen sweep(s)	
5	Calculate SIRF/GIRF with Eq. [3.5]	
6	Perform frequency domain smoothing of calculated SIRF/GIRF to suitable $\Delta f(\omega)$	

Table 3.1:
Step-by-step guide on how to perform a system characterization based on frequency-swept pulses

Nr	Spherical harmonic	Order	Shim label
0:	1	0	Z0
1:	x		X
2:	y	1	Y
3:	z		Z
4:	xy		XY
5:	yz		ZY
6:	$2z^2 - (x^2 + y^2)$	2	Z2/Z2sh
7:	xz		ZX
8:	$x^2 - y^2$		X2-Y2
9:	$3yx^2 - y^3$		Y3
10:	xyz		XYZ
11:	$5yz^2 - y(x^2 + y^2 + z^2)$		Z2Y
12:	$2z^3 - 3z(x^2 + y^2)$	3	Z3
13:	$5xz^2 - x(x^2 + y^2 + z^2)$		Z2X
14:	$z(x^2 - y^2)$		Z(X2-Y2)
15:	$x^3 - 3xy^2$		X3

Table 3.2: *Real-valued spherical harmonics used as spatial basis functions for the fields measured with the dynamic field camera, also corresponding to the field distributions that the shim coils are designed to produce. For the Z2 field, the shim system included two separate shim coils, one without (Z2) and one with (Z2sh) active self-shielding.*
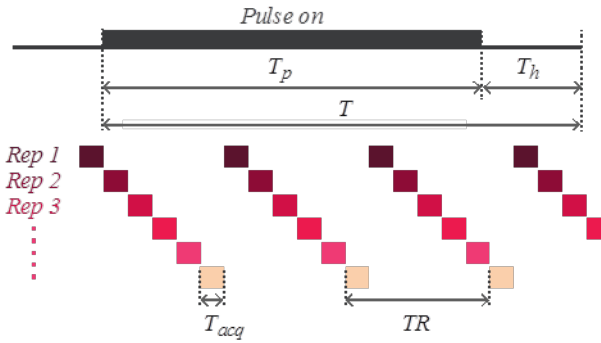
Field measurements

The output shim fields were recorded with spatiotemporal field monitoring (7), using a dynamic field camera (57,35) with 16 NMR field probes (6,38). In the field camera, the probes were distributed as on the surface of a sphere of 20 cm diameter. The unwrapped phase of the probe signal provides a measure of the time-integral of the magnetic field at the position of a probe. The field is thus obtained by taking the time-derivative of the probe phase. For each time point, a set of spatial basis functions can be fitted to the probe data to yield time-varying coefficients connected with static spatial field distributions. Here, real-valued spherical harmonics were used as basis functions, corresponding to the field distributions the shim coils are designed to produce (Table

3.2). 16 probes allow for full 0th - 3rd order fields to be captured simultaneously in one measurement. The probe positions were calibrated by their respective frequency shift under a linear gradient in each direction. In this way, the coordinate system for the probes is defined by the gradient profiles. Signal coupling between the probes was also calibrated under static gradients and corrected for in the processing of the probe data.

The length of each individual field observation, T_{acq}, is limited by the probes' T2*. The field probes used here contained water doped with 17.9mM $GdCl_3$, yielding a T1 and T2 of about 3 ms. As the signal life-time of the probes was much shorter than the desired observation time for the field responses, an interleaved acquisition scheme was applied. The probes were continuously re-excited with a TR dependent on probe T1, thus acquiring snippets of the full field response. The same measurement was then repeated with the acquisitions shifted in relation to the application of the shim pulses, until the full response had been captured (Fig. 3.2). The data from different measurements were stitched together and re-gridded onto a regular time grid using linear interpolation. T_{acq} was set to 1 ms, and the TR of probe re-excitation was 20 ms. Thus 20 separate response measurements were required to acquire the full response. The temporal resolution of the monitored fields is determined by the acquisition dwell time of the spectrometer, and was here set to 18 µs. This gives an acquisition bandwidth of about 56 kHz, which was much larger than the expected response bandwidth of the shim system.

The noise of the phase data from the probes is approximately evenly distributed over the acquisition bandwidth in the frequency domain. However, as the field information is obtained by taking the derivative of the phase, which in the frequency domain corresponds to a multiplication with ω, this causes an amplification of higher frequencies. The measurement noise, $\sigma_M(\omega)$, therefore increases approximately linearly with frequency.

Fig. 3.2: *Schematic of the interleaved response measurements with the dynamic field camera. Each acquisition (T_{acq}) is short in comparison to the length of the total response measurement (T). The probes are re-excited at intervals of TR length, in that way acquiring snippets of the response. The whole measurement is repeated several times with the acquisitions shifted in relation to the shim pulse, to fill in the gaps. Signal acquisition is started slightly before the pulse, and continued slightly longer than T to ensure full coverage of the response.*

System characterization

The input of the system to be characterized was defined as the analytically determined frequency sweeps before digitization and subsequent analog conversion by the DACs. The magnetic field measured by the dynamic field camera in the scanner bore was taken as output. The 17 available shim/gradient channels were considered as different input channels, each yielding 16 separate responses, being the different field terms captured by the field camera. Thus in total, a complete system characterization contained $17 \cdot 16$ measured SIRFs. The response in the field term with the spatial field distribution that the respective shim channel was designed to produce, will hereafter be called self-response. Responses in other spatial field distributions will be termed cross-responses.

For each 0th- and higher-order shim channel the field responses to:

A) a linear frequency sweep according to Eq. [3.9] with $\omega_0 = 0\ Hz$, $BW = 6\ kHz$, $T_p = 10\ s$ and $A = 10\%$ of shim maximum

B) a sweep of variable speed (Eq. [3.17]) between 0 and 15 Hz, with $\omega = \beta t^3$, $\beta \approx 0.094\ rad/s^4$, $T_p = 10\ s$ and

$$A_\omega(\omega) = 0.9e^{-\frac{\omega^2}{2\pi}} + 0.1 \quad \text{(see Eq. [3.20])}$$

were measured. The amplitudes were chosen to adhere to different amplitude restrictions of the shim amplifiers for operation at DC (100%) and for continuous wave operation (10%). The gradients were characterized using the same frequency sweeps, but with a flat amplitude of 1 mT/m for both pulses. T_h was set to 0.26 s, yielding a total response measurement time, T, of 10.26 s. Pulse B was included to obtain particularly high measurement sensitivity and frequency resolution at very low frequencies, in order to accurately capture long-living eddy currents in the SIRFs. The responses of pulses A and B were combined according to Eq. [3.5] to compute the self- and cross-term SIRFs. The resulting SIRFs were smoothed with a kernel of frequency-dependent width, starting at 0.05 Hz at DC and increasing to 10 Hz at 40 Hz, from there on staying constant throughout the higher frequencies.

With the measured SIRFs, the field output to any waveform given as input to the shim system, can be estimated, using Eq. [3.1]. This also holds true for cross-term field responses. Such field estimations were used to validate the measured SIRFs for predictive accuracy. Field responses in all 16 different field terms, to

1) a single trapezoid, with amplitude 10 % of shim maximum, slope 50 ms and length of plateau 0.9 s

2) updating the shim level every 50 ms according to a defined sequence of shim settings

were thus estimated using the measured SIRFs for a set of shim channels. The same sequences were fed as input to those shim channels, and the predicted field outputs were compared to directly measured fields responses both in the self- and cross-terms.

In addition to the shim system characterization based on a broadband linear sweep, we here implemented and tested the approach

where a pulse of variable sweep speed was designed to produce a predefined spectral noise profile in the final SIRF. In order to obtain an estimate of $\sigma_M(\omega)$, the noise of the measurement setup, a set of response measurements were acquired without playing out a pulse on the shim system. The sample standard deviation of the response over intervals of 50 Hz in the frequency domain, scaled by $\sqrt{T}$, was taken as the noise at the respective frequency. $\sigma_{\dot{H}t}(\omega)$ was set to yield a flat noise profile at three different levels depending on frequency, with the smoothed cutoffs at 4 Hz and 2 kHz (Fig. 3.9A). The targeted Δf was set as the width of the variable smoothing kernel used for the standard sweeps, and the pulse amplitude was set to 10% of shim maximum. The required sweep speed, $y'_\omega(\omega)$, was then calculated using Eq. [3.23], thereafter obtaining the final frequency modulation, $y(t)$, from Eq. [3.26] and the inverse of $y^{-1}(\omega)$, to yield a sweep of 9.5 s length. Based on the designed sweep, the SIRF of the X2-Y2 shim channel was measured and compared to the SIRF as measured with a standard chirp. For a fully linear time-invariant system, the two SIRFs should be identical apart from different noise levels. In order to estimate the resulting $\sigma_{\dot{H}}(\omega)$ with the designed sweep, the acquisition snippets of the noise calibration measurement were randomly rearranged in the time domain, to serve as a second instance of a noise measurement. In the frequency domain, this instance of noise was then divided by the designed sweep, and the sample standard deviation over intervals of 50 Hz served as measure of $\sigma_{\dot{H}}(\omega)$.

3.4 Results

The magnitudes of all self-term SIRFs are shown in Fig. 3.3. The SIRFs have been grouped according to order of the spatial field terms. Furthermore, SIRFs for higher-order shim channels with an x-y symmetry have been plotted together to emphasize the striking similarity between them in contrast to otherwise wide differences between SIRFs of different shim channels. All self-term SIRFs from shim channels with unshielded coils have a sharp peak at the center, indicating the presence of long-living eddy currents which act as a narrow low-pass filter. For the shim channels with shielded coils,

including the gradients, this central peak is reduced to <1% of the total response. All self-term SIRFs furthermore contain a distinct set of resonances at frequencies between 200 Hz and 2 kHz. The exact origin of these resonances is unclear. Speculatively however, both mechanical resonances of the scanner and electrical resonances can be suspected. The shim response bandwidth is generally hard to define due to the complicated pattern of resonances, but is around 4-6 kHz at -3 dB for the 0th- and 1st-order shims and 1.5-3 kHz for the 2nd-order shims. For the 3rd-order shims, the long-living eddy currents are strong enough to cause an attenuation of more than 3 dB, and the bandwidth measured in this way would therefore be on the order of 1 Hz.

Both magnitude and phase of the self-term SIRFs for the unshielded and shielded Z2 shim channels are shown in Fig. 3.4. The peak at the center of the SIRF is approximately 0.6 Hz wide and 22% high for Z2, compared to about 1% for the Z2sh (Fig. 3.4BE). The response bandwidth is around 2 kHz at -3 dB for Z2, and around 3 kHz for Z2sh. There is one very distinct resonance of 20-30 Hz width at 1.4 kHz in both shim channels (Fig. 3.4CF), and a widely enhanced response at frequencies between 1-2 kHz.

Looking at the impulse response in the time domain for both Z2 shim channels (Fig. 3.5A), oscillations corresponding to the resonance at 1.4 kHz are clearly visible. The step response neatly demonstrates the effect of the eddy currents in the slow asymptotic approach towards 1 for the Z2 shim channel (Fig. 3.5B), and also here the oscillations right after the step are clearly visible in both shims (Fig. 3.5C). In Fig. 3.5C the effect of eddy currents with short time constants can also be seen for Z2 right after the step.

Cross-term responses are present for all shim channels, both to lower and to higher-order field terms (Fig. 3.6). In general however, higher-order shim channels tend to produce much stronger cross-term fields in the lower orders than vice versa. To compare fields of different spatial orders, the field terms are scaled to the maximum field shift produced within a sphere of 10 cm radius (Hz_{max}). All responses are furthermore normalized to the self-term response at DC of the driving shim channel. A cross-term response of 100% at a particular frequency thus means that the maximum field shift within a 10 cm-sphere due to

the cross-term at this frequency is equal to the field shift produced by the self-term of the driving shim channel in static conditions.

The cross-term response at DC, which corresponds to the static cross-terms, was in most cases very low. For the 0th- and 1st- order shim channels, the cross-terms were typically low over the full bandwidth, maximally reaching up to a few percent (Fig. 3.6AB). For the 2nd- and 3rd-order shim channels it varies between <1% and several hundred percent depending on cross-term (Fig. 3.6CD). Overall, responses of Z2/Z2sh in Z0 and Z2Y/Z3/Z2X in the linear field terms reach the highest values (Fig. 3.6D). Note in Fig. 3.6D showing the Z2Y→Y response that although it is several times higher than the self-response over a wide bandwidth there is a sharp dip in the center, such that the DC response is considerably lower. This is due to strong and long-living eddy currents, producing Y field, that eventually do decay to zero. Also in the cross-terms several resonances are present which differ considerably between the field terms. The resonances seen in the cross-terms generally coincide with those for the associated self-term.

Figure 3.7A shows the slow rise and fall, due to eddy currents, of the Z2Y field at the edges of a trapezoidal input. The cross-response in Y to the same input is up to several times larger than the self-response, but does decay to nearly zero with time (Fig. 3.7B). The SIRF-based prediction of the field response to the trapezoidal pulse shows good accordance with the measured field in both the self- and the cross-term, but with a minimal deviation in the Y-field cross-term.

In Fig. 3.8 the response to updating the shim setting every 50ms is shown for the X2-Y2 shim channel. It can be seen how each shim step is a fraction only of the intended step, due to the eddy currents. How the field actually hits the desired shim level thus strongly depends on the history of the shim settings. Within the 50 ms of each shim setting, the field only slowly and almost negligibly approaches the desired field strength. At the end of each step, field oscillations are seen, as expected due to the resonances in the SIRF (Fig. 3.8B). Again, the SIRF-based field predictions agree well with measured data, and can even accurately capture the field oscillations in the self-term.

Figure 3.9 shows the designed sweep, together with the measured noise and resulting SIRF in X2-Y2. The noise of the field measurement, $\sigma_M(\omega)$, shows a quite flat profile close to DC and

thereafter a nearly linear increase with frequency (Fig. 3.9A). At higher frequencies the noise decreases again due to low-pass filter effects of the receive chain and the signal processing (data not shown). The spectral profile of the input sweep, designed based on $\sigma_M(\omega)$ and a targeted noise profile, $\sigma_{\hat{H}t}(\omega)$, consequently shows the same frequency-dependent increase, as well as a step introduced by $\sigma_{\hat{H}t}(\omega)$ (Fig. 3.9B). The estimation of $\sigma_{\hat{H}}(\omega)$ based on a system response calculation using the rearranged noise measurement well follows the targeted noise profile (Fig. 3.9A). The self-term SIRF for the X2-Y2 shim channel determined with the designed sweep is practically identical to the same SIRF determined with a standard chirp (Fig. 3.9C), with the difference in magnitude being below 1% of the response.
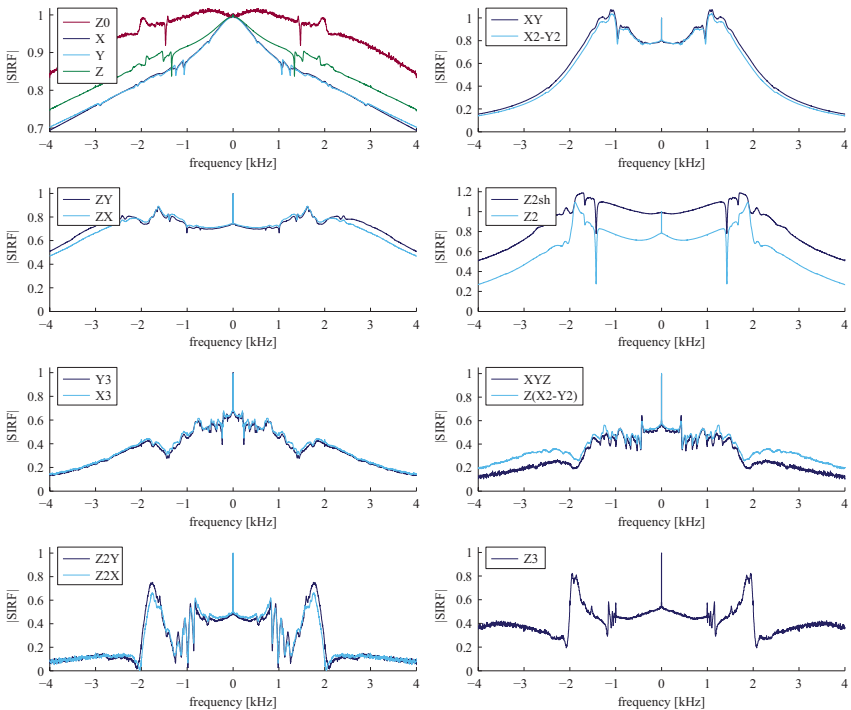
Fig. 3.3: *Magnitude of the self-term SIRF for all shim channels, grouped according to order of field term and x-y symmetry. All SIRFs are scaled to the response at DC. Note that the magnitude scale starts at 0 for all plots except the one containing the 0th- and 1st-order SIRFs. A narrow peak at DC is visible for all unshielded shim channels, indicating the presence of long-living eddy currents. Resonance peaks of possibly mechanical origin can be found in all SIRFs at frequencies between 200 Hz – 2 kHz.*
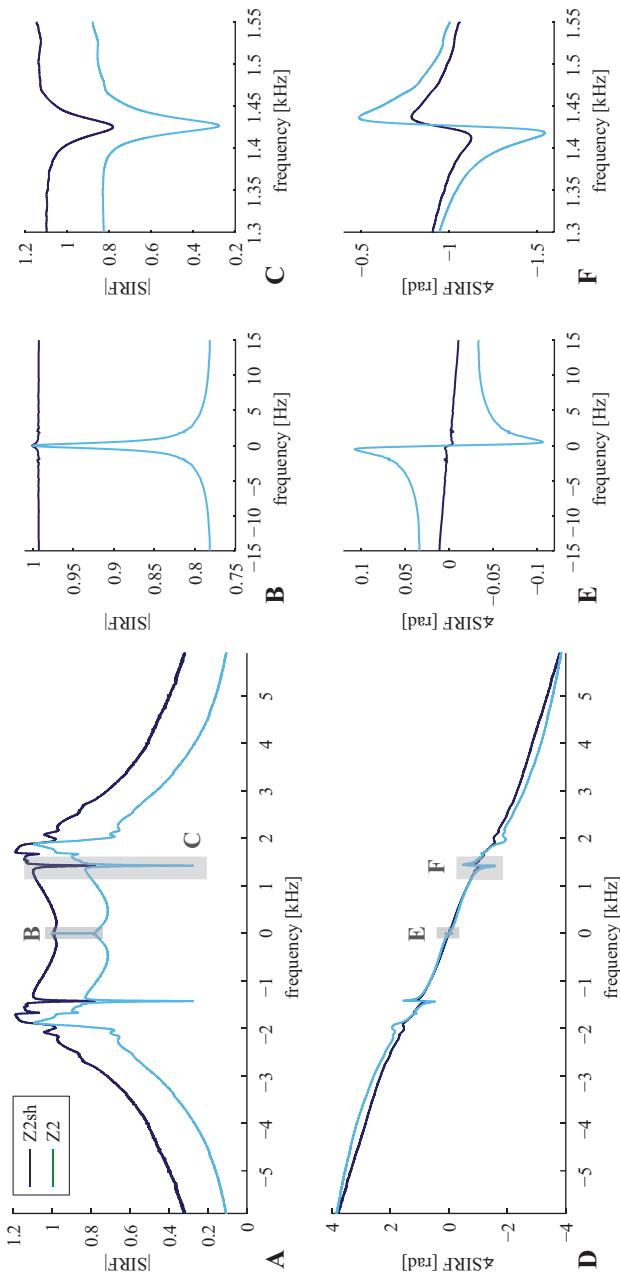
Fig. 3.4: *Self-term SIRF for the unshielded and shielded Z2 shim channels, in magnitude (**A-C**) and phase (**D-F**). Zooms show the central peak caused by eddy currents, which is strongly suppressed for the shielded shim channel (**B,E**), and a deep resonance at 1.4 kHz present in both shim channels (**C,F**).*
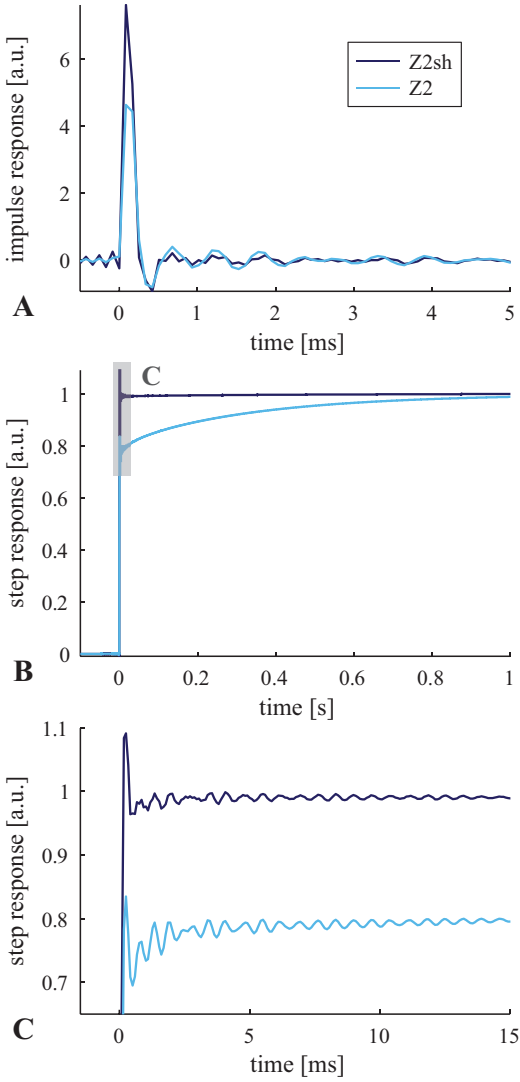
Fig. 3.5: *Time-domain impulse response obtained by a Fourier transform of the measured SIRF (**A**) and step response as yielded by the time-integral of the impulse response (**B,C**) in the self-term for the unshielded and shielded Z2 shim channels. Oscillations right after the impulse/step can be seen (**A,C**), corresponding to the peak at 1.4 kHz in the frequency domain. The long-living eddy currents of the unshielded Z2 can be seen in the slow rise towards 1 in the step response (**B**), and short-living eddy currents are visible in the zoom of the step response (**C**).*

91
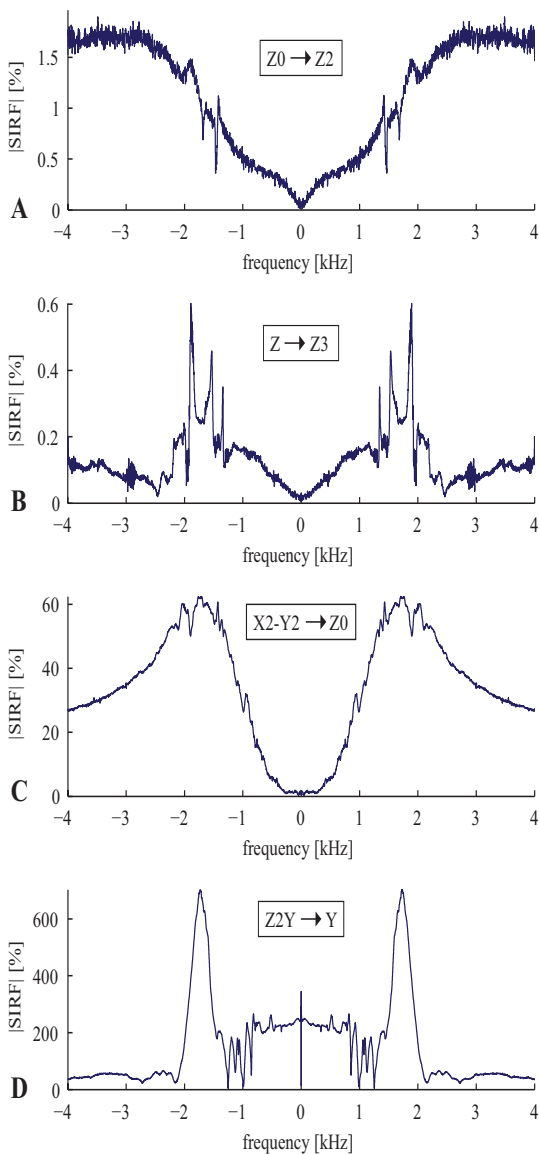
Fig. 3.6: *Magnitude of selected cross-term SIRFs, scaled to DC of the self-term response (in percent). The arrows indicate the direction of the cross-term, e.g. A → B meaning the response in field term B to driving shim channel A. To compare fields of different spatial orders, the field terms as given in Table 2 are rescaled to the maximum field shift within a sphere of 10 cm radius produced by that field term. For cross-terms of higher- to lower-order fields there are several examples of responses ranging far beyond 100% (D). Lower- to higher-order responses are typically below a few percent (A,B). Resonance peaks can be seen in many of the cross-terms (B,D), and long-living eddy currents are present in a few (D).*
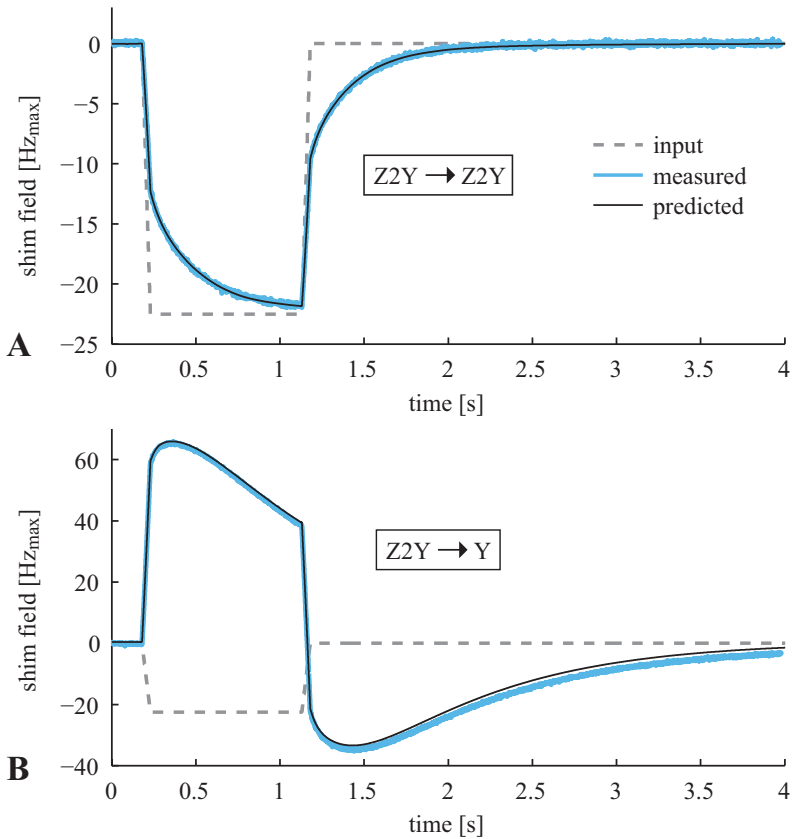
Fig. 3.7: *Comparison of predicted and measured responses to a trapezoidal input in the Z2Y shim channel. The slow rise and fall of the field at the edges of the trapezoid, due to long-living eddy currents, can be well predicted for the self-response (**A**). Also the strong cross-response in the Y field term, and the slow decay towards zero can be predicted with good accuracy (**B**).*
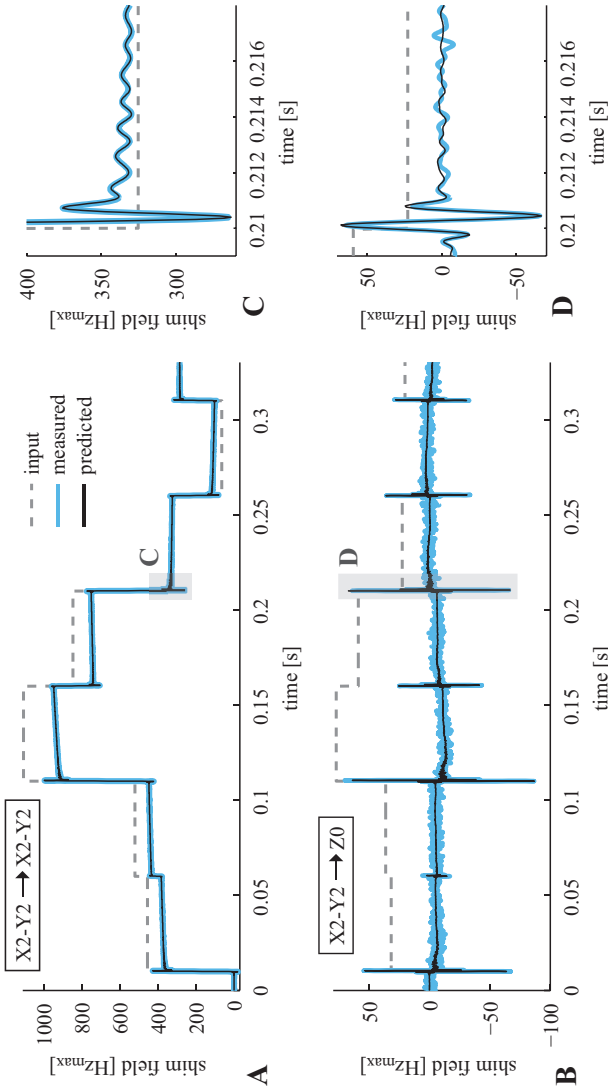
Fig. 3.8: *Comparison of predicted and measured responses to updating the shim setting every 50 ms in the X2-Y2 shim channel. One can note how the shim field, due to eddy currents, only slowly approaches the desired field setting after a step. Therefore, depending on the history of the shim settings, the field will more or less deviate from the desired field (**A**). After each shim step, there is an overshoot followed by oscillations at ~1 kHz in the self-response (**B**). All of these features can be well predicted based on the measured SIRF. In the cross-response to Z0, there is a strong and short oscillation at each step, predicted by the cross-term SIRF (**C,D**).*
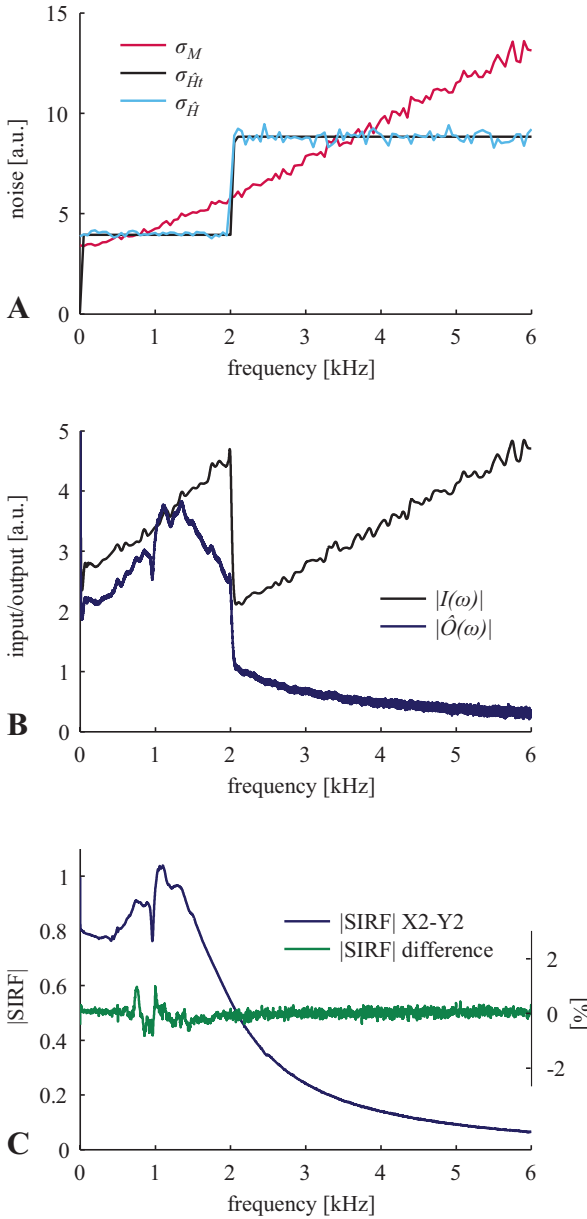
Fig. 3.9: *Comparison of calibrated noise (σ_M), targeted noise profile (σ_Ĥt) and resulting noise in the estimated system response (σ_Ĥ) based on the designed sweep (A). One can see how the profile of σ_H is essentially flat with a step introduced by σ_Ĥt. In (B), the spectral profile of the designed sweep and the measured response are shown. The input increases approximately linearly with frequency to compensate for the frequency-dependent noise increase in σ_M. Note that the fluctuations in the input are due to fluctuations in the calibration of σ_M. The input itself is however still noiseless per definition. The self-term SIRF of the X2-Y2 shim channel determined with the designed sweep agrees well with the same SIRF determined with a standard chirp (C), and the difference in magnitude between the two is <1%.*

95

3.5 Discussion

In this work, the impulse response functions of a higher-order shim system, including the gradients, have been measured by using frequency-swept pulses as test pulses. To this end, properties of frequency sweeps for probing a linear time-invariant system have been investigated. It has been shown theoretically that the noise level in the estimated system response depends on a number of key factors (Eq. [3.16]), namely the noise of the response measurement device ($\sigma_M(\omega)$), amplitude and sweep speed of the test pulse (A and β, resp.), and frequency resolution in the estimated response ($\Delta f(\omega)$). It has also been shown that it is principally possible to design a frequency sweep such as to achieve any desired sensitivity profile of the measurement.

In the literature, a few other classes of input functions for characterizing a linear time-invariant system apart from block pulses and frequency sweeps often appear (59). These include noise-based or pseudorandom sequences and multi-sine pulses. The latter are created by defining the frequency domain magnitude profile of the pulse, usually combined with an iterative optimization of the phase for each frequency, to yield a suitable time-domain pulse. All could be used in principle to characterize a gradient or shim system. The frequency sweeps have the advantage, however, of providing a straight-forward way to keep the time-domain pulse close to, but not exceeding, amplitude and slew rate limits throughout the pulse, while still allowing for a flexible design of the frequency domain profile. This makes for near-optimal time efficiency of the characterization, without the need for iterative optimization algorithms to design the pulse.

For the frequency-swept pulses, a slower sweep speed means spending more time per frequency, and therefore yields higher measurement sensitivity if combined with an appropriate frequency smoothing of the estimated system response. In principle, averaging of several response measurements can also be used to increase sensitivity. The SNR gain per pulse time is equal whether averaging or correspondingly adjusting the sweep speed. Thus acquiring two averages of a sweep yields the same gain in SNR as one sweep of half the speed. However, a waiting time of at least length T_h has to be implemented between each separate input pulse for the averaging,

therefore resulting in a somewhat increased total measurement time for this approach.

Regardless of the types of input, data from response measurements to different test functions can be combined to compute one SIRF, using Eq. [3.5]. In the present work this was performed on data from two frequency sweeps of different bandwidth. It is important to note however, that the combination may be based on any set of inputs – be it different sweeps, block pulses as in Ref. (57), or any arbitrary combination of pulses. Block pulses have an advantage of obtaining particularly high measurement sensitivity around DC, and may well be used as a complement to broadband sweeps.

The frequency resolution of the measured response is $1/T$ without smoothing, where T is the total length of the measurement. Effectively, however, the information on the system response at each frequency has a resolution which depends on the length of the measurement after excitation of that particular frequency. This should ideally, for each frequency, be equal to or longer than the length of the impulse response, T_h, which may vary between frequencies. The response measurements must thus be continued a length of T_h after the end of the sweep, implying that for time efficiency, frequencies expected to have a short response should come at the end of the sweep. Due to the data redundancy of the high frequency resolution in the unprocessed SIRFs, a frequency-domain smoothing may be performed to match the resolution to $1/T_h$ without loss of information on the system response, and thereby yielding a gain in the SNR.

For the noise analyses in the theory section it is assumed that the noise is independent of the input. This holds true for thermal noise of the NMR probes in the field camera. The noise in the phase of the probe signal is flat in the spectrum, and propagates proportionately into all spatial field distributions. As the measure of field is the time-derivative of the phase, the field noise thus increases approximately linearly with frequency. The noise spectrum is also influenced by filters of the receive chain, and noise/jitters of the analog-to-digital converters. The latter can be expected to have a 1/f-dependence and may be the reason for the observed flatness of the field noise close to DC. Additionally, spontaneous field fluctuations inside the scanner bore also appear as noise in the SIRF measurements. Principally, the same analysis applies

for these fluctuations, as long as they are independent of the input. As such fluctuations may be caused by noise from the gradient/shim amplifiers or the cryopump, they may appear disproportionately in specific field terms, and as a consequence, the noise in different field terms may have differing spectral profiles. A sweep designed to achieve specific measurement sensitivity in one field term may thus yield a different noise profile in other field terms.

As the shim field responses could extend over several seconds, the field camera measurements had to be applied in an interleaved and repeated fashion, to fully capture the response. In order to avoid echo formation after re-excitation, the *TR* was in this work chosen quite conservatively to be more than six times T1, and to achieve high phase stability T_{acq} was chosen short compared to T2*, leading to a rather low time efficiency of the measurement. To target higher measurement efficiency, a dedicated setup for continuous field measurements could be used in the future (42). The basis for such a setup is to make the probes short-lived enough that the signal predominantly decays due to T2 relaxation, rather than due to de-phasing from gradient and shim fields, thereby reducing the problem of echo formation (64). Furthermore, by using separate sets of probes that are excited alternatingly, data can be acquired from one set while the other ones are allowed time for relaxation. In this fashion, it becomes feasible to obtain continuous field measurements over several seconds, such that a single application of the input pulse suffices for a full response measurement.

A drawback of the interleaved measurement approach is that any systematic errors of the measurement will appear repeatedly at regular intervals over the length of the response. In the present case, phase errors due to probe coupling and field inhomogeneities of the probes caused single-sample peaks at frequencies corresponding to harmonics of $1/T_{acq}$, and to a lesser degree also $1/TR$. These peaks were generally averaged out by the smoothing process. Where smoothing was not applied, the peaks were removed by interpolating the values of the nearby frequencies. Using probes with shorter relaxation parameters (42,64), these artifacts could be pushed towards higher frequencies and depending on the application may even fall outside of the bandwidth of interest.

The endpoints of the SIRF measurements were in this work defined as the waveform given as input to the DACs and the fields measured in the scanner bore. The measured SIRFs are thus a composite of the transfer functions for the DACs, shim/gradient amplifiers, and the scanner including shim/gradient coils, eddy currents, coil coupling, mechanical vibrations, etc. Exactly how each stage affects the waveform is not given, unless measuring it separately. However, certain features of the SIRFs can be associated with different mechanisms. The amplifiers act as low-pass filters, though with a considerably wider bandwidth than the response bandwidth observed for the higher-order shims. The shim amplifiers were of the same build for the 0th-, 2nd- and 3rd-order shim channels, still the responses differed widely. This indicates that electrical and mechanical properties of the shim coils and surrounding structures determine a major part of the features observed in the SIRFs. Further evidence for this is the similarity observed between the SIRFs of shim channels with an x-y symmetry.

One feature of the SIRFs that can be readily understood is the sharp peak at DC for the unshielded shim coils. This is caused by the unshielded coils coupling strongly to the cryostat, resulting in eddy currents with time constants on the order of seconds. Such eddy currents predominantly have an effect in the field term corresponding to the specific shim channel, however for Z2 they also yield a large Z0 component and similarly for Z2Y/Z3/Z2X they produce strong fields in the linear terms. Less understood are the different resonances below 2 kHz seen in all shims, which may originate in mechanical or electrical resonances of the system. For the gradients, similar peaks have previously been associated with acoustic responses of the scanner (35,11). The mechanical hypothesis is here supported by one resonance at 1.4 kHz appearing in both the Z2 and Z2sh shim channels, despite these channels having markedly different electrical properties.

The utility of the SIRF measurements depends on the linearity and stability of the shim system. Both shim and gradient amplifiers could exhibit certain amplitude-dependent non-linearities, and current/voltage thresholds do limit the domain within which linearity holds. Regarding the stability of the system, preliminary data show that measurements stemming from sessions on different days yield

comparable results. However to quantify the stability, more data would be required.

That the SIRF measurements yield an accurate characterization of system behavior within normal operation is supported by the good agreement between SIRF-based field predictions and directly measured field responses to specific inputs, also in cross-term fields. In some field terms, the predictions were accurate enough to predict small-scale oscillations after steps in the shim settings. In other field terms however, measurement noise and irreproducible field fluctuations together were large enough to overshadow such detailed features of the response. Also, a minimal deviation was seen in the prediction of the Y-field cross-term response to a trapezoidal input in Z2Y, which could be due to either system non-linear or time-variant effects or to measurement errors in the SIRF. These slight deviations notwithstanding, further support for the validity of the characterization technique is given by the stability of the SIRF of the X2-Y2 shim channel, as measured with two markedly different frequency sweeps as inputs.

The ability to measure the GIRFs/SIRFs of a scanner opens up a range of possibilities, in terms of applications. One application that lies near at hand is to determine optimal pre-emphasis settings based on the system characterization. Classically, pre-emphasis has been set with a low number of exponential terms, obtained from a fit of time-domain data after a block pulse (17,46). This mainly yields information on low-frequency behavior of the system. Having a broadband system characterization, however, gives the power to freely shape the system response within hardware bandwidth limitations by applying appropriate filters on the input. Such filters can be calculated from fits of the measured SIRFs, including both exponentially decaying field terms as in the classical case, and oscillatory field terms, which in the frequency domain are seen as resonance peaks off DC (65). Another option is to construct the pre-emphasis filters based on the inverse of the measured SIRFs combined with a suitable low-pass filter (60,66). The latter method provides high degrees of freedom in designing the final system response, but also requires especially high SNR in the SIRF estimate, as noise propagates directly into the applied pre-emphasis filter. Beyond mere pre-emphasis filters, knowing the system response allows for performing a sequence-specific optimization of the input in order to

achieve maximal fidelity of the output gradient or shim waveform within hardware limitations.

Another possibility that becomes feasible with broadband GIRF/SIRF measurements is to use field predictions as a basis for image reconstruction. Thus the actual k-space trajectory, including gradient delays and cross-terms, can be estimated from the input gradient waveforms and can be used in the image reconstruction (67). Similarly, higher-order fields that are present during imaging due to encoding or shimming purposes can be predicted and incorporated in the reconstruction process (39,56,68). Furthermore, as a fast and easy tool to measure system performance the GIRF/SIRF characterization technique may prove useful for system diagnostics and quality control. As seen in this work, the responses, especially for the higher-order shim channels, may show a complicated pattern of resonances and be highly variable between different channels. Using the SIRF characterization to quickly capture the system behavior may help elucidating the origins of such features, and may thereby aid in the development of gradient and shim hardware.

3.6 Conclusion

In this work, frequency-swept pulses as input functions to probe a linear time-invariant system have been investigated, showing that the measurement sensitivity depends on the sweep speed, together with the appropriate frequency smoothing of the estimated system response. The frequency sweeps thus provide a flexible tool that can be adjusted to fit any desired measurement sensitivity, still complying with hardware amplitude and slew rate limitations in the time domain. The characterization method has been applied to the higher-order shim system of an MR scanner, providing a fast and generalized approach for characterizing the dynamics of the shim fields. The SIRF measurements capture a range of features of the shim system, such as response bandwidth, eddy currents, resonances of possibly mechanical origin, and cross-term responses. Knowledge of the SIRFs could form a basis for sequence adjustments for dynamic shimming, corrections in the image reconstruction, and shim pre-emphasis implementations.

Chapter 4

Digital broadband cross-term pre-emphasis for gradients and shims

Manuscript in preparation

4.1 Introduction

Time-varying magnetic fields play a central role in magnetic resonance imaging and spectroscopy as a means to manipulate spin coherences for encoding of spatial information and signal contrast. By far most commonly employed are linear gradient fields, due to which localization by Fourier encoding is made possible (1–3). Less widely spread, but arguably of increasing significance, is encoding and shimming by time-varying fields of higher-order spatial distribution (52,56,69). Common for both is that optimal realization of the MR experiment requires field waveforms in the kHz range, and a very high level of waveform fidelity is of paramount importance to achieve the targeted encoding. Slight deviations from the desired waveforms can have detrimental effects on the MR experiment, leading to artifacts and loss of information in the signal.

The time-varying fields are generated by driving currents through coils designed to produce specific spatial field distributions. The resulting time-courses of the generated fields are influenced by a number of factors, including properties of the coils and amplifiers themselves, but also interactions with other components of the MR scanner. The former naturally impose bandwidth limitations on the field waveforms depending on amplifier frequency response characteristics, in combination with self-inductance and resistance parameters of the coils (45). Regarding interactions, a long-standing issue is eddy currents induced in near-by conducting materials, such as heat shields of the cryostat, giving rise to magnetic fields that tend to oppose the targeted field changes in the magnet bore (9,10,16,17,21,46). Coupling between different field actuation channels can also be a concern, yielding responses of undesired spatial field distributions, called cross-terms. Furthermore, microsecond delays between the field actuation and the signal reception subsystems of an MR scanner can produce phase inconsistencies in the data. Besides pure electrical interactions, also mechanical properties of the MR system can significantly influence the fields, as exemplified by field oscillations resulting from coil vibrations due to changing Lorentz forces on the coils as the currents vary (11,70). Most mechanisms perturbing the field waveforms can affect both the

temporal and the spatial characteristics of the field responses, thus yielding time-varying cross-term responses (9,10,21).

Especially for the gradient hardware, extensive development efforts have been invested in increased switching speed and minimized eddy current induction (45). The pursuit for the latter has led to active shielding of the gradient coils, i.e. for each gradient coil there is an outer current-carrying coil designed to cancel magnetic fields towards the outside (43,44,71,72). Active shielding greatly reduces but does not completely eliminate the impact of eddy currents on the field time-courses (73), and it comes at a cost of bore width. Similarly, field oscillations due to mechanical vibrations are on most MR systems kept low by ensuring balanced Lorentz forces on the coils and providing rigid mechanical support (45). This way, vibrations can be suppressed, but rarely fully eradicated (11,70). Furthermore, also on fast-switching systems, amplifier and coil bandwidth limitations still affect the gradient waveforms. Thus, despite extensive efforts on the hardware side, remaining field imperfections still persist to the degree that they significantly affect MR experiments (12,19,23,74–76).

In order to improve field waveform fidelity, it has long been common practice to modify the control input signal such as to counteract unwanted field effects. Traditionally, this so called pre-emphasis is targeted to suppress eddy-current fields, which are modelled as arising from pure LR-circuits generating exponentially decaying field terms (16,17,46). The input is thus passed through a filter consisting of a sum of exponential terms. The parameters of the exponentials are typically determined by measuring the field response to a step in the gradient demand, and performing a time-domain fit to the measured response. The full complexity of the field perturbations can however not be captured with a model based on a low number of exponentials only. Depending on the design of the system and the set of field channels at hand, oscillatory field components as well as more complicated response patterns and channel interactions can be prominent (57,60,65).

To some extent, deviations in the signal encoding due to field imperfections can, if known, be corrected for by appropriate image reconstruction and post-processing techniques. This however generally requires either a separate calibration acquisition (7,31,77) or specialized equipment for measuring fields concurrently with the MR experiment

(36,38). Furthermore, when field imperfections lead to necessary information being lost from the signal no post-acquisition technique can compensate for the disturbed encoding. This includes cases of distorted excitation patterns (78,79), through-plane dephasing, incomplete k-space sampling (80) and perturbations from a steady state (81).

There is thus a need for a more generalized approach to pre-emphasis. In the present work, we explore two novel pre-emphasis techniques that have the potential to further improve accuracy of actual gradient waveforms and that are geared to addressing issues not accounted for by standard pre-emphasis implementations. Both are based on regarding the gradient and shim chains as linear time-invariant (LTI) systems, for which the gradient or shim impulse response function (GIRF or SIRF) can be determined (57,58,82). The system thus acts as a filter on the prescribed waveforms for each channel.

The basic idea of the first approach is that, having characterized the system, the frequency response can be equalized by employing the inverse of the GIRF or SIRF as pre-emphasis filter. Furthermore, by combining the GIRF inverse with a suitable low-pass function a pre-emphasis filter can be designed that serves to shape the resulting system response to any desired function. The method is valid for controlling the system response over a wide bandwidth, and it does not rely on modelling the physical mechanisms acting on the field waveforms. As an extension, cross-channel pre-emphasis filters can be employed to compensate also for cross-term field responses. This is possible to the degree that field actuation channels exist that produce fields of the same spatial distribution as the cross-term responses.

In a second approach, the input to the system is optimized on a sequence-by-sequence basis, rather than fed through a pre-defined filter. The motivation behind this lies in the nature of the physical limitations of the system. Any real-world system has a limited range of operation, manifested as amplitude and slew rate limitations in the case of the gradients. A frequency-domain filter serving to boost certain frequencies cannot ensure these time-domain limits to be kept for all inputs. Neither will it yield the highest output field fidelity the system could be capable of producing for all inputs. The task of finding the optimal input waveform to achieve a desired field response, still keeping within system limits, is inherently a case-by-case optimization problem. It has

previously been proposed to regard gradient waveform design in general as an optimization problem (83,84). We here demonstrate the first implementation of utilizing the measured system frequency response to improve gradient waveform fidelity for common imaging gradient sequences, based on an optimization approach.

It must be noted that optimal strategies for pre-emphasis, taking cost and effort into account, may vary depending on system properties and intended applications. The aim of this work is not to perform a comparative study between different pre-emphasis methods, but to investigate the feasibility of the presented techniques.

4.2 Theory

The theory presented here is a general treatment of how to compensate for an imperfect system response by modifying the input signal. The outlined principles thus apply for linear gradient channels as well as higher-order gradient or shim channels alike. For simplicity, the term gradient will be used to represent all dynamic field actuation channels whenever general principles are discussed.

It has recently been proposed to model the gradient chain of an MR system as a linear time-invariant system (57,58). More specifically, a multiple-input multiple-output system model is chosen for the model to encompass all gradient channels and field responses. Here, the inputs are defined as the control signals to the different gradient channels, and the outputs are defined as the measured fields of different spatial distribution inside the scanner bore. Such a system can be described in full by a set of transfer functions, here called gradient impulse response functions (GIRFs). Each GIRF thus determines the field response of a particular spatial distribution to input in a particular gradient channel.

In the time domain, the response in the mth output channel, $o_m(t)$, to signal in the lth input channel, $i_l(t)$, can be found as a convolution of the input with the corresponding time-domain impulse response function, $girf_{l,m}(t)$:

$$o_m^{(l)}(t) = \int_{-\infty}^{\infty} i_l(t) \cdot girf_{l,m}(t-\tau)d\tau \; . \qquad [4.1]$$

In the frequency domain this corresponds to a multiplication:

$$O_m^{(l)}(\omega) = I_l(\omega) \cdot GIRF_{l,m}(\omega) \ , \qquad\qquad [4.2]$$

where $O(\omega)$, $I(\omega)$ and $GIRF(\omega)$ represent the Fourier Transform of $i(t)$, $o(t)$ and $girf(t)$ respectively. For simultaneous input in different gradient channels, the resulting response in the mth output channel can be obtained by the sum of the individual contributions from the different inputs. In the frequency domain this yields:

$$O_m(\omega) = \sum_l I_l(\omega) \cdot GIRF_{l,m}(\omega) \qquad\qquad [4.3]$$

The GIRFs of a system can be experimentally determined by driving each gradient channel separately with a controlled input pulse. Given the ability to measure the resulting field responses, the GIRF for each combination of input and output channels can be obtained by a frequency-domain division of the measured output by the known input in the corresponding channels (57). Based on the measured GIRFs, a couple of conceptually different approaches to pre-emphasis can be developed, as will be outlined in the following paragraphs.

Pre-emphasis by GIRF inverse

First, the focus will be on the field response of the spatial distribution that a specific gradient channel was designed to produce. This will be termed the self-term response, and field responses of other spatial distributions will be called cross-term responses. As a specific output channel can be assigned as the self-term for a specific input channel, the subscripts on $O(\omega)$, $I(\omega)$ and $GIRF(\omega)$ are dropped in the following discussion.

One approach to improve the system response is to implement a pre-emphasis filter, $P(\omega)$, acting on the input waveform:

$$O(\omega) = I(\omega) \cdot P(\omega) \cdot GIRF(\omega) \ . \qquad\qquad [4.4]$$

Generally, the pre-emphasis filter aims to equalize the response at all frequencies, such as to yield the targeted output waveform, $O_T(\omega)$, identical to the input:

$$O_T(\omega) = I(\omega) \ . \qquad\qquad [4.5]$$

The simplest formulation of $P(\omega)$ could thus be based on the inverse of the measured GIRF:

$$P(\omega) = \frac{1}{GIRF(\omega)} \; .$$ [4.6]

Such a formulation naturally has its limits where the frequency response of the system gets low, implying that the input has to be amplified nearly infinitely to make up for the inherent attenuation of the system. A more general formulation of $P(\omega)$ is based on defining a desired system transfer function, $H_T(\omega)$, such that:

$$O_T(\omega) = I(\omega) \cdot H_T(\omega) \; ,$$ [4.7]

yielding the pre-emphasis filter:

$$P(\omega) = \frac{H_T(\omega)}{GIRF(\omega)} \; .$$ [4.8]

Generally, the gradient channels as real-world physical systems will act as low-pass filters on the input signal, with a limited bandwidth depending on the coils and the gradient amplifiers. $H_T(\omega)$ must thus be chosen such as to not unduly amplify frequencies above the hardware bandwidth limits. There are several thinkable ways to ensure this. One straightforward and practical approach is to define a $H_T(\omega)$ that goes towards zero faster than the response of the system itself, such that:

$$P(\omega) = \frac{H_T(\omega)}{GIRF(\omega)} < 1, \quad |\omega| > \omega_{BW} \; ,$$ [4.9]

where ω_{BW} defines a cut-off frequency above which the pre-emphasis filter acts as an attenuator on the resulting system response. With this approach, full control in defining the frequency profile of the target system response is retained, however at the cost of narrowing the effectual bandwidth of the system. A related approach, which does not suppress the high-frequency response of the system, is to leave the system response at frequencies above a certain cut-off frequency untouched, or multiplied by a constant, c:

$$P(\omega) = \frac{H_T(\omega)}{GIRF(\omega)} = c, \quad |\omega| > \omega_{BW} \; .$$ [4.10]

This approach may however require extra care to be taken in the design of $H_T(\omega)$ at the transition from the controlled to the uncontrolled

domain, in order to achieve a smooth profile of $H_T(\omega)$. For each of these approaches, a pre-emphasis implementation has been tested in this work, as further described in the Methods.

Determining the pre-emphasis filter based on the inverse of the measured GIRF yields high flexibility in designing the resulting system response. A drawback of the approach however is the sensitivity to noise in the system characterization. The GIRF is determined from actual measurements of the field response to known input pulses. Thus a certain noise component will always be present, which translates into noise in the pre-emphasis filter. In Ref. (82) it is discussed how to choose the input pulses for the system characterization, such as to fulfil certain requirements on the noise level in the final measured GIRF, given known noise characteristics of the field response measurements.

To reduce the propagation of noise into the pre-emphasis, it can be of advantage for less complex system responses to construct the pre-emphasis filter from a low number of analytically defined terms, instead of using the direct non-parametric approach described above. In most cases, an appropriate model will consist of a number of exponentially decaying terms and oscillatory exponentially decaying terms. Modelling the step response, $s(t)$, of the pre-emphasis as a sum of exponentials in the time-domain:

$$s(t) = \theta(t) \sum_j A_j e^{-a_j t} \quad , \qquad [4.11]$$

where $\theta(t)$ is the Heaviside step function, yields a frequency-domain representation of the step response:

$$S(\omega) = \sum_j \frac{A_j}{a_j + i\omega} \quad . \qquad [4.12]$$

As the impulse-response is the time-derivative of the step response, which in the frequency domain corresponds to a multiplication with $i\omega$, this yields the pre-emphasis filter:

$$P(\omega) = \sum_j \frac{A_j i\omega}{a_j + i\omega} \quad . \qquad [4.13]$$

To extract the amplitude parameters, A_j, and the decay times, $1/a_j$, of the appropriate pre-emphasis filter, a fit of the real part of $P(\omega)$:

$$\mathrm{Re}(P(\omega)) = \sum_j \frac{A_j \omega^2}{a_j^2 + \omega^2} \qquad [4.14]$$

on the real part of the inverse of the measured GIRF can be performed. In this representation the exponentials thus correspond to Lorentzian terms. Optionally, the inverse of the GIRF may be multiplied with a target system response before the fit. Oscillatory responses can be described similarly in the frequency domain, but with the center frequency shifted away from DC.

Cross-term pre-emphasis

The method of applying a pre-emphasis filter to the input can be further extended to cover also cross-term responses. Cross-terms of spatial field distributions for which there are available coils can be actively compensated for by creating opposing fields. On many MR systems, the set of active coils are designed to produce approximations of spherical harmonics. The spherical harmonics are simultaneously suitable as basis functions for spatiotemporal field measurements with a limited number of field probes. In this case, the measured field terms can thus straightforwardly be assigned to specific field actuation channels. Alternatively, the fields produced at the probe positions can be determined for each coil, and be used as basis functions for the field measurements.

The system model, including the full set of input and output channels, can in a vector-matrix notation be written as:

$$\begin{pmatrix} O_1(\omega) \\ \vdots \\ O_{N_m}(\omega) \end{pmatrix} = \begin{pmatrix} GIRF_{11}(\omega) & \cdots & GIRF_{1N_l}(\omega) \\ \vdots & \ddots & \vdots \\ GIRF_{N_m 1}(\omega) & \cdots & GIRF_{N_m N_l}(\omega) \end{pmatrix} \begin{pmatrix} I_1(\omega) \\ \vdots \\ I_{N_l}(\omega) \end{pmatrix}, [4.15]$$

where N_l is the number of available input channels and N_m is the number of output field terms. Defining $\bar{I}(\omega)$ and $\bar{O}(\omega)$ as the input and output vectors, respectively, and the system response as a frequency-dependent matrix, **GIRF**(ω), yields:

$$\bar{O}(\omega) = \mathbf{GIRF}(\omega) \cdot \bar{I}(\omega) . \qquad [4.16]$$

Similarly to the case for the self-term pre-emphasis the task is now to find a specific pre-emphasis filter, $P(\omega)$, here a frequency-dependent matrix, to multiply with the input:

$$\overline{O}_T(\omega) = \mathbf{GIRF}(\omega) \cdot \mathbf{P}(\omega) \cdot \overline{I}(\omega) \qquad [4.17]$$

such that the targeted output, $\bar{O}_T(\omega)$, is described by the input passed through a target system response matrix, $\mathbf{H}_T(\omega)$:

$$\overline{O}_T(\omega) = \mathbf{H}_T(\omega) \cdot \overline{I}(\omega) \ . \qquad [4.18]$$

If the number of input channels equals the number of output field terms, this yields $P(\omega)$ as the inverse of the GIRF matrix multiplied with $\mathbf{H}_T(\omega)$:

$$\mathbf{P}(\omega) = \mathbf{GIRF}^{-1}(\omega) \cdot \mathbf{H}_T(\omega) \ . \qquad [4.19]$$

Assuming that the components representing the different input and output channels are arranged such that the self-term GIRFs lie on the diagonals of the GIRF matrix, and the cross-terms make up the off-diagonal elements, a natural choice of $\mathbf{H}_T(\omega)$ is the identity matrix, $\mathbf{Id}$, multiplied with a low-pass filter $H_T(\omega)$:

$$\mathbf{H}_T(\omega) = H_T(\omega) \cdot \mathbf{Id} \ , \qquad [4.20]$$

leading to:

$$\mathbf{P}(\omega) = H_T(\omega) \cdot \mathbf{GIRF}^{-1}(\omega) \ . \qquad [4.21]$$

Note that as the elements of the matrices are frequency-dependent the inversion has to be performed for each frequency at which control of the system frequency response is desired. The elements of the pre-emphasis matrix, $P_{m,l}(\omega)$, represent the pre-emphasized control of the mth shim channel due to input in the lth shim channel. In the above formulation of $\mathbf{H}_T(\omega)$, this amounts to the required cross-term compensation when $m \neq l$. If there is no unique assignment of "self-term" and "cross-term" responses, a more general formulation of $\mathbf{H}_T(\omega)$ can be obtained by setting the lth column of $\mathbf{H}_T(\omega)$ as the targeted output vector to unit input in the lth element of $\bar{I}(\omega)$. This could be the case when a different set of spatial basis functions are used to describe the measured fields than the spatial field distributions that the gradient and shim channels produce. If the number of input and output channels do not match, i.e. $N_m \neq N_l$, the **GIRF** inverse can be replaced by the Moore-Penrose pseudo-inverse:

$$\mathbf{GIRF^+} = \left(\mathbf{GIRF^H GIRF}\right)^{-1} \mathbf{GIRF^H} \ , \qquad [4.22]$$

where H represents the conjugate transpose of the matrix. If $N_l > N_m$, this implies that there is a redundancy in the field actuation channels. The spatial field distribution produced by the redundant field channels can thus be described by a linear combination of the fields from the other channels. In this case, the pseudo-inverse delivers the solution yielding the minimum norm of the input vector after pre-emphasis. If, on the other hand, $N_l < N_m$, there are output field terms which fundamentally cannot be controlled by the input. For such a system, the pre-emphasis calculated with the pseudo-inverse amounts to the solution having the least-squares deviation from the target field vector.

In the choice of low-pass filter, $H_T(\omega)$, the same considerations regarding bandwidth limitation of the system as discussed in the previous section apply in principle. In this case however, it must also be noted that the physical bandwidth limitations may differ between the different gradient channels. Thus it may be desirable to allow for different low-pass filters for different channels. This can be implemented by introducing a diagonal matrix with $H_T(\omega)$ for the different channels as elements on the diagonal. One must be aware of however, that this implies that cross-terms from a channel with a wider bandwidth into one with a narrower bandwidth will not be compensated for at all frequencies. Choosing $H_T(\omega)$ for all channels to be limited by the narrowest bandwidth of the included gradient channels limits the speed of the system unnecessarily for certain channels, but allows for control over the cross-term responses at all frequencies.

As in the case of self-term pre-emphasis based on the GIRF inverse, noise in the measured GIRF propagates to the pre-emphasis filter, here through the inversion of the **GIRF** matrix. Similarly, for less complex system responses a fit of an analytically defined model may be advantageous in order to reduce noise. Here, this amounts to performing a separate fit on each of the frequency-dependent elements of the determined pre-emphasis matrix, $P_{m,l}(\omega)$ separately.

Iterative optimization of input waveforms

The previous sections have treated how to design a pre-emphasis filter such as to achieve a targeted frequency response of the system. It was broadly stated that care must be taken to not excessively amplify frequencies where the natural response of the system is low. A more precise formulation of this limitation can be made by taking a time-domain perspective. For any real-world gradient or shim system there is a limited time-domain amplitude range within which the system behaves approximately linearly and can be safely operated. Limiting factors are, among others, finite available power supply and heat deposition due to the currents. Most gradient systems have time-domain specifications limiting both the amplitude (G_{max}), and the slope of the demand, i.e. the slew rate (S_{max}). Passing the input waveform through a pre-emphasis filter, the effective input, $i_{eff}(t)$, to the system can be written as:

$$i_{eff}(t) = \int_{-\infty}^{\infty} i(\tau) \cdot p(t-\tau)d\tau \ , \qquad [4.23]$$

where $p(t)$ is the time-domain representation of the pre-emphasis. The maximum amplitude and slope of $i_{eff}(t)$ will depend on the original input waveform, $i(t)$, and the pre-emphasis filter. If any frequencies are amplified by the pre-emphasis filter there are necessarily inputs for which $i_{eff}(t)$ exceeds system amplitude or slew rate limits. Furthermore, if the pre-emphasis filter does not bring the resulting system frequency response up to unity at all frequencies, it is not ensured that $i_{eff}(t)$ is the optimal input for maximal fidelity of the output waveform. In effect, any reasonable pre-emphasis filter will neither ensure hardware limits to be kept nor yield optimal output for all input waveforms. To resolve this dilemma, one must move away from the formulation of the pre-emphasis as a pre-defined filter and instead regard it as a sequence-by-sequence optimization problem.

A natural objective function to define for the problem is to minimize the L2-norm of the difference between the system output and a targeted gradient waveform, $g_T(t)$:

$$\min \left\| \int_{-\infty}^{\infty} i(\tau)girf(t-\tau)d\tau - g_T(t) \right\|_2 \qquad [4.24]$$

under the constraints that:

$$i(t) \le G_{max}, \frac{di(t)}{dt} \le S_{max} \quad \forall t \ . \tag{4.25}$$

The objective function can however be adjusted for different goals depending on the application. In the case of spatial encoding by linear gradients for imaging experiments, it can be advantageous to optimize on the integral of the field instead, i.e. on the targeted k-space trajectory, $k_T(t)$:

$$\min \left\| \int_0^t \int_{-\infty}^{\infty} i(\tau) girf(t'-\tau) d\tau dt' - k_T(t) \right\|_2 . \tag{4.26}$$

Furthermore, one may want to weight the field fidelity of different parts of the sequence differently. To this end, a weighting function, $w(t)$, can be introduced:

$$\min \left\| w(t) \left[\int_0^t \int_{-\infty}^{\infty} i(\tau) girf(t'-\tau) d\tau dt' - k_T(t) \right] \right\|_2 . \tag{4.27}$$

The problem formulation could further be extended to include also cross-term responses. One way to do this would be to define the objective function as a sum of the square of the error in the different field terms:

$$\min \sum_m w_m \left\| \sum_l \int_0^t \int_{-\infty}^{\infty} i_l(\tau) girf_{l,m}(t'-\tau) d\tau dt' - k_{T(m)}(t) \right\|_2^2 . \tag{4.28}$$

Here a weighting factor, w_m, was introduced to adjust the relative significance of different field terms in the total error.

Each of these objective functions yields a convex, constrained optimization problem, which can be solved by suitable iterative algorithms. A treatment on the choice of algorithm for efficient solution, given the specific nature of the constraints, can be found in Ref. (85). The listed objective functions are targeted to reduce field deviations due to an imperfect system response given a desired gradient waveform. A more general view of gradient waveform design as an optimization problem is given in Ref. (83).

4.3 Pre-emphasis implementations

To investigate the feasibility of the pre-emphasis approaches outlined in the Theory, test implementations of the different methods have been utilized for gradient or shim pre-emphasis on commercial MR systems. The specific setup details differed between the implementations and will be described in the subsections below. First, a pre-emphasis based on an exponential model, with the goal of reducing field effects of long-living eddy currents of higher-order shims, was implemented. The approach closely resembles the classical pre-emphasis methods, with the difference, however, that the parameters of the exponential field terms were obtained from a frequency-domain fit on the inverse of the measured SIRF (*Frequency-domain fit*) (40). Second, as a more flexible approach, a pre-emphasis filter was calculated from the inverse of the SIRF and a defined targeted system response (*SIRF inverse*) (60). In a third implementation, the pre-emphasis was extended to include also cross-term compensation, and was calculated by inverting the SIRF matrix for a set of shim channels (*Cross-term pre-emphasis*) (66). Finally, an iterative optimization algorithm was utilized to find the optimal gradient input to achieve least k-space deviation for different trajectories commonly used for fast imaging (*Sequence-specific optimization*) (85).

Frequency-domain fit

Methods

Measurements were performed on the higher-order shim system of a whole-body 7T Philips Achieva system (Philips Healthcare, Cleveland, USA) equipped with full 3rd-order spherical harmonic shim coils. The shim amplifiers supported analogue control input, which was realized via a Load&Go (Resonance Research Inc., Billerica, USA) unit for dynamic shim updating. The unit allows for updating the shim settings for each channel in a pre-defined sequence. Sequence definition was performed on a PC connected to the Load&Go unit. Synchronization with the scanner sequence timing was achieved via a trigger signal from the spectrometer.

Field measurements were performed with a 3rd-order dynamic field camera comprising 16 ^{1}H NMR field probes distributed as on the surface of a sphere of 20 cm diameter (6,7,38). The probes were doped to yield a T1 and T2 of approximately 20 ms. In order to measure field responses that extended longer than the signal life-time of the probes, an interleaved measurement scheme was implemented (82). Each experiment was thus repeated a number of times with the field acquisitions shifted in relation to the shim control signal, until the full field response to a certain shim waveform had been acquired. Here, each acquisition after probe excitation covered 20 ms (T_{acq}), and the probes were re-excited at a rate of 300 ms (TR), thus requiring 15 repetitions for full coverage of the shim field response. In the frequency-domain representation of the field measurements, narrow peaks at the concatenation frequencies ($1/TR$, $1/T_{acq}$ and harmonics thereof) could be observed and were removed by interpolation of nearby values.

In order to determine the SIRFs of the system, two separate sets of boxcar functions were fed as input to the shim channels. One set of boxcar inputs (width 0.1, 0.3 and 0.5 ms, amplitude 10 % of shim maximum) were intended to measure the GIRFs over a wider bandwidth, with low frequency resolution (40 Hz), and the second set (width 0.3, 0.5, 0.9 and 1.5 s, amplitude 30 % of shim maximum) served to measure very low frequencies with high sensitivity and frequency resolution (0.15 Hz). From the responses to each set of boxcars, the GIRF was calculated as a least-squares combination of the individual measurements (57).

A pre-emphasis model of three exponential terms was fitted in the frequency-domain to the real part of the GIRF inverse, using a Levenberg-Marquardt algorithm provided in Matlab (Matlab 2010a, Mathworks, USA). The fit was restricted to cover only frequencies below 20 Hz. Application of the exponential pre-emphasis was performed with analogue electrical circuits contained within the Load&Go unit for this purpose, using the decay times and amplitude parameters obtained from the fit. The resulting system response with pre-emphasis was measured with two sets of boxcar inputs, as described above.

Results

Figure 4.1A shows the magnitude of the inverse SIRF and the fitted pre-emphasis filter for the X2-Y2 shim channel. The low-frequency response could be well approximated by three Lorentzian terms, with a fit residual of <0.2%. The fit yielded exponential decay times of 584 ms, 252 ms and 52 ms with relative amplitudes of 8.9 %, 11.1% and 4.6%, respectively. The measured SIRF with pre-emphasis for the same shim channel showed a mostly flat magnitude response around DC (±0.4% deviation from 1 within ±20 Hz) (Fig. 4.1B), and an approximately linear phase response (Fig. 4.1D). At higher frequencies the pre-emphasis acts as a constant amplification of the system response, as can be expected from the frequency-domain representation of the exponential field terms (Fig. 4.1C).
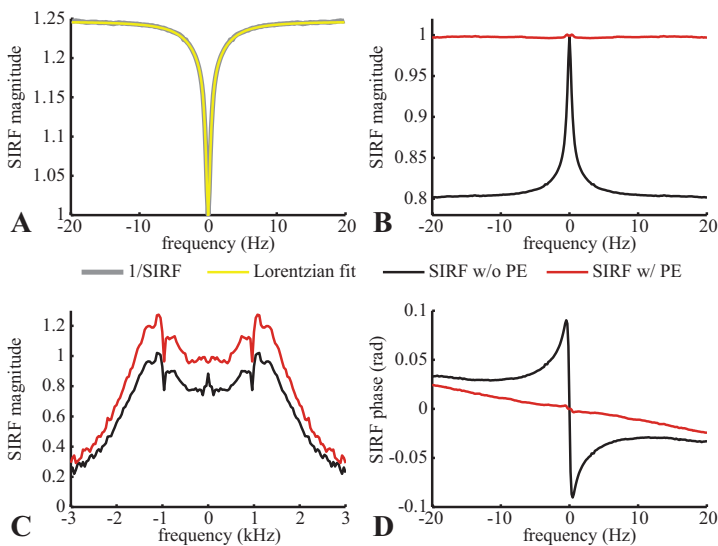
Fig. 4.1: *The magnitude of the SIRF inverse together with the fitted Lorentzian terms are shown in (**A**). Magnitude and phase (**B** and **D**, resp.) of measured SIRFs with and without pre-emphasis (PE) are plotted for the low-frequency response. The magnitude of a broadband SIRF with and without pre-emphasis is shown in (**C**). All shown SIRFs are self-term responses of the X2-Y2 shim channel.*

SIRF inverse

Methods

Measurements were performed on the higher-order shim system of the 7T scanner mentioned in the previous section. Shim control was in this setup realized via a set of digital-to-analogue converters (DAC) (NI 9264 set in an NI cDAQ 9188 chassis, National Instruments), connected to the analogue input of the shim amplifiers. The DACs (sample rate 25 kS/s, range +/- 10V, dynamic range 16 bits) were programmed with LabView and controlled via a PC. The output waveforms were synchronized with the scanner sequence timing via a trigger signal, and the clock of the DACs was locked to the clock of the spectrometer to avoid slow relative drifts for long shim pulses.

Field measurements were performed with a 3rd-order dynamic field camera based on ^{1}H probes doped to a T1 and T2 of 3 ms. Shim field responses were acquired in an interleaved measurement scheme with 3 ms acquisition time and 30 ms probe TR, thus requiring 10 repetitions of the experiment for full measurement coverage of the field response. Peaks at the concatenation frequencies were removed by interpolation in the frequency domain.

Characterization of the shim system response was performed with two frequency-swept pulses as inputs, one covering the full bandwidth of interest and the other aimed to capture the low-frequency response with high sensitivity at a high frequency resolution. The former was a linear frequency sweep of amplitude 10% of shim maximum, covering 0-2 kHz played out in 1 second, and the latter was a linear frequency sweep of amplitude 10% of shim maximum, starting and ending at 4% (i.e. initial phase pi/8), covering 0-20 Hz played out in 6 seconds. The SIRF was calculated from a least-squares combination of the two measurements.

For the pre-emphasis design, a target system response, $H_T(\omega)$, was defined such as to achieve unit response with a linear phase within a specified bandwidth, and to leave the response untouched at higher frequencies:

$$H_T(\omega) = GIRF(1 - rc(\omega)) + rc(\omega)e^{i\omega\tau} \qquad [4.29]$$

where $rc(\omega)$ is a raised-cosine low-pass filter:

$$rc(\omega) =$$

$$
\begin{cases}
1, & |\omega| < \omega_C(1-\beta) \\
\dfrac{1}{2} + \dfrac{1}{2}\cos\left(\dfrac{\pi\left(|\omega| - \omega_C(1-\beta)\right)}{2\omega_C\beta}\right), & \omega_C(1-\beta) < |\omega| < \omega_C(1+\beta) \\
0, & |\omega| > \omega_C(1+\beta)
\end{cases}
\qquad [4.30]
$$

The full-width half-maximum of the filter is determined by ω_c and β is a factor defining the width of the transition band. Here ω_c was set to 1.4 kHz and β was set to 1/4 yielding a transition width of 0.7 kHz. This yields the pre-emphasis filter:

$$P(\omega) = 1 - rc(\omega) + \frac{rc(\omega) \cdot e^{i\omega\tau}}{GIRF(\omega)} \ . \qquad [4.31]$$

τ was chosen such as to smoothly join the phase of $H_T(\omega)$ with the original phase response of the system. The latter was obtained from a linear fit of the phase of the measured GIRF up to 1.9 kHz. The linear phase in the targeted system response corresponds to a group delay of τ. If the shim demand is known sufficiently long before actuation, a negative delay of τ could be introduced to compensate for this linear phase.

   The system response with pre-emphasis was measured with a linear frequency sweep of 10% shim maximum, covering 0-4 kHz, played out in 4 seconds. The low-frequency response (<5 Hz) was obtained from measurements of a trapezoidal pulse of 1 second length and 10 ms slope. The same trapezoidal pulse was measured also without pre-emphasis for comparison. The measured GIRFs with and without pre-emphasis were furthermore used to predict the field response to a trapezoidal pulse of 1 s length and 0.6 ms slope.

Results

The pre-emphasis filter calculated from the SIRF inverse is displayed for the X2-Y2 shim channel in Fig. 4.2A. The magnitude profile
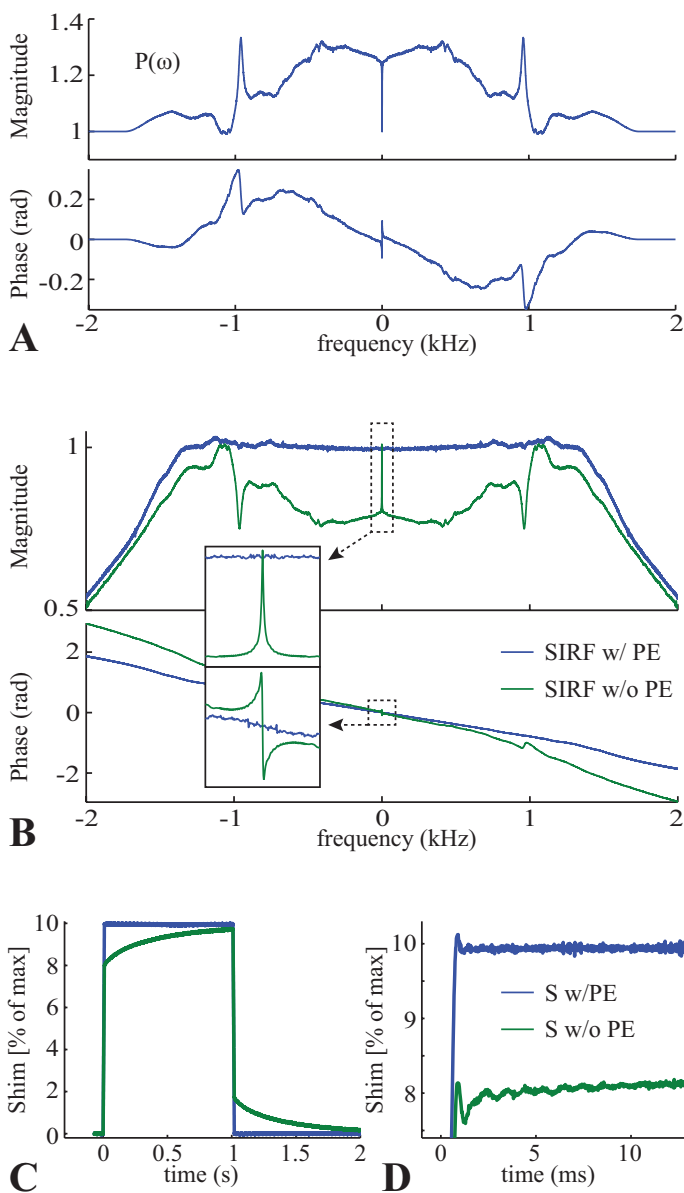
Fig. 4.2: *Pre-emphasis filter calculated from inverse SIRF (A) and measured SIRFs with and without pre-emphasis (PE) (B). Measured and predicted (C and D, resp.) shim responses (S) to a trapezoidal input with and without pre-emphasis. The responses are scaled to % of maximum shim field. All data shown are from the X2-Y2 shim channel.*

shows that frequencies above 1 Hz are strongly amplified to compensate for long-living eddy currents. A prominent peak in the filter at around 1 kHz can also be noticed, serving to equalize a resonance in the original SIRF. Viewing the full shape of the filter, it becomes apparent that a rational approximation of the filter would require a model of high order to capture all features. Figure 4.2B shows the measured SIRF with and without pre-emphasis. With pre-emphasis a nearly flat plateau is created in the magnitude response up to the cut-off bandwidth of the pre-emphasis filter. In the phase response the pre-emphasis delivers a mostly linear phase as targeted, with a τ of about 0.2 ms. Figure 4.2C and 4.2D show the measured and predicted field responses, respectively, to trapezoidal inputs with and without pre-emphasis. Without pre-emphasis, the field rises slowly due to the long-living eddy currents, whereas with pre-emphasis the targeted field value can be reached within milliseconds.

Cross-term pre-emphasis

Methods

Measurements were performed on the higher-order shim system of the same 7T scanner as above, using the shim control setup described in the previous section. Additionally, in order to control the linear gradient channels of the system, a custom-built voltage summation unit was used to add output from the DACs to the gradient control voltage of the system spectrometer for each gradient channel. For linear gradient control, DACs with a higher sample rate (100 kS/s, range +/- 10 V, dynamic range 16 bits, NI 9263) than for control of the higher-order shims were employed in order to cover the full operational bandwidth of the linear gradient amplifiers.

Field measurements were performed with a 3rd-order dynamic field camera, containing proton probes with a T1 and T2 of 3 ms. Interleaved measurements were acquired with a probe TR of 20 ms and a T_{acq} of 1 ms, thus requiring 20 measurement repetitions for full response coverage. Narrow peaks at the concatenation frequencies were removed as above.

Shim characterization was performed with two frequency-swept pulses. The first was a linear frequency sweep covering 0-2 kHz in 10

seconds, with an amplitude of 10% of maximum for higher-order shim channels and 1 mT/m for gradient channels. The second sweep had a frequency modulation increasing cubically with time, covering 0-15 Hz in 10 seconds. The amplitude was frequency-dependent ranging between 10-100% of shim maximum for higher-order shims, and flat 1 mT/m for gradients (82). The resulting SIRF was smoothed in the frequency domain with a kernel of frequency-dependent width, varying between <0.1Hz for the lowest frequencies to 10 Hz for frequencies above 40 Hz.

The cross-term pre-emphasis for interactions between the Z2Y and the Y channels was determined. These specific channels were chosen for the very strong cross-term responses observed in the Y field term to input in the Z2Y shim channel. The targeted self-term response was chosen to be a raised-cosine low-pass filter with ω_c and β set to 0.5 kHz and 1, respectively (see Eq. [4.30]). The pre-emphasis matrix was thus defined as:

$$\mathbf{P}(\omega) = rc(\omega) \cdot \mathbf{SIRF}^{-1}(\omega) \ . \qquad [4.32]$$

The resulting system response with cross-term pre-emphasis was determined for input in the Z2Y shim channel using a linear frequency sweep covering 0-1.2 kHz in 8 seconds at 10% of shim maximum. Furthermore, the field response to a trapezoidal input (5 ms slope, 0.5 s plateau) was measured with and without pre-emphasis.

Results

Measured SIRFs with and without cross-term pre-emphasis are shown together with the targeted system response and the implemented pre-emphasis filters for the Z2Y and Y shim channels in Figures 4.3 and 4.4, respectively. All SIRFs shown are responses to input in the Z2Y shim channel. In order to compare responses of different spatial order, all field terms are scaled to maximum field shift within a sphere of 10 cm radius and the SIRF magnitude plots are further scaled to the response at DC of the Z2Y self-term.

The Z2Y self-response is suppressed by eddy currents, and several strong resonances can be observed (Fig. 4.3AB). The Y cross-term at most exceeds 3 at frequencies above 1 Hz (Fig. 4.4AB), indicating that the maximum field caused by a linear field term in the y direction at these frequencies is 3 times higher than the static response in
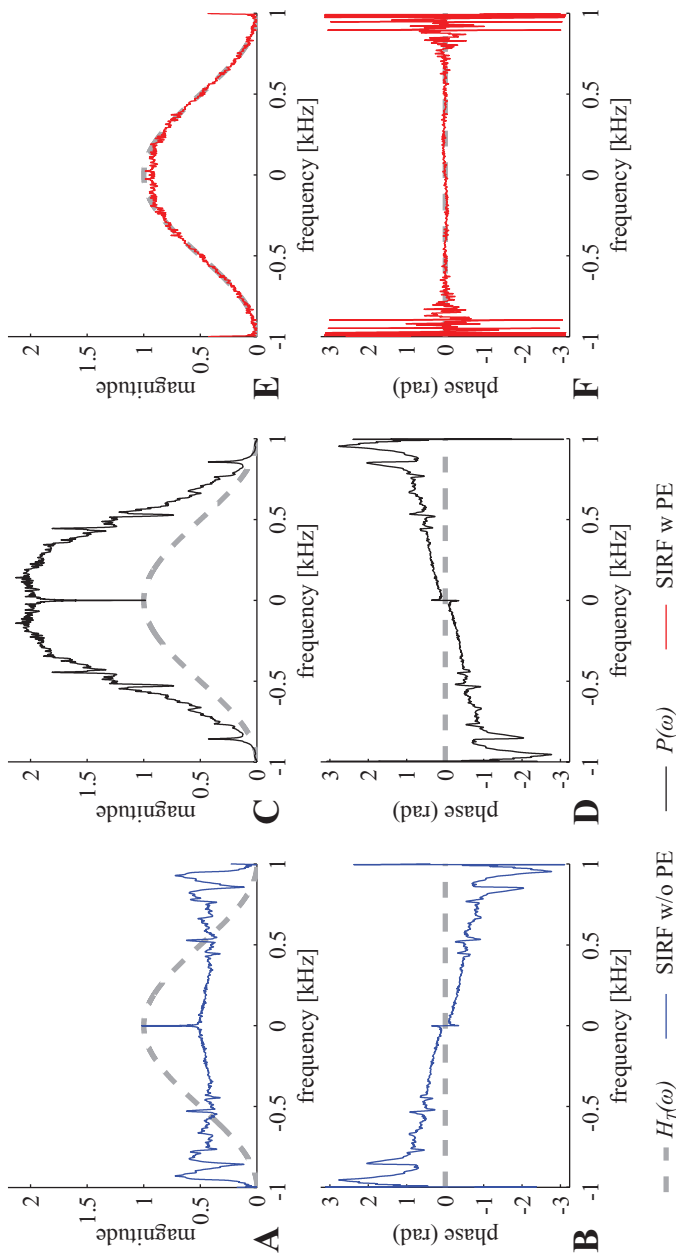
Fig. 4.3: *Measured self-term SIRF without pre-emphasis (PE) of the Z2Y shim channel (**AB**), calculated pre-emphasis filter (P(ω)) (**CD**) and measured self-term SIRF with pre-emphasis (**EF**). All plots contain the targeted frequency response, $H_T(ω)$. The magnitude plots are normalized to the DC response of the self-term SIRF.*
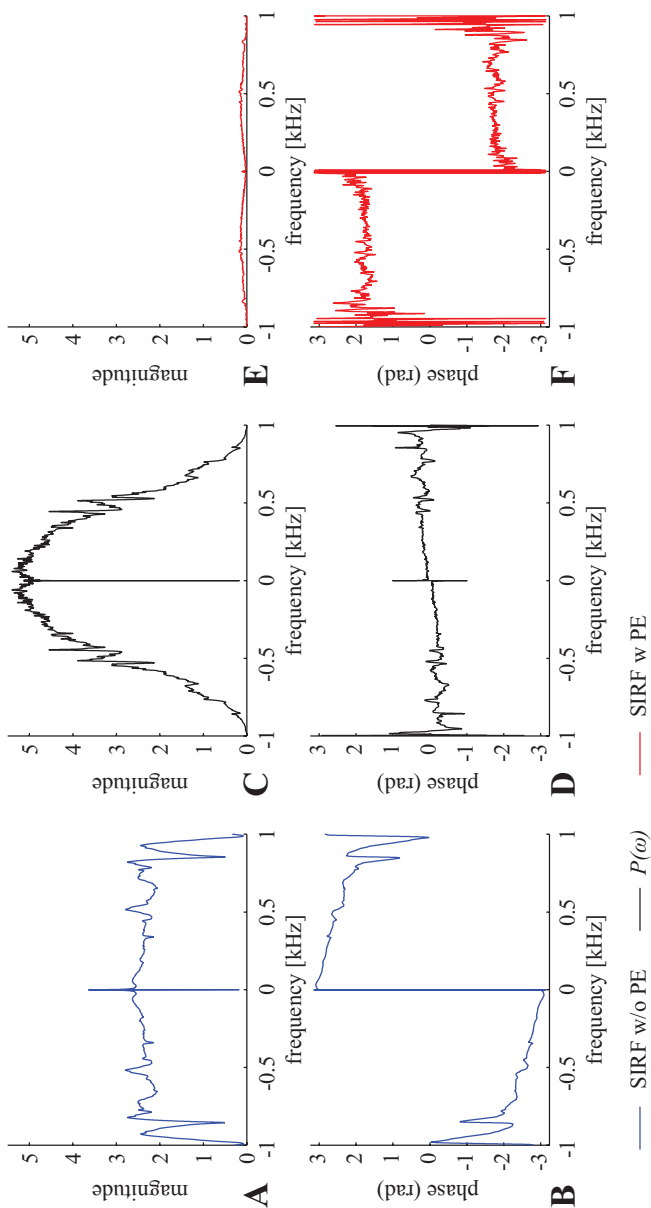
Fig. 4.4: *Measured cross-term SIRF without pre-emphasis (PE) for Y field response to input in the Z2Y shim channel (**AB**), calculated cross-term pre-emphasis filter (P(ω)) (**CD**) and measured cross-term SIRF with pre-emphasis (**EF**). The targeted frequency response is naturally zero in this case. The magnitude plots are normalized to the DC response of the self-term SIRF.*

the Z2Y field term. Figures 4.3CD and 4.4CD show the calculated pre-emphasis filters required to achieve the targeted system response in the Z2Y self-term and the Y cross-term, respectively. Implementing these pre-emphasis filters yields a self-term response that closely follows the targeted response, however with some slight deviation at low frequencies (Fig. 4.3EF). Resonances appearing around x Hz in the self-term response without pre-emphasis are suppressed beneath noise level with pre-emphasis. The cross-term response in Y is efficiently suppressed by the pre-emphasis, and the remaining cross-term component maximally reaches 6 % of the original cross-term response (Fig. 4.4EF).

Figure 4.5A and 4.5B show the time-domain responses in the Z2Y and Y field terms, respectively, to a trapezoidal input in the Z2Y shim channel, with and without pre-emphasis. With pre-emphasis the peak input in the self-term is nearly doubled as compared to without pre-emphasis, and the field response therefore quickly reaches the targeted value (Fig. 4.5A). The cross-term response without pre-emphasis at times exceeds 300% of the amplitude of the self-term response. (Fig. 4.5B) When compensated for by the pre-emphasis, the cross-term response maximally reaches 3% of the self-term response.
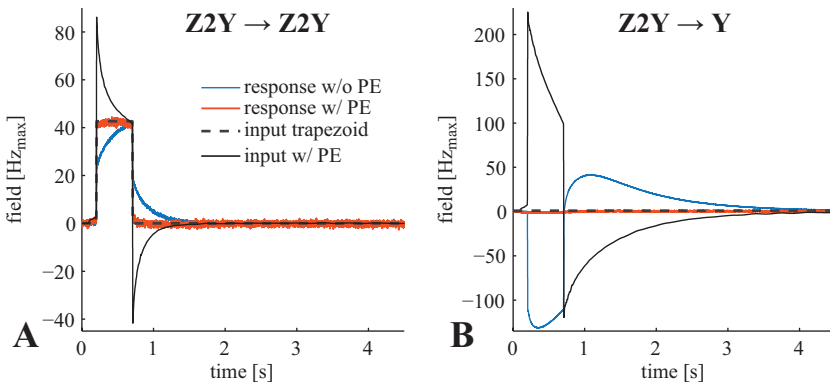
*Fig. 4.5: Measured field response to a trapezoidal input in the Z2Y shim channel with and without cross-term pre-emphasis (PE). The response is shown in the self-term (**A**) and the Y-field cross-term (**B**). Measured fields are scaled to maximum field shift within a sphere of 10 cm radius*

Sequence-specific optimization

Methods

Pre-emphasis by iterative optimization of the input was tested on the gradient system of a 3T Philips Achieva scanner (Philips Healthcare, Best, The Netherlands). Gradient sequence definitions were processed with the ordinary scanner control software, including eddy current compensation and gradient delay correction as implemented by the manufacturer.

Field measurements for system characterization were obtained with a 3rd-order dynamic field camera, based on NMR field probes containing water doped such as to allow continuous field observations up to 100 ms. The gradient system was probed with a set of triangular pulses as inputs as described in Ref. (57). In order to reduce noise in the representation of the system response used for the optimization, a rational transfer function was fitted to the measured GIRF in a semi-automatic fitting procedure. A sampled time-domain representation of the fitted transfer function was used in the optimization described below. Details on the chosen transfer function model and the fit procedure are given in Ref. (85).

Input waveform optimization was performed for EPI and spiral k-space trajectories, defined to yield 3 mm resolution at a field-of-view of 220 mm. Gradient sequences with which the defined trajectories could be traversed were calculated with the time-optimal method described in Ref. (86). For each trajectory, a set of gradient sequences were calculated using different values for the maximum gradient and slew rate limits, ranging between 80% and 100% of the specifications for the gradient system used (G_{max} 31 mT/m, S_{max} 200 T/M/s). Gradient sequences calculated with reduced hardware limits thus needed longer time to traverse a specific trajectory.

The trajectories were chosen to lie in the transversal plane and the input optimization was performed separately for the two gradient axes. The objective function for the optimization was defined as the root-sum-of-squares error of the time-integral of the gradient waveform (Eq. [4.26]), i.e. the error in k(t) for each axis, sampled at a rate of 6.4 µs. The full hardware limits of the system were used as constraints for the optimization algorithm. Reference sequences based on reduced

hardware limits thus contained more leeway for the optimization to shape the input such as to reach higher output field fidelity. The optimization was implemented as an active set algorithm programmed in C, described in Ref. (85). Selected gradient waveforms were given as input, with and without optimization, to the gradient system. The resulting field responses were measured with a dynamic field camera as above, and the measured trajectories were compared to the targeted trajectories.

Results

Figure 4.6A and 4.6B show a zoom of one corner of the targeted EPI trajectory, including prephaser, together with the measured results of the optimized and the non-optimized inputs for gradient sequences calculated based on 100% gradient amplitude and slew rate limitations (Fig. 4.6A) and based on 80% of the limitations (Fig. 4.6B). The measured trajectories show especially large deviations from the target trajectory at the turns of the trajectory, due to the slightly attenuated system frequency response at the main frequencies of the EPI readout gradient. For the non-optimized gradient sequences, reducing the hardware limits does not considerably improve the deviation at the turns. The gradient sequence based on full hardware constraints operates at the system limits at nearly all times, and consequently only moderate improvements due to the optimization can be observed. For the gradient sequence based on reduced limits, however, the optimized input achieves significantly reduced deviation from the target trajectory. The length of the gradient sequences based on 100% and 80% of system limits was 31 ms and 36 ms respectively. Simulations show that already at a reduction of the gradient amplitude to 90% a comparable trajectory improvement could be achieved at only 1 ms increased length of the sequence.

       The results of optimizing the input for an Archimedean center-out spiral trajectory are shown in Figure 4.6C and 4.6D, basing the gradient sequence on 100% and 80%, respectively, of the hardware limits. Most of the deviation between measured and targeted trajectories happens at the center of the spiral, which is therefore shown in the plot. The deviation at the center is due to the sequence operating at higher
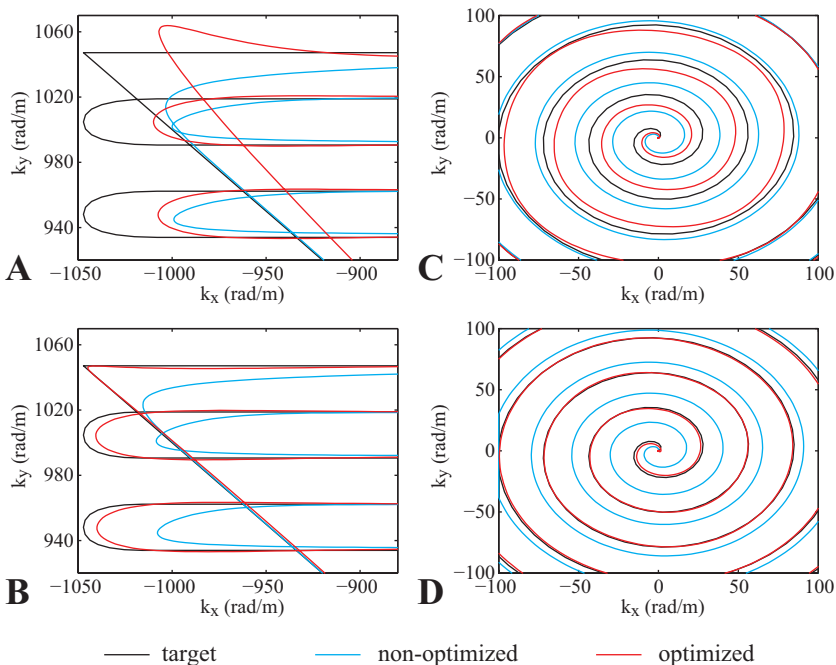
Fig. 4.6: *Zoom of targeted EPI trajectory together with measured optimized and non-optimized trajectories for gradient sequences calculated based on 100% (**A**) and 80% (**B**) of system hardware constraints. Zoom of targeted spiral trajectory together with measured optimized and non-optimized trajectories without and with (**C** and **D**, resp.) reduced slew rate and gradient constraints.*

frequencies at the start, and consequently being more affected by the low-pass characteristics of the gradient system. For the gradient sequence based on full hardware limits, both the optimized and the non-optimized input yield trajectories that seemingly do approach the target after a few spiral turns. It is worth noting, however, that the non-optimized trajectory has by the time it closes up on the target trajectory been through one turn more, and therefore in reality deviates by one Δk. This deviation persists to the end of the trajectory, leading to a slightly diminished k-space coverage of the non-optimized trajectory. The

optimized trajectory is also affected by the frequency compression at the center of the trajectory, but catches up with and closely follows the target trajectory after a few turns. For the gradient sequence calculated based on reduced hardware limits, the optimized trajectory shows only very minor deviations from the target trajectory throughout the whole sequence. The length of the gradient sequences based on 100% and 80% of gradient amplitude and slew rate limits was 21.8 ms and 24.4 ms respectively. Simulations show that the slew rate reduction has the larger effect on improving the trajectory by optimization, but also is the primary factor prolonging the sequence.

4.4 Discussion and Conclusion

Field fidelity is a crucial requirement for many applications in MR imaging and spectroscopy. Despite increasing sophistication of the gradient and shim hardware, remaining dynamic field imperfections can cause significant artifacts in sensitive applications. Traditionally, exponentially decaying fields caused by eddy current induction have been counteracted by applying a pre-emphasis filter to the input waveforms. The complexity of the field dynamics can however not be fully accounted for with this model. The present work has focused on novel approaches to pre-emphasis based on a broadband characterization of the frequency response of the system. The presented methods come in different flavors, which may be suitable for different systems depending on properties of the system response, the quality of the available system characterization and the requirements of the intended applications.

In a parametrical approach closely related to the classical version of pre-emphasis, an analytically defined model can be fitted to the inverse of the measured GIRF. In this work, eddy current fields were compensated for on a higher-order shim system by fitting three Lorentzian terms to the low-frequency components of the SIRF inverse. As such, the method thus mainly differs from classical pre-emphasis implementations by taking a frequency-domain perspective. The model can however readily be extended to encompass also other types of responses, such as oscillatory field terms, which in the frequency domain are represented by resonances not centered at DC (65). For

complicated system responses, however, it may be difficult to robustly obtain good fits, and the procedure will generally require manual interaction to choose appropriate starting points for the fitting algorithms.

A more general approach to pre-emphasis is to equalize the frequency response of the system by directly utilizing the inverse of the measured GIRF multiplied with a low-pass filter of choice as the pre-emphasis filter. This yields full control in shaping the system response within hardware bandwidth limitations. Crucial for this approach, however, is to possess a low-noise estimate of the system response, as any noise in the measured GIRF directly translates into noise in the pre-emphasis filter. A detailed discussion on how to achieve a GIRF measurement with a targeted noise level can be found in Ref. (82). It was here shown that a highly complex frequency response could be flattened within a specified bandwidth using this approach on higher-order shim channels.

The pre-emphasis based on the GIRF inverse was further extended to address also cross-term responses, which on some systems can be detrimental for specific applications. The cross-term compensation relies on having field actuation channels corresponding to the induced cross-terms, such as to be able to actively drive counteracting fields. Cross-term pre-emphasis was calculated using a matrix-vector representation of the system. As for the self-term pre-emphasis, one drawback of the approach is the sensitivity to measurement noise in the estimates of the system response, which in this case propagates through the matrix inversion. The approach was tested for interactions between the Z2Y and Y shim channels and it was shown that the cross-term fields could be much reduced. A small response in the Y field to input in the Z2Y shim channel however remained also after pre-emphasis. The reason for this residual cross-term is not yet fully understood. Plausible causes include non-linear interactions between the Z2Y and the Y shim channels and higher-order fields that are projected onto lower orders in response measurements with a 3rd-order dynamic field camera.

The concept of passing the input through a pre-emphasis filter in order to improve the field response relies on the gradient or shim system being largely linear and time-invariant. This holds for the most

prominent, but not for all, effects that influence the field dynamics. Not included in the linear model are for instance amplifier non-linearities and concomitant fields, which must be handled with other correction methods (87). Furthermore, the system response may change slightly depending on the state of the scanner, e.g. due to gradient heating (88). Owing to the easy implementation of the GIRF-based pre-emphasis filter, it may be feasible to update the pre-emphasis to match the current state of the system. The updated pre-emphasis could be based on quickly re-measuring the GIRF, from which the appropriate pre-emphasis could be automatically calculated. Alternatively, for reproducible effects the changing system response may be correlated with external parameters, such as temperature, and be calibrated beforehand.

The frequency response of the system can be improved by passing the input through a pre-emphasis filter. Unless the response is brought to unity at all frequencies, however, a distortion-free output waveform cannot be guaranteed for all possible inputs. At the same time, excessively boosting frequencies attenuated by the system may cause the input waveforms after pre-emphasis to violate time-domain hardware limits, such as amplitude and slew rate limits. This dilemma can be surpassed by taking a sequence-by-sequence optimization approach. It is thereby possible to find the input waveform yielding the highest output waveform fidelity achievable within system hardware capabilities for each targeted field waveform. The optimization approach can be adjusted to different objectives, such as minimizing field deviations or errors in the time-integral of the gradient field. The latter is preferred for optimizing imaging gradient sequences, whereas the former may be more suitable for e.g. dynamic shimming purposes.

It was here shown that the fidelity of common imaging trajectories on a commercial MR system with standard pre-emphasis compensation was improved by optimization. The results of the optimization could be enhanced by slightly reducing the amplitude and slew rate limits of the reference input waveform, thereby yielding more room for modifications of the sequence by the optimization algorithm. This however increases the length of the gradient sequence required to traverse a given k-space trajectory. Fundamentally, there is a trade-off between speed and accuracy when it comes to realizing defined k-space

trajectories. With infinite time the error between actual and targeted trajectories could be made arbitrarily small for any trajectory. In practice, a suitable compromise has to be chosen, which may vary depending on application. In the present work, the relation between sequence length and trajectory accuracy was probed by optimizing a set of gradient sequences for each trajectory. It would be desirable to automatize this process, for example by searching for the fastest possible gradient sequence that can traverse a trajectory with a defined maximal error, given a specific system frequency response and time-domain limitations. The design of such an algorithm is an open problem to be addressed in the future.

One further challenge of the optimization approach is the computation time required for the optimization. In the implementation here, computation times on the order of hours on a standard desktop CPU were required for the optimization of gradient sequences of a few thousand sample points (about 30 ms sampled at 6.4 µs). This would be prohibitively long for on-the-fly calculations of input waveforms, but is feasible for optimizing gradient sequences for pre-determined trajectories. Shorter or more coarsely sampled gradient sequences naturally require less computation time – scaling approximately linearly with the number of sampling points. One could investigate further refinements of the optimization algorithm to reduce computation time. For example, repeated elements of long sequences could possibly be modularly optimized, with the modules covering at least the length of the gradient impulse response.

From a system design perspective, increased control over the field dynamics by pre-emphasis may serve to relax the requirements on hardware perfection for such systems. Pre-emphasis does however not completely eliminate the need for accounting for remaining field imperfections at a post-acquisition stage. As gradient and shim systems are physical systems with limited bandwidth and power, there will always exist waveforms that cannot be perfectly fulfilled on the system.

Chapter 5

Image reconstruction using the gradient impulse response for trajectory prediction

Manuscript in preparation

5.1 Introduction

Fast imaging techniques are indispensable for a number of widely used applications in MRI, such as functional MRI and diffusion-weighted imaging. The techniques depend on fast coverage of k-space, which is often achieved by using echo-planar imaging (EPI) or spiral sampling patterns. This typically requires the gradients to be employed at the limits of the system capabilities and to be switched rapidly during the course of the acquisitions. Despite much engineering work having been dedicated to perfect gradient hardware, actual gradient time-courses generally deviate significantly from the prescribed gradient time-courses. This is due to a number of effects, including amplifier bandwidth limitations, eddy currents, coil vibrations and gradient delays. If not accounted for, deviations from the ideal field time-courses can have detrimental effects on the reconstructed images. For EPI images, the artifacts often take the form of ghosting, predominantly the persistent Nyquist ghosting observed in close to all EPI images.

Many correction strategies have been developed to overcome the problem of imperfect gradient time-courses. For EPIs, it is common to correct phase offsets between odd and even readout lines, using data acquired in a separate reference scan (74,89–91). The reference scan typically consists of a few readout lines through the center of k-space, from which phase inconsistencies between lines can be estimated. Other techniques estimate similar parameters directly from the acquired images using regions without overlaps between object and ghost (92–95). Some methods take advantage of having a time-series of data and alternate the direction of the readout gradient in every second scan in order to estimate fully sampled images from readout lines acquired in a single direction (96,97). Others make use of k-space representations of receive coil sensitivities to detect and correct for phase inconsistencies between readout lines (98,99). Each of these techniques relies in one way or the other on having redundant information in the acquired data. The redundancy can then be used to estimate the necessary corrections. Furthermore, all of the mentioned techniques are specifically designed to correct for artifacts arising from EPI trajectories only. In order to handle other classes of trajectories, such as spirals or modified EPIs

(e.g. density-weighted EPIs), they would either require thorough modification or would not be applicable.

A more versatile strategy is to measure the k-space trajectory itself. Image reconstruction can then be based on the measured trajectory, instead of an ideal assumed trajectory (31,100–102). Several techniques exist for obtaining estimates of actual k-space trajectories. Some are based on MR acquisitions from a phantom or directly from the subject (30–32,77). These however generally require modifications to the imaging sequence and rely on repeated acquisitions for each gradient direction to be measured. A faster alternative to measure the gradient fields is to use a dynamic field camera based on small NMR probes (6,7,35,38). This allows for estimates of the dynamic fields of different spatial distribution to be obtained in a single acquisition without sequence modifications. Measuring the gradient sequence as a calibration step, however, requires a separate calibration scan for each trajectory to be corrected for. As a consequence, any modification to the trajectory, such as altered field-of-view, resolution or gradient parameters, requires a new calibration measurement to be performed.

A technique which does neither increase scan time, nor require sequence modifications or extra calibration scans is to measure the gradient fields concurrently with the imaging experiment using NMR field probes that are decoupled from the imaging experiment by frequency separation (36). This however requires a complex hardware setup, which may not be accessible at every site.

A more generic approach that has recently been introduced is to determine the impulse response of the gradient system (57,58,82). Knowing the gradient impulse response function (GIRF), the field response in the scanner to any input gradient sequence can be estimated. In this work, we investigate the feasibility of performing image reconstruction on EPI trajectories estimated from the measured gradient impulse response, and compare it to results obtained with concurrent field monitoring. The GIRF measurement can be performed as a one-time calibration of the system, and can be designed to characterize also cross-term field responses.

5.2 Methods

Measurements were performed on a 3T Philips Achieva system (Philips Healthcare, Best, The Netherlands). Gradient system characterization was performed as described in Ref. (57). In brief, 12 different triangular pulses (slew rate 180 T/m/s, time-to-peak 50 – 160 us at 10 us increment) were given as input to each gradient channel separately. The resulting field responses were measured with a dynamic field camera consisting of 16 ^{1}H NMR field probes distributed as on the surface of a sphere of 10 cm radius (6,7,35,38). Spherical harmonic basis functions of 0th to 3rd order were fitted to the measured field responses. Each GIRF was calculated by a least-squares combination of response data from the different input pulses in the frequency domain.

Single-shot EPI data was acquired from a spherical phantom (35 ms TE, 42 ms T_{acq}, 22x22 cm^2 FOV, 88x88 matrix, axial slices) and the brain of a healthy volunteer (31 ms TE, 32 ms T_{acq}, 23x23 cm^2 FOV, 76x76 matrix, lightly angulated axial slices). During the acquisitions the gradient fields were measured with high temporal resolution using concurrent field monitoring (36). To this purpose, 9 ^{19}F field probes were employed, allowing for fitting spherical harmonics of 0th-2nd order to the measured fields.

GIRF-based prediction of the output gradient waveforms was performed by a frequency-domain multiplication of the input gradient sequence with the measured GIRFs:

$$G_m(\omega) = \sum_l I_l(\omega) \cdot GIRF_{l,m}(\omega) \, , \qquad [5.1]$$

where $I_l(\omega)$ is the input in the lth gradient channel, $GIRF_{l,m}(\omega)$ represents the transfer function from input in the lth gradient channel to output in the mth field term, and $G_m(\omega)$ is the field response in the mth field term (57). The GIRF-based predictions thus included also cross-term responses. Predictions were obtained both for the linear gradient fields and for field responses of 0th order, i.e. a spatially uniform field component. The time-domain waveforms were subsequently obtained by inverse Fourier transform of $G_m(\omega)$. To obtain the k-space phase coefficients, $k_i(t)$, the nominal and predicted gradient sequences, $g_i(t)$, were integrated over time:

$$k_i(t) = \gamma \int_o^t g_i(\tau) d\tau \ . \qquad\qquad [5.2]$$

Image reconstruction was performed with a gridding-based Fourier transform embedded in an iterative conjugate gradient algorithm (103–105). No EPI phase correction was applied to the data. Reconstructions based on nominal trajectories were performed with and without a time-shift of the trajectory to account for gradient delays. The delay parameters were estimated by comparing the times at which the trajectories passed the center of k-space in the readout direction between nominal and concurrently measured trajectories.

To account for measured or predicted spatially uniform phase modulations, the imaging data was demodulated by the 0th-order field integrals $k_0(t)$ before reconstruction. Reconstructions based on GIRF-predicted trajectories were performed with and without this demodulation, in order to investigate the significance of cross-term predictions in the 0th-order field. In the concurrently measured 0th-order phase coefficients, a component linear over time was identified as stemming from lower-order projections of concomitant field terms from the linear gradients. A time-linear spatially uniform phase induces a shift in the image for EPI sampling schemes. For better comparison between nominal, predicted and concurrently monitored reconstructions, this linear component was therefore subtracted from the monitored $k_0(t)$ before image reconstruction. In summary, images were reconstructed based on:

- (a) the nominal trajectory (no EPI phase correction)
- (b) the nominal trajectory shifted by 0.9 μs and 1.8 μs for the phantom and the *in vivo* data, respectively
- (c) the GIRF-predicted trajectory, without 0th-order phase demodulation
- (d) the GIRF- predicted trajectory, including demodulation by the predicted $k_0(t)$
- (e) the concurrently monitored trajectory, including demodulation by the measured $k_0(t)$ corrected for a time-linear component due to concomitant fields

For the *in vivo* data, the reconstruction was complemented by static off-resonance correction based on a separately acquired B_0-map. The B_0

correction was implemented as a multifrequency interpolation reconstruction algorithm, described in (106).

5.3 Results

The nominal, measured and GIRF-predicted trajectories for the phantom EPI acquisitions are shown in Fig. 5.1A. The measured trajectory deviates significantly from the nominal trajectory, especially at the turns. The GIRF-predicted trajectory closely follows the measured trajectory, with slight deviations only. In the readout direction, the maximum k-value reached for the measured trajectory is 50 rad/m less than prescribed, implying that the true resolution of the image is slightly lower than desired. This suppression in the readout direction is to be expected due to low-pass characteristics of the gradient system, and will vary with the main frequency of the EPI readout gradient. The EPI readout frequency primarily depends on gradient slew rate and amplitude performance and the choice of image resolution.

Figure 5.1B shows the difference between nominal vs. measured and GIRF-predicted vs. measured k-coefficients in the readout direction ($k_{RO}(t)$). The maximum error in $k_{RO}(t)$ is 51 rad/m for the nominal, and 9 rad/m for the GIRF-predicted k-coefficients. The root-mean-square of the error is reduced to 3.5 rad/m by GIRF-prediction from 35 rad/m in the nominal case. In the phase encoding direction ($k_{PE}(t)$) the error is smaller for both the nominal and the GIRF-predicted k-coefficients (Fig. 5.1C). The maximum error amounts to 39 rad/m and 4 rad/m for the nominal and the predicted k-coefficients, respectively, and the corresponding root-mean-square error is 3.7 rad/m and 1.1 rad/m.

The measured and predicted $k_0(t)$ are shown in Figure 5.1D. The 0th-order phase oscillates considerably with the EPI readout frequency, with a peak-to-peak amplitude of about 0.6 rad. This feature is largely predicted by the GIRF. During the readout, the maximum and root-mean-square prediction error is 0.2 rad and 0.06 rad, respectively (Fig. 5.1E).

Figure 5.2 and 5.3 show reconstructed images of phantom and *in vivo* data, respectively, in a linear and a log scaling. The images are based on reconstructions a), b), d) and e) as described in the Methods. In
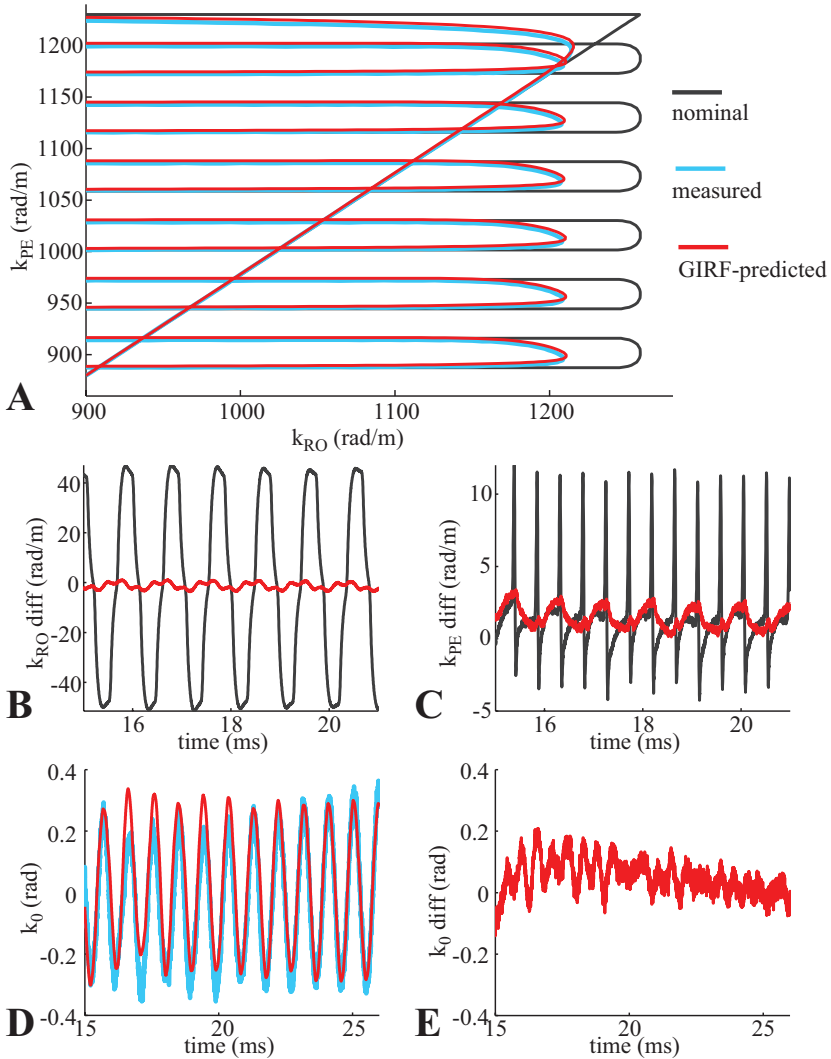
Fig. 5.1: *Nominal (black), measured (blue) and GIRF-predicted (red) k-space trajectory for an EPI sequence (**A**). **B** shows the difference in the k-coefficient in the readout direction (k_{RO}) for nominal and GIRF-predicted vs. measured k_{RO}, and **C** shows the difference in the phase encode direction (k_{PE}). In **D** the measured and the GIRF-predicted k_0 are plotted with the difference shown in **E**.*
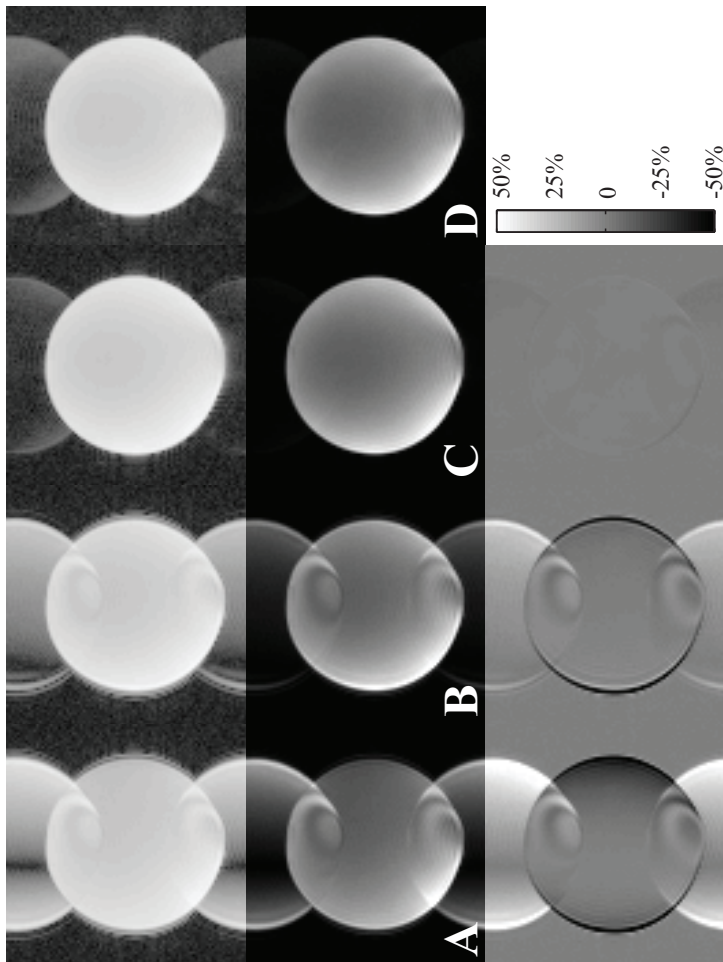
Fig. 5.2: *Phantom images reconstructed based on the nominal trajectory (**A**), the nominal trajectory with a delay (**B**), the GIRF-predicted trajectory, including demodulation by k_0 (**C**) and the concurrently monitored trajectory (**D**). The upper row shows the images in logarithmic scale, the middle row in linear scale and the lower row the difference to the concurrently monitored reconstruction, scaled to percent of maximum image value.*
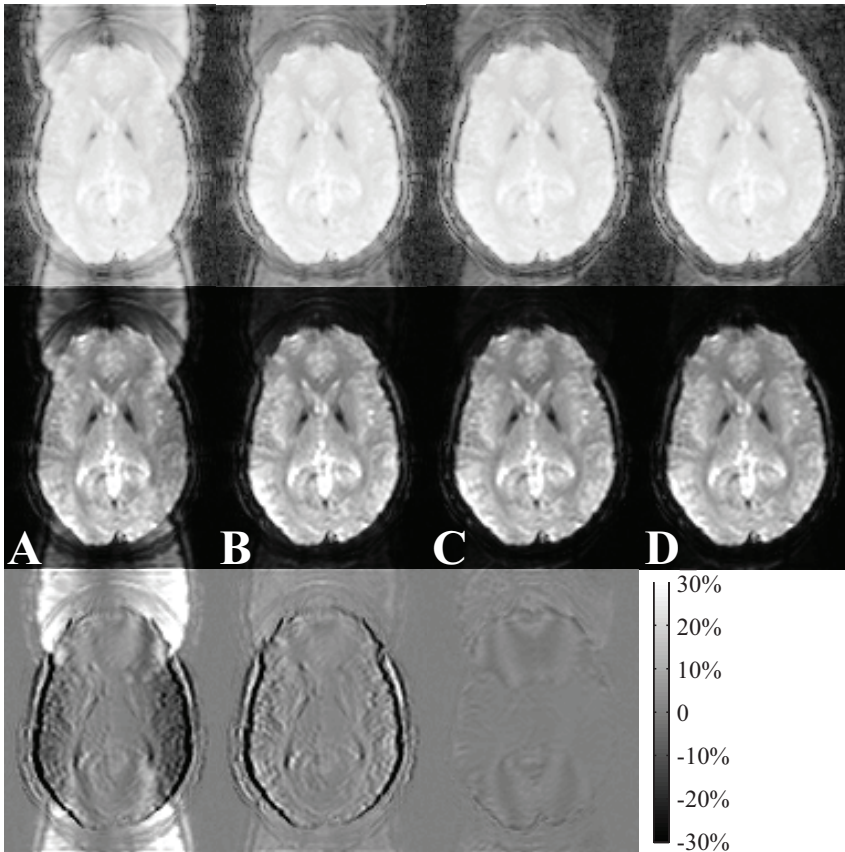
Fig. 5.3: *In vivo brain images reconstructed based on the nominal trajectory*
*(**A**), the nominal trajectory with a delay (**B**), the GIRF-predicted trajectory,*
*including demodulation by k_0 (**C**) and the concurrently monitored trajectory*
*(**D**). The upper row shows the images in logarithmic scale, the middle row in*
linear scale and the lower row the difference to the concurrently monitored
reconstruction, scaled to percent of maximum image value.

the bottom row of the figures are difference images compared to the monitored reconstruction, scaled to percent of maximum value in the monitored image. The reconstructions on nominal trajectories show strong ghosting artifacts (Fig. 5.2A and 5.3A), which can be reduced by introducing an appropriate delay on the trajectory (Fig. 5.2B and 5.3B). Looking at the difference images, it can be observed that the there is also a geometrical distortion, mainly appearing as a compression in the readout direction, compared to the monitored reconstruction. This distortion is not improved by the delay correction. Reconstructions based on concurrently measured trajectories show very low ghost levels, visible in the log-scale images only (Fig. 5.2D and 5.3D). Using the GIRF for trajectory prediction similar ghost levels as for the concurrently monitored images can be obtained, with a slightly increased ghost in the *in vivo* case (Fig. 5.2C and 5.3C). There is a high geometrical congruency between images based on monitored and GIRF-predicted trajectories, and consequently edges are not prominent in the difference images. A minimal skewing of the images based on GIRF-predictions can be observed both for the phantom and the *in vivo* case.

Figure 5.4 shows phantom reconstructions based on GIRF-predicted trajectories, with and without demodulation by the predicted 0th-order phase coefficient. The ghosting is considerably increased when $k_0(t)$ is not included in the reconstruction.
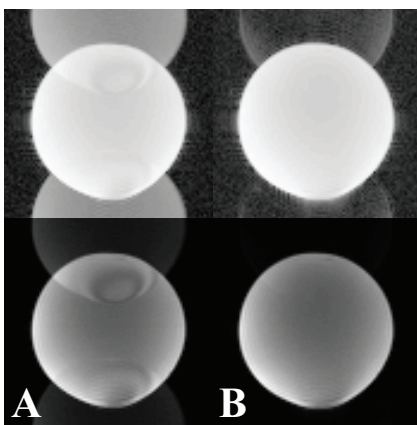
Fig. 5.4: *Phantom images reconstructed based on the GIRF-predicted trajectory, without and with demodulation by the predicted k_0 (**A** and **B**, respectively). The upper row shows the images in logarithmic scale and the lower row in linear scale.*

5.4 Discussion

In the work presented here, EPI images have been reconstructed using k-space trajectories estimated based on a linear time-invariant model of the gradient system. The quality of images reconstructed with GIRF-predicted trajectories was found to be comparable to using concurrent field monitoring for trajectory measurements. The GIRF-based method is not restricted to a particular type of trajectory, and thus has the potential to work as a general correction method for reproducible gradient imperfections. This would eliminate the need for application-dependent correction techniques, which often require acquisition of reference or calibration data and thus can increase scan time.

It was observed that to suppress EPI ghosts to a minimum the inclusion of predicted 0th-order field responses in the reconstruction was required. Generally, the GIRF-based method offers the possibility of correcting also for cross-term responses of any spatial order, if adequately characterized (57,82). For response measurements with a dynamic field camera, the number of field probes contained must match or exceed the number of spatial basis functions to be characterized. Cross-term responses may be of varying significance for different systems and applications. For systems that are not optimized for dynamic performance, such as higher-order shim systems, cross-terms can at times overshadow the self-term response (66). On most commercial gradient systems, on the other hand, they are likely to be less prominent, but still significant for sensitive applications (75). Here it could be noted that reconstructions based on concurrently monitored trajectories still contained slight residual ghosting, visible in the log-scale images. A possible cause for the remaining ghosting could be higher-order cross-term responses. If known, these can be accounted for by performing image reconstruction based on a higher-order signal model (39,68).

As every post-acquisition correction approach, the GIRF-based reconstruction will only deliver satisfactory results if the acquired signal contains adequate information. For k-space sampling, this amounts to having sufficient coverage of k-space, sampled in accordance with the Nyquist criterion. For larger field perturbations leading to loss of information, the reconstruction problem is inherently ill-conditioned.

In order to determine the GIRF of a system, the ability to measure field responses in the scanner bore is required. This can straightforwardly be done with a set of NMR field probes in a dynamic field camera. If no specialized hardware for field measurements is available, there are several phantom-based measurement techniques that can be used to acquire field responses (30–32,77). They generally have the disadvantage of being more time-consuming and yielding less measurement sensitivity. As the GIRF measurement can be performed as a one-time calibration of the system, however, the time required for the characterization is less crucial. A harder limit may be to adapt such techniques to acquire cross-term responses, especially of higher order.

The GIRF correction is only valid to the extent that the system is linear and time-invariant. This is largely true for most reproducible effects perturbing the field. There are however smaller non-linear contributions that are not included in the model. This concerns e.g. amplifier non-linearities and concomitant fields. The latter were here found to be a cause for an apparent 0th-order drift in the measured fields. To a first approximation, concomitant fields scale quadratically with the strength of the applied linear gradient fields (87). Knowing the gradient time waveforms a good approximation of the concomitant fields can be calculated analytically, and can be used both for correcting measured field data and for image reconstruction. The latter requires higher-order reconstruction algorithms, as concomitant fields for linear gradients primarily cause field terms of 2nd and higher spatial order.

A further violation of the assumption of linearity and time-invariance can be caused by a changing system response due to e.g. gradient heating. This has been shown to shift the frequency of oscillatory field responses (88). If the changes in the system response are reproducible, it may be possible to calibrate the effects and to dynamically update the GIRF with the changing state of the scanner.

Not possible to account for with the GIRF approach are non-reproducible field fluctuations, such as stemming from magnet drifts or movement of the subject in the scanner (14,107–109). If these become significant, it is necessary to acquire field measurements during the course of the scans. For slowly changing fields this can be performed with navigators techniques (110–112) or field monitoring (113–115). Faster field fluctuations require the capability of measuring the field

during acquisition of imaging data, which is possible using concurrent field monitoring (36,115). Concurrent field monitoring requires a specialized hardware setup, but has the additional advantage that also the time-courses of the imaging gradients can be directly captured in the measurements.

5.5 Conclusion

It has here been shown that image reconstruction based on GIRF-predicted field time-courses can reduce ghosting and geometric distortion in EPI images to a minimum. The GIRF needs to be determined only once for a given system, hence providing a correction method for gradient imperfections without additional reference acquisitions or sequence-by-sequence field monitoring. Also, GIRF-based image reconstruction is amenable to arbitrary k- space encodings without further customization, thus eliminating the need for a set of diverse correction methods tuned to specific applications or k-space sampling patterns. Furthermore, cross-term field responses can easily be integrated in the GIRF model, thus enabling correction of spatially uniform and 2nd- or higher-order field responses.

Chapter 6

Retrospective correction of physiological field fluctuations in high-field brain MRI using concurrent field monitoring

6.1 Introduction

MR imaging requires a stable main magnetic field, upon which time-varying gradient fields are added for signal encoding. Imperfect gradient time-courses or perturbations in the background magnetic field cause deviations from the desired encoding. If not accounted for, this can lead to ghosting artifacts, distortions, blurring and signal dropout in the acquired images. Field perturbations can have various origins and temporal characteristics. Certain effects are related to gradient operation such as eddy currents induced by gradient switching, field oscillations due to mechanical coil vibrations and thermal drifts caused by gradient heating. Others have origins unrelated to the current scan, e.g., slow magnet drifts or interfering fields from equipment in the close environment of the scanner.

Another significant source of dynamic field perturbations in *in vivo* experiments is the subject itself. Any movement of the subject changes the magnetic susceptibility distribution in the magnet bore and thereby alters the field distribution. This effect scales with tissue magnetization and therefore is most prominent at high background field strengths. This type of motion-induced field perturbations may substantially influence signal encoding even at some distance from the moving tissue. Breathing, in specific, involves motion of the chest wall, diaphragm, and abdomen, giving rise to field changes that have been shown to affect brain imaging at high field (14,15,108,110,116,117). Likewise, limb motion, speaking and swallowing have been shown to influence the quality of high-field neuroimaging (107,109,112,118,119).

Field perturbations are most detrimental to gradient-echo sequences with long echo times and multiple-shot acquisition, in which they cause shot-to-shot inconsistency of phase accrual. A prominent example of such sequences is T2*-weighted imaging, which is increasingly used for high-field brain imaging due to its rich magnitude and phase contrast (120–123). Enhanced T2* contrast at high field has opened up new possibilities for the investigation of various disorders of the brain, including multiple sclerosis and Alzheimer's disease (124,125). However, the aforementioned sensitivity to breathing-induced field fluctuations has been reported to impair image quality particularly in patients with Alzheimer's disease (15).

One key to correcting for physiologically induced field fluctuations is the ability to measure the perturbing fields during scans. To this end, navigator measurements have been incorporated in high-resolution T2*-weighted brain imaging (15,112) and fMRI time series (110,126,127). The separate navigator acquisition is typically included in the sequence before image encoding and acquisition, and the navigator data is commonly used to retrospectively correct the imaging data. However, depending on the given sequence, navigators can be difficult to accommodate and may alter contrast behavior, increase total scan time, or perturb signal steady-states. Most navigator techniques also rely on spatial uniformity of the perturbing field across the imaging volume (15,110,126), an assumption that does not generally hold true for physiologically induced fields (14,108,117). To address spatial variation, the navigator approach has been enhanced by 1D gradient encoding (112,127). However, the added gradient lobes further remove a given sequence from its original spin dynamics and still offer only rather limited spatial specificity of field information. To further enhance the latter, it has been proposed to obtain spatially varying field estimates by a sensitivity-weighted combination of navigator data from different receive coils (112). However, coil sensitivity patterns can be quite extended, particularly at high field, and thus again mediate field information of only limited spatial fidelity. Apart from the difficulties of obtaining spatially resolved field measurements, a general limitation to all navigator techniques is that they do not capture field dynamics during imaging readouts and thus require external field fluctuations to be sufficiently slow for accurate correction.

As an alternative to navigators, it has been proposed to estimate breathing-induced fields using a respiratory belt to guide the combination of pre-acquired field maps from different phases of the breathing cycle (128). This approach was implemented to steer real-time shim updates for brain imaging at 7T. A prerequisite for this approach is that the breathing belt signal can be reproducibly translated into the related field changes within the imaging volume. This requires calibration of the breathing field patterns on a per-subject basis. Fields deviating from these patterns, e.g., due to changes in breathing behavior or motion unrelated to breathing, will not be accounted for. In another method to estimate physiological field fluctuations, field measurements

were acquired with a field probe close to the volume of interest (113). Using a single field probe, however, is only valid under the assumption that the field fluctuations are spatially uniform, leading to biased corrections in the presence of non-uniform fields.

These considerations illustrate that field measurements for the correction of physiological fluctuations need to reconcile a number of key features and capabilities to achieve accuracy, efficiency and versatility at the same time. They must capture spatiotemporal field variations accurately, to sufficient order in space and with adequate temporal resolution. They should be accomplished without changing or imposing constraints on the imaging sequence to be stabilized. In particular, they should not require additional scan time or sequence timing changes and the field measurement should not alter the magnetization dynamics of tissue to be imaged.

To achieve this, in the present work we use an array of heteronuclear NMR field probes distributed around the imaging volume (6,36). Performing independent NMR experiments at a separate Larmor frequency (38,39), such probes readily operate concurrently with any given sequence and do not affect the magnetization state of the imaging target. The desired spatial order of field determination is achieved with an appropriate number of probes and suitable positioning, without pre-determination of expected field patterns. The high temporal resolution of the field probe measurements allows for capturing physiological field fluctuations along with any imperfections of gradient and shim operation. For image reconstruction, the full dynamics of the measured fields are incorporated in an extended signal model. In this way, full-bandwidth correction is achieved as opposed to the use of correction fields whose feasible bandwidth is limited by the latency of the sensing and actuation chains. The practical utility of the proposed approach is demonstrated for high-resolution T2*-weighted brain imaging at 7T, with a focus on breathing and limb motion as the most common physiological sources of bulk field perturbation in the head.

6.2 Methods

T2*-weighted gradient-echo imaging of the brain was performed in healthy volunteers on a whole-body 7T MR system (Philips Healthcare, Cleveland, USA), in compliance with the local ethics guidelines. In order to create defined physiological field changes, the volunteers were instructed to perform different tasks during the scans. The tasks included lying still and breathing normally, taking deep breaths throughout the acquisition, or repeatedly moving one hand from the side up to the chin. During each scan the dynamic field evolution was monitored with a set of ^{19}F NMR field probes (6,36,38,129). Magnetic field monitoring was performed in two variants of different temporal resolution. In one approach the full length of each imaging readout was monitored (termed *Concurrent field monitoring*) (119), whereas in the second approach a single, fast field measurement was performed between each readout and the subsequent slice excitation (termed *Snapshot field monitoring*) (115). The latter approach captures the field evolution only at a coarse temporal resolution of one sample per TR and is thereby inherently limited to the correction of slow field fluctuations. However, this option has the advantage of not being limited by dephasing of the probes due to the imaging gradients, rendering it feasible for use in conjunction with arbitrary image resolution.

The probe properties and the probe receive chains differed for the concurrent and the snapshot monitoring setups. Details specific to the two approaches are given in the subsections below. For both modes of operation, the field probes were mounted on the surface of a head receiver array and were distributed such as to provide good conditioning for a spatial expansion of the field evolution in terms of spherical harmonics up to 2nd and 3rd order, respectively (Tab. 6.1) (7).

GRE imaging sequence
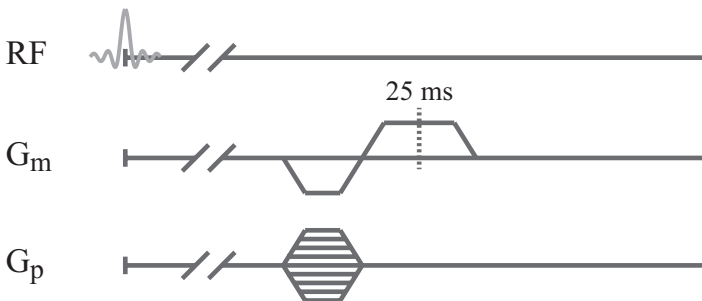
Field monitoring
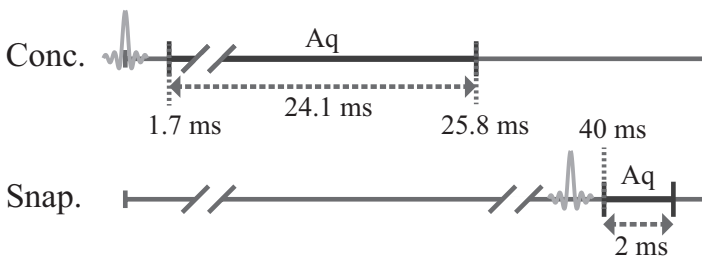
Fig. 6.1: *Schematic of the employed gradient-echo imaging sequence including the timing of probe excitation and acquisition for both the concurrent (Conc.) and the snapshot (Snap.) monitoring approach.*

Order	Spherical harmonic	Field coefficient	Phase coefficient
0	1	B_0	k_0
1	x	G_x	k_x
	y	G_y	k_y
	z	G_z	k_z
2	xy	B_4	k_4
	yz	B_5	k_5
	$2z^2 - (x^2 + y^2)$	B_6	k_6
	xz	B_7	k_7
	$x^2 - y^2$	B_8	k_8
3	$3yx^2 - y^3$	B_9	k_9
	xyz	B_{10}	k_{10}
	$5yz^2 - y(x^2 + y^2 + z^2)$	B_{11}	k_{11}
	$2z^3 - 3z(x^2 + y^2)$	B_{12}	k_{12}
	$5xz^2 - x(x^2 + y^2 + z^2)$	B_{13}	k_{13}
	$z(x^2 - y^2)$	B_{14}	k_{14}
	$x^3 - 3xy^2$	B_{15}	k_{15}

Table 6.1: *Real-valued spherical harmonics used as spatial basis functions for the phase and field coefficients measured with a set of 16 NMR field probes.*

Concurrent Field Monitoring

For concurrent field monitoring 13 unshielded transmit/receive probes containing perfluoropinacol as NMR-active compound were employed. The probes were doped with Fe(III)acac to yield a T2 of about 60 ms. The inner diameter of the probe capillaries was 0.8 mm, which results in a theoretical limit of about 0.4 mm in terms of image resolution up to which k-space trajectories can be fully monitored (7). The probes were excited at the [19]F Larmor frequency via a separate signal generator and RF amplifier, and the probe signal was received through vacant channels of the scanner spectrometer. Before feeding the signal from the field probes to the spectrometer it was passed through a custom RF mixing

stage (ZX05-10L+, Mini-Circuits, NY, USA) shifting it to the same intermediate frequency as for the ^{1}H signal.

The baseline frequency offset of each probe was determined in an acquisition without gradient fields present and the positions of the probes were obtained from the frequency shift of the probe signal under static gradients applied in each direction (7). Residual radiofrequency coupling between the probe channels was determined by a set of reference probe measurements using static gradients in different orientations to spectrally separate signals from different probes. Assuming linear coupling, the observed signal cross-talk was used to determine a coupling matrix by least-squares fitting. Decoupling of eventual probe signals was then achieved by applying the inverse of the coupling matrix before further processing.

Axial images were acquired with a standard RF-spoiled Cartesian gradient-echo sequence with 0.75x0.75 mm^2 in-plane resolution, 2 mm slice thickness, FOV 220x220 mm^2, TE 25ms, TR 800ms and 45° flip angle. [1]H imaging signals were received with a 16-channel head receive array (Nova Medical, MA, USA), leaving 16 spectrometer channels available for probe signal acquisition. For each acquired k-space line the probes were excited simultaneously with the imaged slice. The acquisition of field probe signal was started shortly after excitation and continued until the end of the imaging readout, covering 24.1 ms in total (Fig. 6.1). Spherical harmonic spatial basis functions of 0th - 2nd order were fitted to the measured probe phase evolutions after rescaling by the ratio of ^{1}H and ^{19}F gyromagnetic ratios. In the resulting time-dependent phase expansion, k_0 represents a global, spatially uniform ^{1}H phase term, the regular k_x, k_y, k_z describe first-order encoding in terms of the k-space trajectory, and the remaining coefficients reflect encoding of second order in space (Tab. 6.1). Corresponding instantaneous field terms (B_0, G_x, G_y, G_z, …) are obtained by taking the time derivative of the phase coefficients and dividing by the gyromagnetic ratio of [1]H.

Monitoring of the imaging gradient sequence was additionally performed without a subject in the scanner for use as a reference field evolution upon image reconstruction. The reference measurements were thus unaffected by physiological field fluctuations but contained any

reproducible field imperfections such as caused by eddy currents and bandwidth limitations of the gradient system.

Snapshot Field Monitoring

The snapshot field measurements were performed with 16 transmit/receive field probes containing hexafluorobenzene doped with Cr(dpm)3 to yield a T2 of about 30 ms. The inner diameter of the probe capillaries was 1.1 mm. This set of probes was additionally equipped with radiofrequency shielding and cable traps to reduce cable shield currents, coupling of ^{1}H excitation pulses from the head transmit coil into the probe cables and probe-to-probe coupling. The probes were excited via a separate RF excitation chain and their signals were received with a stand-alone spectrometer based on generic ADC, FPGA and controller components (National Instruments) (42). The baseline frequency offset and the position of each probe as well as the coupling matrix were determined in the same fashion as described above for concurrent field monitoring.

Image data was acquired with the same gradient-echo sequence as described above yet at 0.3x0.3 mm^2 in-plane resolution, 3 mm slice thickness, FOV 230x230 mm^2. 8 axial slices were acquired with a gap of 6 mm. ^{1}H imaging signals were received with a 32-channel head receiver array (Nova Medical, MA, USA). For each subject, regular static B0 shimming was performed with a pencil-beam algorithm. During the imaging sequence, snapshot field measurements were performed in gradient-free windows between each readout and the subsequent excitation (Fig. 6.1). In each of these windows, probe signals were acquired for 2 ms, yielding a single field value per probe by phase extraction and linear regression. The 16-probe array then permitted spherical harmonic field expansion up to full 3rd order.

For reconstruction, the observed field perturbations were assumed to have been constant over the respective sequence repetition from slice excitation to the field measurement. On this basis, the measured field coefficients were translated into time-linear coefficient excursions in the spherical harmonic phase model. The underlying unperturbed reference trajectory was calculated based on the nominal FOV and resolution.

Image Reconstruction

To study the effects of the physiological field perturbations as well as the required spatial order of measurement and correction, images were reconstructed using information of measured field fluctuations to different spatial orders and were compared to reference reconstructions. The latter were in the case of concurrent monitoring based on measured trajectories obtained without a subject in the scanner, and in the snapshot case based on nominal trajectories. In total, images were reconstructed in the following variants:

a) based on the reference trajectory unaffected by physiological field fluctuations
b) including measured 0th-order field fluctuations
c) including 0th- and 1st-order field fluctuations according to a 1st-order field model based on 4 selected probes
d) including 0th- and 1st-order field fluctuations according to a higher-order field model based on all probes
e) including the entire higher-order field model up to 2nd and 3rd order respectively.

Due to field fluctuations as well as minor imperfections of the measured reference trajectories the effective sampling patterns were not perfectly Cartesian. For a-d), images were therefore reconstructed with convolution-based Fourier interpolation (gridding) and fast Fourier transform, embedded in an iterative conjugate-gradient algorithm for optimal density compensation (104,105,130). To account for 0th-order fields, the object signal was demodulated with the applicable measured or reference k_0 before reconstruction. For e), a higher-order signal model as described in Ref. (39) was used and the reconstruction was again performed with an iterative conjugate gradient algorithm (39). All reconstructions were implemented in Matlab (Mathworks, MA, USA), with the large matrix-vector multiplications of the higher-order reconstructions performed on a graphics processor unit (Tesla M2050, Nvidia, CA, USA) to increase computation speed (131,132).
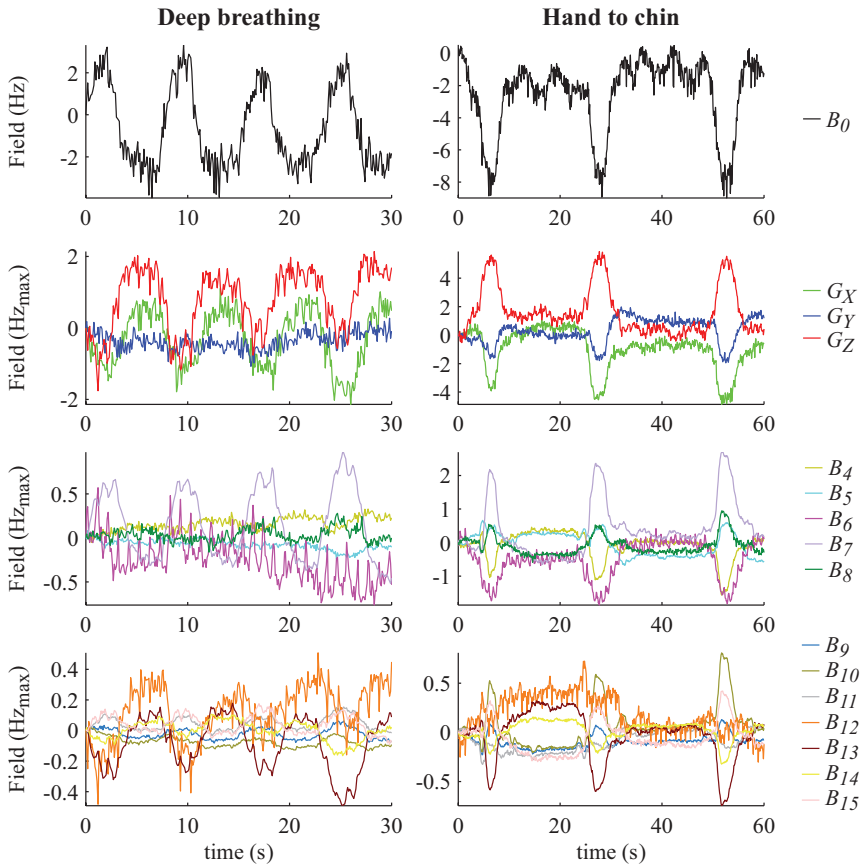
Fig. 6.2: *Example of measured field fluctuations during deep breathing (left), and moving one hand up to the chin (right), shown for fields up to 3rd-order real-valued spherical harmonics (Table 6.1). To compare fields of different spatial orders, all field terms are scaled to maximum field shift within a sphere of 20 cm diameter (Hz$_{max}$). The displayed field fluctuations were obtained during data acquisition for the images shown in Fig. 6.4 (hand-to-chin) and Fig. 6.5 (deep breathing).*

6.3 Results

Field fluctuations caused by breathing were apparent for all subjects. During deep breathing the 0th-order field showed a peak-to-peak variation in the range of 3-7 Hz for the different subjects (Fig. 6.2). In the linear field terms, clear breathing-related fluctuations were observed in the z-direction (feet-head) and in the x-direction (anterior-posterior) but, for most subjects, not in the y-direction (left-right), reflecting the approximate symmetry of the lungs and thorax. Across all subjects, the peak-to-peak variations in the linear field terms ranged up to 6 Hz at 10 cm distance from the isocenter. Smaller effects were measured in the 2nd- and 3rd-order field terms. The field fluctuations observed when moving a hand to the chin showed large inter-subject variability. In the 0th order, shifts of 6-16 Hz were measured while the 1st-order field terms fluctuated by up to 12 Hz at 10 cm distance from the isocenter. The contribution of higher-order fields was also larger for the hand-to-chin movement than for deep breathing. This behavior was expected since the hand as the source of field perturbation moved closer to the imaging volume than the chest.

Without correction, images acquired during deep breathing were subject to a range of artifacts including ghosting and intensity modulations, which often had the appearance of stripes across the image (Fig. 6.3). Using field monitoring to correct for the underlying field fluctuations resulted in a strong reduction of visible artifacts for both concurrent monitoring and the snapshot approach. The images acquired during hand movement showed similar artifact characteristics as for deep breathing (Fig. 6.4). However, in the hand-to-chin case artifacts were less evenly distributed, with most artifact power concentrated in the anterior part of the head where the strongest field distortions are expected. Also in this case similar image quality was recovered with concurrent monitoring and the snapshot approach. For both types of field perturbations, the corrections yielded large improvements in image quality over a range of slice levels in the brain (Fig. 6.5). Residual ghosting, ringing and intensity modulation were barely visible except in the most proximal slices where the field perturbations were largest and most likely not to be fully captured by the finite spatial order of field measurement and correction. No systematic difference in image quality

was observed between corrections based on concurrent monitoring and the snapshot approach. Data acquisition during shallow breathing and without limb motion was naturally exposed to smaller field perturbations. However, in these cases retrospective field correction still achieved subtle improvements in image quality (data not shown).

The role of the spatial order of data correction is studied in Fig. 6.6. Field correction based on the measured 0th-order fields only, generally yielded substantial improvements in image quality compared to reference reconstructions, especially for deep breathing. In most cases, however, 0th-order correction was not sufficient to reduce artifacts to below visibility (Fig. 6.6AB). Correction up to 1st order was usually sufficient, however in some cases it required to be based on data from more than 4 probes (Fig. 6.6CD). In a number of cases, including both deep breathing and hand movements, the reconstructions based on fields up to 2nd and 3rd order further visibly improved image quality (Fig. 6.6E).
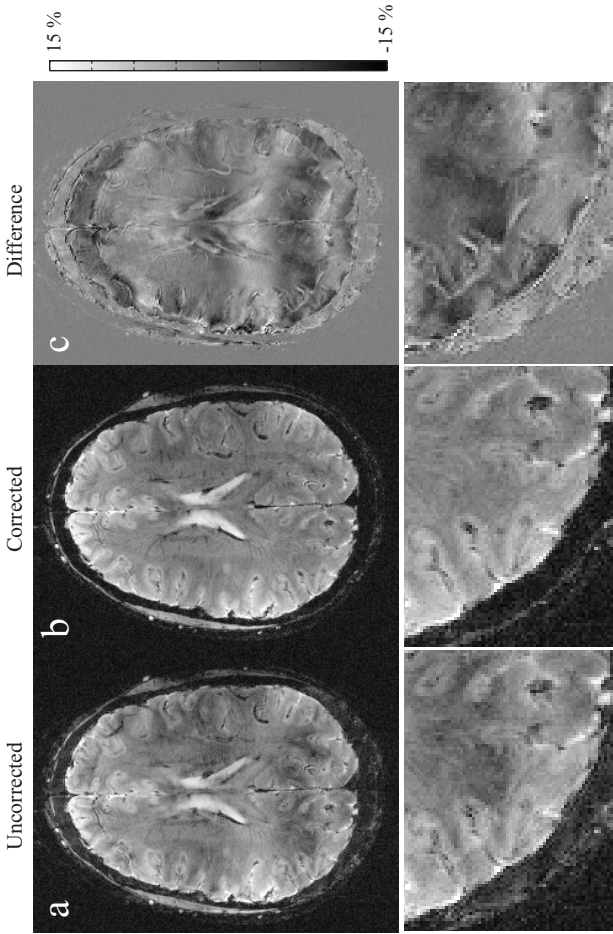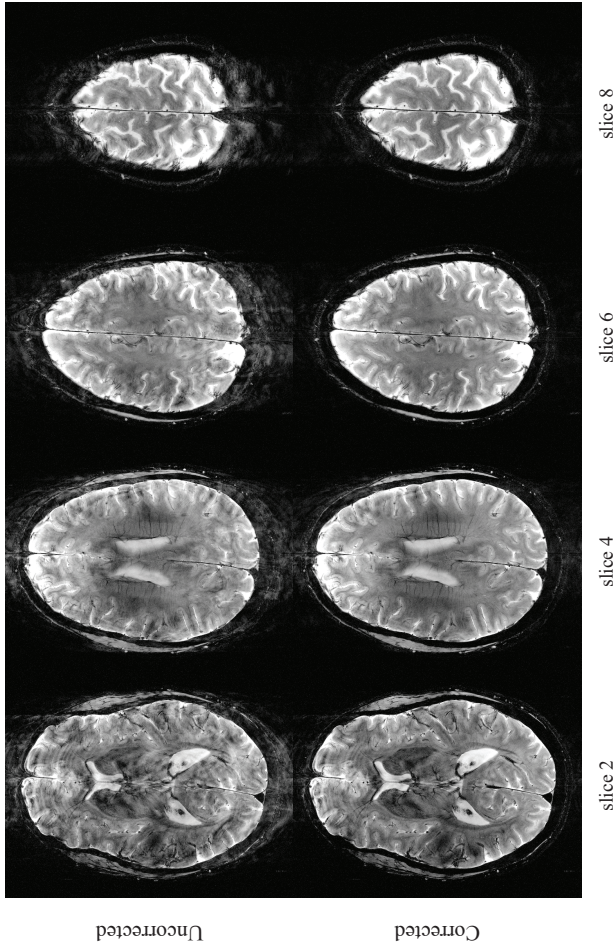
Fig. 6.3: *Image acquired during deep breathing and with concurrent monitoring during readouts, showing the reference reconstruction in **a**), the reconstruction including measured 0th-1st order fields, based on a 2nd order fit, in **b**) and the difference image between the two reconstructions in **c**). In the reference image both ghosting and intensity modulations are apparent, which are largely corrected for using field correction up to 1st order.*
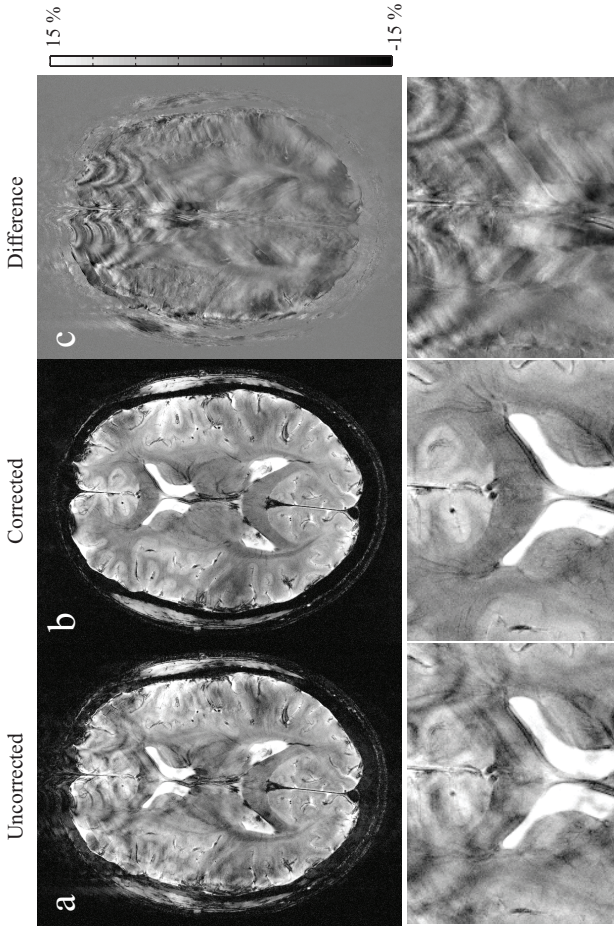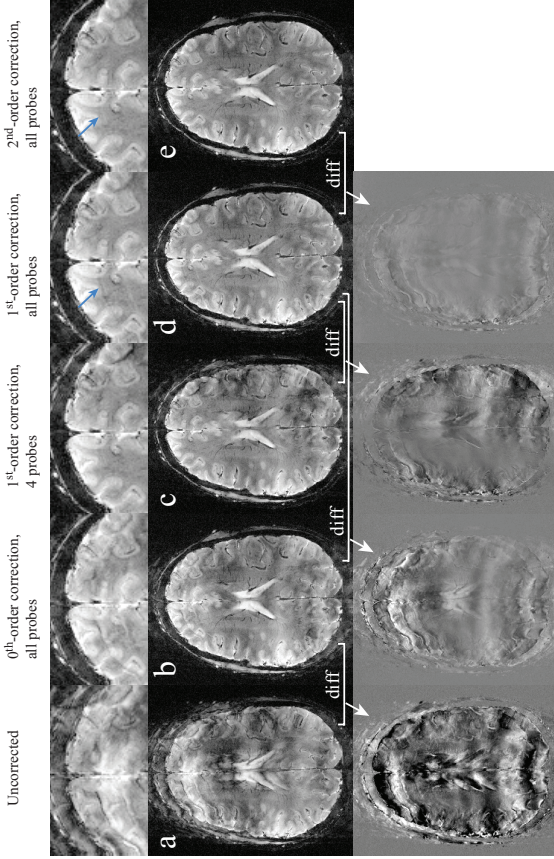
Fig. 6.4: *Snapshot-monitored image acquired as the subject was moving one hand up to the chin repeatedly, showing the reference reconstruction in **a**), the reconstruction including measured 0th-1st order fields, based on a 3rd order fit, in **b**) and the difference image between the two reconstructions in **c**). The ghosting in the reference reconstruction is mainly concentrated to the anterior part of the image, and is much reduced with the field correction up to 1st order.*

Fig. 6.5: *Four different slices acquired during deep breathing of the subject, obtaining field measurements with snapshot monitoring. In the top row the reference reconstructions are shown, and in the lower row are the reconstructions including up to 3rd-order field fluctuations. Strong ghosting artefacts are observed in all slices, which can be largely reduced with the correction based on field monitoring.*

Fig. 6.6: *Comparison of different reconstructions for one slice acquired as the subject moved one hand up to the chin repeatedly, monitored with concurrent monitoring. The reconstructions are based on the reference trajectory **a**), including measured 0th-order fields **b**), including 0th-1st-order fields based on a fit of data from 4 probes only **c**), including 0th-1st-order fields based on a 2nd-order fit of data from all probes **d**), reconstructed including measured 0th-2nd-order fields **e**). The reconstructions in **b**) and **c**) significantly improve quality in the anterior parts of the image, however simultaneously increasing the ghosting posteriorly. In **d**) a good overall image quality is observed. In **e**) the homogeneity of the image is somewhat further improved compared to **d**), and a slight remaining ghost in the anterior part of the image is decreased (arrow in inset).*

6.4 Discussion

In this work, a retrospective correction of physiological field perturbations based on measurements with ^{19}F field probes has been implemented for high-resolution T2*-weighted brain imaging at 7T. It was shown that image artifacts caused by field fluctuations due to breathing or hand movements could be well corrected for by incorporating the monitored fields of different spatial distribution in the image reconstruction. While 0th-1st order fields were generally sufficient to remove the majority of artifacts, it was observed that including data from more than 4 field probes in the fit yielded better results. This can be understood from the positioning of the field probes, which are necessarily distributed outside the volume of interest. If the number of probes is not sufficient to approximate the fields within the enclosed volume, higher-order fields may be projected onto lower orders in the fit. This may lead to a non-optimal correction, even when the fields within the imaging object itself could be well represented by a lower number of basis functions.

In some cases of both deep breathing and hand motion, accounting for 2nd- and 3rd-order fields in the reconstruction visibly improved image quality further. Generally, the spatial distribution of the physiologically induced fields will depend on the physiognomy of the subject and the type of perturbing motion. The closer the source of the field perturbation is to the imaging volume, the more significant the contribution of higher-order fields is expected to be. For perturbations originating inside the imaging volume, expansion into spherical harmonics will no longer be adequate. Image reconstruction including higher-order fields is practical but computationally demanding, especially for high-resolution imaging. Straightforward iterative solving of the higher-order signal model, e.g., by a conjugate-gradient algorithm requires explicit matrix-vector multiplications with large matrices (39). To increase reconstruction speed the encoding contribution of higher-order fields can be expanded into a sum of functions separable in time and space. Such expansion translates the signal model into a weighted sum of Fourier transforms and thus deploys the efficiency of Fast Fourier Transform for the loop operations (68).

The concurrent monitoring technique used in this work requires decoupling of the field measurement and the imaging experiment (38). This was achieved by using a different nucleus in the field probes than for image acquisition (36). A prerequisite for this approach is the capability of receiving multiple-channel signals from nuclei other than protons, which here was enabled by the use of RF mixers to receive fluorine signal through proton channels of the available spectrometer. As opposed to navigator correction techniques, concurrent monitoring allows for measuring fields independently of the magnetization state of the imaging object. As a consequence, the encoding fields during the full imaging readout can be measured along the way, thereby yielding information on faster field fluctuations as well as imperfections of the gradient waveforms, e.g., due to eddy currents. Depending on the specific implementation of the field monitoring, however, the imaging gradients may pose a limit to which sequences can be monitored. The field probe signal originates from liquid droplets in the probe capillaries (6,133), which can be fully dephased by a sufficiently large gradient moment. This effect limits the maximal k-space excursion and thereby the image resolution that can be monitored with a single excitation of probes of a given capillary diameter (7).

To reach higher image resolutions than given by the droplet diameter of the field probes, snapshot field monitoring was implemented. In this approach, a single field measurement per k-space line was acquired in a window of zero imaging gradients. Such a strategy is expected to work well when imperfections of the imaging gradients per se are negligible and physiological and external field fluctuations are sufficiently slow. Apart from increasing the possible image resolution, the snapshot monitoring comes with additional advantages in terms of probe design, such as allowing for larger probe diameters, which yield higher signal-to-noise ratios, and adjusting the relaxation parameters to enable faster re-excitation of the probes. The snapshot approach has been found effective for correcting field fluctuations induced by breathing or limb motion, implying that the field changes were sufficiently slow. This is in agreement with reports of successful correction based on navigators of similar temporal characteristics (15,112).

Snapshot monitoring is naturally not suited to correct for technical imperfections of sensitive gradient sequences, such as spiral readouts or long echo-planar imaging trains. However, many temporal gradient imperfections can be addressed by separate measurement of the impulse response of the gradient system, which permits rather accurate estimates of actual gradient waveforms (57,58,67,82). Image reconstruction can then be performed based on the estimated k-space trajectories combined with snapshot measurements of independent field fluctuations as implemented in the present work. In this combination, the low-bandwidth field measurements will capture slow field changes of external or internal origin, particularly those relating to thermal changes in the system, e.g., of passive shimming components. However, heating-related changes of gradient response characteristics and fast external field fluctuations are not covered in this way.

For greatest versatility of field correction it is desirable to rely on concurrent field measurements at full temporal bandwidth without restriction of gradient moments or interruptions for probe recovery and re-excitation. To achieve such continuous field monitoring, modifications of the field probe design and mode of operation have recently been proposed (42). The modified approach utilizes somewhat larger probes doped to very short relaxation times, ensuring that the probe signal decay is always dominated by T2 relaxation rather than gradient dephasing. A consistent yield of FID signal can then be obtained by re-excitation at a high rate (64). Using redundant sets of such probes with alternating excitation permits fully continuous comprehensive field measurement. One key challenge however is the net sensitivity, which benefits from larger probe droplets but suffers from the concatenation of multiple FIDs.

As an alternative to retrospective field correction as implemented here, field measurements with a set of NMR probes can also be used for feedback control employing gradient and shim coils to actively stabilize the field (113,134,135). A feedback implementation has the advantage of avoiding perturbations to the encoding that generally cannot be corrected for retrospectively. These include erroneous RF excitation leading to shifted and distorted slice profiles, changes in through-plane dephasing behavior, and the disruption of

steady-states. However, the bandwidth of the feedback loop limits the range of field perturbations that can be addressed in this way.

While addressing field fluctuations due to motion outside the volume of interest, the presented method is not applicable to correct for motion of tissue to be imaged. Additional explicit motion correction could be necessary since the head may move slightly in the course of breathing, especially when taking deep breaths. However, in previous studies it has been reported that breathing-related artifacts in long-TE gradient-echo images stemmed mainly from field fluctuations rather than bulk head motion (15,116). This is supported here by the observation that artifacts were well corrected for by addressing the field fluctuations only. In cases where head motion becomes limiting, techniques for correction of rigid body motion may be combined with correction of field fluctuations (136–138).

The present work focuses on correcting field fluctuations in T2*-weighted high-resolution anatomical brain imaging. However, a range of further applications could benefit from the presented technique. These include all types of imaging that are highly susceptible to field offsets and rely on data consistency over extended acquisition times such as fMRI time series and diffusion imaging with echo-planar readouts, phase-contrast flow measurements, susceptibility-weighted imaging, and quantitative susceptibility mapping, among others. The detrimental effects of field fluctuations are likely to be even more pronounced in 3D imaging schemes, which correspondingly could stand much to gain from accurate field corrections. Apart from imaging, also spectroscopy and spectroscopic imaging techniques suffer from artifacts induced by field fluctuations and could therefore benefit from enhanced correction. The magnitude of field perturbations due to magnetized tissue generally increases in proportion to field strength. Notably, several of the more vulnerable applications are commonly performed at high field precisely to benefit from enhanced local field variations. Therefore the significance of correction for physiological field fluctuations is expected to likewise increase with field strength.

6.5 Conclusion

It has previously been observed that fields stemming from motion of the subject can affect the quality of brain images at higher fields. In this work, a method for retrospective correction of such physiological field fluctuations based on concurrent magnetic field monitoring with ^{19}F NMR probes has been investigated. The presented approach captures fields of different spatial distribution and can easily be integrated into various types of imaging sequences. It was shown that artifacts due to breathing and limb motion could be greatly reduced in high-resolution T2*-weighted images of the brain at 7T. For good correction of physiologically induced field perturbations single field measurements per repetition time were shown to suffice. Optionally, the fields may be monitored at a high temporal resolution during imaging acquisition, thereby yielding information also on the actual waveforms of the imaging gradients.

Chapter 7

Outlook

Magnetic resonance imaging fundamentally requires the use of magnetic fields that vary both in space and in time. The accuracy of the time-courses of the applied fields has been an issue since the development of MRI, still being a limiting factor today for certain applications. In the present thesis, the dynamics of such fields have been described by a model assuming linearity and time-invariance (LTI). Methods for determining the impulse response of systems producing time-varying fields have been investigated and characterizations of the gradient and shim systems of commercial MR scanners have been performed. Instrumental for this approach has been the ability to quickly and accurately measure field responses using small NMR field probes.

One advantage of the proposed method for system characterization is that the physical mechanisms influencing system behavior do not need to be known and modeled separately. To better understand the system, however, it may be desirable to compare physically driven models of the system with results obtained from measurements. This may for instance be done by modeling eddy currents flowing in different structures of the scanner or mechanical coil vibrations giving rise to field oscillations. The latter requires models of coil vibrational modes, which also relate to the acoustic response of the system. Comparing the acoustic frequency response of the system with the field response may therefore add further insight on mechanical properties of the system. A one-to-one correspondence between acoustic resonances and field resonances can however not be expected, as the scanner constitutes a complex mechanical structure of which not all components are current-carrying.

Building upon the proposed characterization of dynamic fields, novel approaches to modifying input waveforms to gradient and shim systems for increased accuracy of the time-courses of the output fields have been explored in this thesis. Furthermore, the ability to predict field responses to any given input pulse for a system with a known impulse response was employed to estimate actual k-space trajectories for commonly used echo-planar imaging sequences. Image reconstruction based on the estimated k-space trajectories showed greatly reduced artifacts due to field imperfections.

This work thus holds promise to ameliorate the problems of inaccurate field time-courses both by improving field waveform

accuracy and allowing for easy implementation of post-acquisition corrections for field imperfections. The former would be especially important for applications that do not readily lend themselves to post-acquisition corrections. An example of this is spatially selective excitation techniques that depend on traversal of k-space during RF application. Such excitation techniques frequently make use of spiral or radial trajectories, which are highly vulnerable to gradient imperfections. Also in the context of spatial signal encoding, field imperfections often pose problems for non-Cartesian trajectories. Certain applications completely rely on specialized non-Cartesian trajectories, e.g. to achieve specific density weighting of k-space, noise decoupling by trajectory perturbations or sampling optimality for compressed sensing. In such cases, the bandwidth constraints of a system could be considered in the trajectory design to obtain physically realizable sampling patterns.

As perfect field time-courses for all thinkable applications cannot be realized with real-world physical systems, the ability to correct acquired data for effects of field imperfections will continue to be of high significance. This is especially relevant for applications relying on fast imaging techniques, e.g. fMRI, and techniques that suffer from eddy currents due to large preparatory gradient pulses, e.g. diffusion. The corrections may also need to take cross-term field responses into account.

Taken together, these techniques for handling dynamic field imperfections could pave the way for more routine use of vulnerable trajectories and could possibly relax constraints on the field-producing hardware. The latter could reduce costs of MR systems and could be beneficial for the less mature hardware producing dynamic fields of higher spatial orders, which are necessary for dynamic shimming and non-linear spatial encoding. Most *in vivo* MR spectroscopy methods involve the use of dynamic gradient and/or shim fields as well, and consequently may also benefit from the methods developed in this work.

Gradient and shim system characterization was in this work performed with a 3rd-order dynamic field camera. By including an appropriate number of probes in the field camera, or performing repeated measurements with the camera in shifted positions, the field characterization could be extended to include any desired spatial order.

The proposed technique for system characterization holds to the extent that the system is truly linear and time-invariant. If deviations from this assumption become limiting, the characterization could possibly be further extended to include certain non-linear effects, such as harmonics of input frequencies and non-linear amplitude dependence of the system response. It may also be possible to model certain time-varying system responses, e.g. due to thermal variations of the system.

For non-reproducible field perturbations, the approaches mentioned above are not valid. Such effects require field measurements simultaneously with or in close proximity to the data acquisition for appropriate correction. In this thesis, concurrent field monitoring with fluorine-based NMR probes was used to correct for physiologically induced field fluctuations. Such field measurements may become the method of choice for applications that are highly sensitive to minor field variations.

References

1. Lauterbur PC. Image Formation by Induced Local Interactions: Examples Employing Nuclear Magnetic Resonance. Nature 1973;242:190–191.

2. Kumar A, Welti D, Ernst RR. NMR Fourier zeugmatography. J. Magn. Reson. 1969 1975;18:69–83.

3. Mansfield P. Multi-planar image formation using NMR spin echoes. J. Phys. C Solid State Phys. 1977;10:L55.

4. Liang Z-P, Lauterbur PC. Principles of Magnetic Resonance Imaging - A Signal Processing Perspective. New York, USA: IEEE Press; 2000.

5. McRobbie DW, Moore EA, Graves MJ, Prince MR. MRI - From Picture to Proton. Second edition. United Kingdom: Cambridge University Press; 2007.

6. De Zanche N, Barmet C, Nordmeyer-Massner JA, Pruessmann KP. NMR probes for measuring magnetic fields and field dynamics in MR systems. Magn. Reson. Med. 2008;60:176–186.

7. Barmet C, De Zanche N, Pruessmann KP. Spatiotemporal magnetic field monitoring for MR. Magn. Reson. Med. 2008;60:187–197.

8. Turner R. A target field approach to optimal coil design. J. Phys. Appl. Phys. 1986;19:L147.

9. Boesch C, Gruetter R, Martin E. Temporal and spatial analysis of fields generated by eddy currents in superconducting magnets:

Optimization of corrections and quantitative characterization of magnet/gradient systems. Magn. Reson. Med. 1991;20:268–284.

10. Liu Q, Hughes DG, Allen PS. Quantitative characterization of the eddy current fields in a 40-cm bore superconducting magnet. Magn. Reson. Med. 1994;31:73–76.

11. Wu YH, Chronik BA, Bowen C, Mechefske CK, Rutt BK. Gradient-induced acoustic and magnetic field fluctuations in a 4T whole-body MR imager. Magn. Reson. Med. 2000;44:532–536.

12. Clayton DB, Elliott MA, Leigh JS, Lenkinski RE. 1H Spectroscopy without solvent suppression: Characterization of signal modulations at short echo times. J. Magn. Reson. 2001;153:203–209.

13. Foerster BU, Tomasi D, Caparelli EC. Magnetic field shift due to mechanical vibration in functional magnetic resonance imaging. Magn. Reson. Med. 2005;54:1261–1267.

14. Van de Moortele P, Pfeuffer J, Glover GH, Ugurbil K, Hu X. Respiration-induced B0 fluctuations and their spatial distribution in the human brain at 7 Tesla. Magn. Reson. Med. 2002;47:888–895.

15. Versluis MJ, Peeters JM, van Rooden S, van der Grond J, van Buchem MA, Webb AG, van Osch MJP. Origin and reduction of motion and f0 artifacts in high resolution T2*-weighted magnetic resonance imaging: Application in Alzheimer's disease patients. NeuroImage 2010;51:1082–1088.

16. Jehenson P, Westphal M, Schuff N. Analytical method for the compensation of eddy-current effects induced by pulsed magnetic field gradients in NMR systems. J. Magn. Reson. 1990;90:264–278.

17. Van Vaals JJ, Bergman AH. Optimization of eddy-current compensation. J. Magn. Reson. 1990;90:52–70.

18. Wysong RE, Madio DP, Lowe IJ. A novel eddy current compensation scheme for pulsed gradient systems. Magn. Reson. Med. 1994;31:572–575.

19. Jezzard P, Barnett AS, Pierpaoli C. Characterization of and correction for eddy current artifacts in echo planar diffusion imaging. Magn. Reson. Med. 1998;39:801–812.

20. Zur Y, Stokar S. An algorithm for eddy currents symmetrization and compensation. Magn. Reson. Med. 1996;35:252–260.

21. Eccles CD, Crozier S, Westphal M, Doddrell DM. Temporal spherical-harmonic expansion and compensation of eddy-current fields produced by gradient pulses. J. Magn. Reson. A 1993;103:135–141.

22. Barnett A. Comments on "Gradient-induced acoustic and magnetic field fluctuations in a 4T whole-body MR imager." Magn. Reson. Med. 2001;46:207–207.

23. Nixon TW, McIntyre S, Rothman DL, de Graaf RA. Compensation of gradient-induced magnetic field perturbations. J. Magn. Reson. 2008;192:209–217.

24. Hedeen RA, Edelstein WA. Characterization and prediction of gradient acoustic noise in MR imagers. Magn. Reson. Med. 1997;37:7–10.

25. Li W, Mechefske CK, Gazdzinski C, Rutt BK. Acoustic noise analysis and prediction in a 4-T MRI scanner. Concepts Magn. Reson. 2004;21B:19–25.

26. Sierra CVR, Versluis MJ, Hoogduin JM, Duifhuis H. Acoustic fMRI noise: Linear time-invariant system model. IEEE Trans. Biomed. Eng. 2008;55:2115–2123.

27. Addy NO, Wu HH, Nishimura DG. Simple method for MR gradient system characterization. In: Proceedings of the 17th Annual Meeting of ISMRM, Honolulu, Hawaii, USA; 2009. p 3068.

28. Vannesjö SJ, Häberlin M, Kasper L, Barmet C, Pruessmann KP. A method for characterizing the magnetic field response of a gradient system. In: Proceedings of the 18th Annual Meeting of ISMRM, Stockholm, Sweden; 2010. p 1536.

29. Wysong RE, Lowe IJ. A simple method of measuring gradient induced eddy currents to set compensation networks. Magn. Reson. Med. 1993;29:119–121.

30. Terpstra M, Andersen PM, Gruetter R. Localized eddy current compensation using quantitative field mapping. J. Magn. Reson. 1998;131:139–143.

31. Duyn JH, Yang YH, Frank JA, van der Veen JW. Simple correction method for k-space trajectory deviations in MRI. J Magn Reson 1998;132:150–153.

32. Alley MT, Glover GH, Pelc NJ. Gradient characterization using a Fourier-transform technique. Magn. Reson. Med. 1998;39:581–587.

33. Goodyear DJ, Shea M, Beyea SD, Shah NJ, Balcom BJ. Single point measurements of magnetic field gradient waveform. J. Magn. Reson. 2003;163:1–7.

34. Balcom BJ, Bogdan M, Armstrong RL. Single-point imaging of gradient rise, stabilization, and decay. J. Magn. Reson. A 1996;118:122–125.

35. Barmet C, Wilm BJ, Pavan M, Pruessmann KP. A third-order field camera with microsecond resolution for MR system diagnostics. In: Proceedings of the 17th Annual Meeting of ISMRM, Honolulu, Hawaii, USA; 2009. p 781.

36. Barmet C, Wilm BJ, Pavan M, Katsikatsos G, Keupp J, Mens G, Pruessmann KP. Concurrent higher-order field monitoring for routine head MRI: an integrated heteronuclear setup. In: Proceedings of the 18th Annual Meeting of ISMRM, Stockholm, Sweden; 2010. p 216.

37. Lathi BP. Signal Processing and Linear Systems. Indian Edition. New York: Oxford University Press; 2008.

38. Barmet C, De Zanche N, Wilm BJ, Pruessmann KP. A transmit/receive system for magnetic field monitoring of in vivo MRI. Magn. Reson. Med. 2009;62:269–276.

39. Wilm BJ, Barmet C, Pavan M, Pruessmann KP. Higher order reconstruction for MRI in the presence of spatiotemporal field perturbations. Magn. Reson. Med. 2011;65:1690–1701.

40. Vannesjö J, Fillmer A, Barmet C, Boesiger P, Henning A, Pruessmann KP. Fast characterization of higher-order shim dynamics by impulse response measurements with a dynamic field camera. In: Proceedings of the 19th Annual Meeting of ISMRM, Montreal, Canada; 2011. p 719.

41. Giese D, Haeberlin M, Barmet C, Pruessmann KP, Schaeffter T, Kozerke S. Analysis and correction of background velocity offsets

in phase-contrast flow measurements using magnetic field monitoring. Magn. Reson. Med. 2012;67:1294–1302.

42. Dietrich BE, Barmet C, Brunner D, Pruessmann KP. An autonomous system for continuous field monitoring with interleaved probe sets. In: Proceedings of the 19th Annual Meeting of ISMRM, Montreal, Canada; 2011. p 1842.

43. Mansfield P, Chapman B. Active magnetic screening of gradient coils in NMR imaging. J. Magn. Reson. 1986;66:573–576.

43. Roemer PB, Hickey JS, inventors; General Electric Company, assignee. Self-shielded gradient coils for NMR imaging. US Patent 4,737,716. April 12, 1988.

45. Turner R. Gradient coil design: A review of methods. Magn. Reson. Imaging 1993;11:903–920.

46. Morich MA, Lampman DA, Dannels WR, Goldie FT. Exact temporal eddy current compensation in magnetic resonance imaging systems. IEEE Trans. Med. Imaging 1988;7:247–254.

47. Lechner SM, Sipilä PT, Wiesinger F, Kerr AB, Vogel MW. Spiral imaging artifact reduction: A comparison of two k-trajectory measurement methods. J. Magn. Reson. Imaging 2009;29:1485–1492.

48. Poser BA, Barth M, Goa P-E, Deng W, Stenger VA. Single-shot echo-planar imaging with Nyquist ghost compensation: Interleaved dual echo with acceleration (IDEA) echo-planar imaging (EPI). Magn. Reson. Med. 2013;69:37–47.

49. Klose U. In vivo proton spectroscopy in presence of eddy currents. Magn. Reson. Med. 1990;14:26–30.

50. Blamire A, Rothman D, Nixon T. Dynamic shim updating: A new approach towards optimized whole brain shimming. Magn. Reson. Med. 1996;36:159–165.

51. Morrell G, Spielman D. Dynamic shimming for multi-slice magnetic resonance imaging. Magn. Reson. Med. 1997;38:477–483.

52. De Graaf RA, Brown PB, McIntyre S, Rothman DL, Nixon TW. Dynamic shim updating (DSU) for multislice signal acquisition. Magn. Reson. Med. 2003;49:409–416.

53. Koch K, McIntyre S, Nixon T, Rothman D, De Graaf R. Dynamic shim updating on the human brain. J. Magn. Reson. 2006;180:286–296.

54. Juchem C, Nixon TW, Diduch P, Rothman DL, Starewicz P, De Graaf RA. Dynamic shimming of the human brain at 7 T. Concepts Magn. Reson. Part B Magn. Reson. Eng. 2010;37B:116–128.

55. Sengupta S, Welch EB, Zhao Y, Foxall D, Starewicz P, Anderson AW, Gore JC, Avison MJ. Dynamic B0 shimming at 7 T. Magn. Reson. Imaging 2011;29:483–496.

56. Hennig J, Welz AM, Schultz G, Korvink J, Liu Z, Speck O, Zaitsev M. Parallel imaging in non-bijective, curvilinear magnetic field gradients: a concept study. Magn. Reson. Mater. Phys. Biol. Med. 2008;21:5–14.

57. Vannesjo SJ, Haeberlin M, Kasper L, Pavan M, Wilm BJ, Barmet C, Pruessmann KP. Gradient system characterization by impulse response measurements with a dynamic field camera. Magn. Reson. Med. 2013;69:583–593.

58. Addy NO, Wu HH, Nishimura DG. Simple method for MR gradient system characterization and k-space trajectory estimation. Magn. Reson. Med. 2012;68:120–129.

59. Pintelon R. Chapter 5, Design of Excitation Signals. In: System identification: a frequency domain approach, 2nd ed. Hoboken, N.J: John Wiley & Sons Inc; 2012. p 151–175.

60. Vannesjo SJ, Dietrich BE, Barmet C, Wilm BJ, Brunner DO, Pruessmann KP. Measurement and pre-emphasis of shim responses using frequency sweeps. In: Proceedings of the 20th Annual Meeting of ISMRM, Melbourne, Australia; 2012. p 142.

61. Papoulis A. Section 8-1, Frequency Modulation and the Method of Stationary Phase. In: Signal Analysis, McGraw-Hill Book Company; 1977.

62. Silver M., Joseph R., Hoult D. Highly selective $\pi2$ and π pulse generation. J. Magn. Reson. 1984;59:347–351.

63. Tannús A, Garwood M. Improved Performance of Frequency-Swept Pulses Using Offset-Independent Adiabaticity. J. Magn. Reson. A 1996;120:133–137.

64. Dietrich BE, Brunner DO, Wilm BJ, Barmet C, Pruessmann KP. Analysis of Measurement Precision in Continuous Magnetic Field Monitoring. In: Proceedings of the 21th Annual Meeting of ISMRM, Salt Lake City, USA; 2013. p 2716.

65. Busch J, Vannesjoe SJ, Giese D, Barmet C, Pruessmann K, Kozerke S. Pre-emphasis Compensation of Oscillatory Phase Offsets in Phase-Contrast Flow Measurements. In: Proceedings of the 20th Annual Meeting of ISMRM, Melbourne, Australia; 2012. p 1172.

66. Vannesjo SJ, Dietrich BE, Pavan M, Barmet C, Pruessmann KP. Digital Cross-Term Pre-Emphasis for Higher-Order Dynamic Shimming. In: Proceedings of the 21th Annual Meeting of ISMRM, Salt Lake City, USA; 2013. p 671.

67. Graedel NN, Vannesjo SJ, Kasper L, Gross S, Dietrich BE, Barmet C, Pruessmann KP. Image Reconstruction Using the Gradient Impulse Response for Trajectory Prediction. In: Proceedings of the 21th Annual Meeting of ISMRM, Salt Lake City, USA; 2013. p 552.

68. Wilm BJ, Barmet C, Pruessmann KP. Fast Higher-Order MR Image Reconstruction Using Singular-Vector Separation. IEEE Trans. Med. Imaging 2012;31:1396 –1403.

69. Stockmann JP, Ciris PA, Galiana G, Tam L, Constable RT. O-space imaging: Highly efficient parallel imaging using second-order nonlinear fields as encoding gradients with no phase encoding. Magn. Reson. Med. 2010;64:447–456.

70. Mechefske C. Characterization of acoustic noise and magnetic field fluctuations in a 4 T whole-body MRI scanner. Mech. Syst. Signal Process. 2002;16:459–473.

70. Mansfield P, Chapman BLW, Turner R, Bowley RM, inventors; National Research Development Corporation, assignee. Magnetic field screens. US Patent 4,978,920. December 18, 1990.

72. Turner R, Bowley RM. Passive screening of switched magnetic field gradients. J. Phys. [E] 1986;19:876.

73. Carlson JW, Derby KA, Hawryszko KC, Weideman M. Design and evaluation of shielded gradient coils. Magn. Reson. Med. 1992;26:191–206.

74. Bruder H, Fischer H, Reinfelder H-E, Schmitt F. Image reconstruction for echo planar imaging with nonequidistant k-space sampling. Magn. Reson. Med. 1992;23:311–323.

75. Grieve SM, Blamire AM, Styles P. Elimination of Nyquist ghosting caused by read-out to phase-encode gradient cross-terms in EPI. Magn. Reson. Med. 2002;47:337–343.

76. Robison RK, Devaraj A, Pipe JG. Fast, simple gradient delay estimation for spiral MRI. Magn. Reson. Med. 2010;63:1683–1690.

77. Latta P, Gruwel MLH, Volotovskyy V, Weber MH, Tomanek B. Simple phase method for measurement of magnetic field gradient waveforms. Magn. Reson. Imaging 2007;25:1272–1276.

78. Schneider JT, Haas M, Ruhm W, Hennig J, Ullmann P. Robust spatially selective excitation using radiofrequency pulses adapted to the effective spatially encoding magnetic fields. Magn. Reson. Med. 2011;65:409–421.

79. Zheng H, Zhao T, Qian Y, Ibrahim T, Boada F. Parallel transmission RF pulse design for eddy current correction at ultra high field. J. Magn. Reson. 2012;221:139–146.

80. Vannesjö SJ, Kasper L, Pavan M, Barmet C, Pruessmann KP. On the feasibility of single-shot EPI during higher-order shim settling. In: Proceedings of the 18th Annual Meeting of ISMRM, Stockholm, Sweden; 2010. p 145.

81. Fischer RF, Barmet C, Rudin M, Boesiger P, Pruessmann KP, Kozerke S. Monitoring and compensating phase imperfections in cine balanced steady-state free precession. 2013.

81. Vannesjo SJ, Dietrich BE, Pavan M, Brunner DO, Wilm BJ, Barmet C, Pruessmann KP. Field camera measurements of gradient and shim impulse responses using frequency sweeps. Magn. Reson. Med. 2013;DOI:10.1002/mrm.24934.

83. Simonetti OP, Duerk JL, Chankong V. An optimal design method for magnetic resonance imaging gradient waveforms. IEEE Trans. Med. Imaging 1993;12:350–360.

84. Hargreaves BA, Nishimura DG, Conolly SM. Time-optimal multidimensional gradient waveform design for rapid imaging. Magn. Reson. Med. 2004;51:81–92.

85. Vogt C. Optimizing input signals for an MRI gradient system. ETH Zurich 2013.

86. Lustig M, Kim S-J, Pauly JM. A Fast Method for Designing Time-Optimal Gradient Waveforms for Arbitrary -Space Trajectories. IEEE Trans. Med. Imaging 2008;27:866–873.

87. Bernstein MA, Zhou XJ, Polzin JA, King KF, Ganin A, Pelc NJ, Glover GH. Concomitant gradient terms in phase contrast MR: Analysis and correction. Magn. Reson. Med. 1998;39:300–308.

88. Busch J, Vannesjo SJ, Barmet C, Pruessmann KP, Kozerke S. Analysis of Thermal Stability of Background Phase Errors in Phase-Contrast Flow Imaging. In: Proceedings of the 21th Annual Meeting of ISMRM, Salt Lake City, USA; 2013. p 69.

89. Hu X, Le TH. Artifact reduction in EPI with phase-encoded reference scan. Magn. Reson. Med. 1996;36:166–171.

90. Wan X, Gullberg GT, Parker DL, Zeng GL. Reduction of geometric and intensity distortions in echo-planar imaging using a multireference scan. Magn. Reson. Med. 1997;37:932–942.

91. Chen N, Wyrwicz AM. Removal of EPI Nyquist ghost artifacts with two-dimensional phase correction. Magn. Reson. Med. 2004;51:1247–1253.

92. Buonocore MH, Gao L. Ghost artifact reduction for echo planar imaging using image phase correction. Magn. Reson. Med. 1997;38:89–100.

93. Hennel F. Image-Based Reduction of Artifacts in Multishot Echo-Planar Imaging. J. Magn. Reson. 1998;134:206–213.

94. Foxall DL, Harvey PR, Huang J. Rapid iterative reconstruction for echo planar imaging. Magn. Reson. Med. 1999;42:541–547.

95. Buonocore MH, Zhu DC. Image-based ghost correction for interleaved EPI. Magn. Reson. Med. 2001;45:96–108.

96. Kim Y-C, Nielsen J-F, Nayak KS. Automatic correction of echo-planar imaging (EPI) ghosting artifacts in real-time interactive cardiac MRI using sensitivity encoding. J. Magn. Reson. Imaging 2008;27:239–245.

97. Van der Zwaag W, Marques JP, Lei H, Just N, Kober T, Gruetter R. Minimization of Nyquist ghosting for echo-planar imaging at ultra-high fields based on a "negative readout gradient" strategy. J. Magn. Reson. Imaging 2009;30:1171–1178.

98. Kellman P, McVeigh ER. Phased array ghost elimination. NMR Biomed. 2006;19:352–361.

99. Li H, Fox-Neff K, Vaughan B, French D, Szaflarski JP, Li Y. Parallel EPI artifact correction (PEAC) for N/2 ghost suppression in neuroimaging applications. Magn. Reson. Imaging 2013;31:1022–1028.

100. Spielman DM, Pauly JM. Spiral imaging on a small-bore system at 4.7t. Magn. Reson. Med. 1995;34:580–585.

101. Zhang Y, Hetherington HP, Stokely EM, Mason GF, Twieg DB. A novel k-space trajectory measurement technique. Magn. Reson. Med. 1998;39:999–1004.

102. Josephs O, Deichmann R, Turner R. Trajectory measurement and generalised reconstruction in rectilinear EPI. In: Proceedings of the 8th Annual Meeting of ISMRM, Denver, Colorado, USA; 2000. p 1517.

103. O'Sullivan JD. A Fast Sinc Function Gridding Algorithm for Fourier Inversion in Computer Tomography. IEEE Trans. Med. Imaging 1985;4:200–207.

104. Jackson JI, Meyer CH, Nishimura DG, Macovski A. Selection of a convolution function for Fourier inversion using gridding [computerised tomography application]. IEEE Trans. Med. Imaging 1991;10:473–478.

105. Pruessmann KP, Weiger M, Bornert P, Boesiger P. Advances in sensitivity encoding with arbitrary k-space trajectories. Magn. Reson. Med. 2001;46:638–651.

106. Man L-C, Pauly JM, Macovski A. Multifrequency interpolation for fast off-resonance correction. Magn. Reson. Med. 1997;37:785–792.

107. Birn R, Bandettini P, Cox R, Jesmanowicz A, Shaker R. Magnetic field changes in the human brain due to swallowing or speaking. Magn. Reson. Med. 1998;40:55–60.

108. Raj D, Paley DP, Anderson AW, Kennan RP, Gore JC. A model for susceptibility artefacts from respiration in functional echo-planar magnetic resonance imaging. Phys. Med. Biol. 2000;45:3809.

109. Barry RL, Williams JM, Klassen LM, Gallivan JP, Culham JC, Menon RS. Evaluation of preprocessing steps to compensate for

magnetic field distortions due to body movements in BOLD fMRI. Magn. Reson. Imaging 2010;28:235–244.

110. Hu X, Kim S-G. Reduction of signal fluctuation in functional MRI using navigator echoes. Magn. Reson. Med. 1994;31:495–503.

111. Liu H-L, Kochunov P, Lancaster JL, Fox PT, Gao J-H. Comparison of navigator echo and centroid corrections of image displacement induced by static magnetic field drift on echo planar functional MRI. J. Magn. Reson. Imaging 2001;13:308–312.

112. Versluis MJ, Sutton BP, de Bruin PW, Börnert P, Webb AG, van Osch MJ. Retrospective image correction in the presence of nonlinear temporal magnetic field changes using multichannel navigator echoes. Magn. Reson. Med. 2012;68:1836–1845.

113. Boer VO, vd Bank BL, van Vliet G, Luijten PR, Klomp DWJ. Direct B0 field monitoring and real-time B0 field updating in the human breast at 7 tesla. Magn. Reson. Med. 2012;67:586–591.

114. Duerst Y, Wilm BJ, Dietrich BE, Brunner DO, Barmet C, Schmid T, Vannesjo SJ, Pruessmann KP. Full 3rd Order Real-Time Shim Feedback for Field Stabilization and Its Application in Brain MRI at 7T. In: Proceedings of the 21th Annual Meeting of ISMRM, Salt Lake City, USA; 2013. p 669.

115. Vannesjo SJ, Wilm BJ, Duerst Y, Dietrich BE, Brunner DO, Barmet C, Pruessmann KP. Snapshot Field Monitoring Enables Correction of Slow Field Perturbations in High-Resolution Brain MRI. In: Proceedings of the 21th Annual Meeting of ISMRM, Salt Lake City, USA; 2013. p 2569.

116. Raj D, Anderson AW, Gore JC. Respiratory effects in human functional magnetic resonance imaging due to bulk susceptibility changes. Phys. Med. Biol. 2001;46:3331.

117. Barry RL, Menon RS. Modeling and suppression of respiration-related physiological noise in echo-planar functional magnetic resonance imaging using global and one-dimensional navigator echo correction. Magn. Reson. Med. 2005;54:411–418.

118. Yetkin F, Haughton V, Cox R, Hyde J, Birn R, Wong E, Prost R. Effect of motion outside the field of view on functional MR. Am. J. Neuroradiol. 1996;17:1005–1009.

119. Vannesjo SJ, Barmet C, Duerst Y, Gross S, Brunner DO, Pruessmann KP. Higher-order monitoring of physiological field

fluctuations in brain MRI at 7T. In: Proceedings of the 20th Annual Meeting of ISMRM, Melbourne, Australia; 2012. p 216.

120. Li T-Q, van Gelderen P, Merkle H, Talagala L, Koretsky AP, Duyn J. Extensive heterogeneity in white matter intensity in high-resolution T2*-weighted MRI of the human brain at 7.0 T. NeuroImage 2006;32:1032–1040.

121. Duyn JH, Gelderen P van, Li T-Q, Zwart JA de, Koretsky AP, Fukunaga M. High-field MRI of brain cortical substructure based on signal phase. Proc. Natl. Acad. Sci. 2007;104:11796–11801.

122. Fukunaga M, Li T-Q, Gelderen P van, Zwart JA de, Shmueli K, Yao B, Lee J, Maric D, Aronova MA, Zhang G, et al. Layer-specific variation of iron content in cerebral cortex as a source of MRI contrast. Proc. Natl. Acad. Sci. 2010;107:3834–3839.

123. Marques JP, Zwaag W van der, Granziera C, Krueger G, Gruetter R. Cerebellar Cortical Layers: In Vivo Visualization with Structural High-Field-Strength MR Imaging. Radiology 2010;254:942–948.

124. Mainero C, Benner T, Radding A, Kouwe A van der, Jensen R, Rosen BR, Kinkel RP. In vivo imaging of cortical pathology in multiple sclerosis using ultra-high field MRI. Neurology 2009;73:941–948.

125. Rooden S van, Maat-Schieman MLC, Nabuurs RJA, Weerd L van der, Duijn S van, Duinen SG van, Natté R, Buchem MA van, Grond J van der. Cerebral Amyloidosis: Postmortem Detection with Human 7.0-T MR Imaging System. Radiology 2009;253:788–796.

126. Pfeuffer J, Van de Moortele P-F, Ugurbil K, Hu X, Glover GH. Correction of physiologically induced global off-resonance effects in dynamic echo-planar and spiral functional imaging. Magn. Reson. Med. 2002;47:344–353.

127. Barry RL, Martyn Klassen L, Williams JM, Menon RS. Hybrid two-dimensional navigator correction: A new technique to suppress respiratory-induced physiological noise in multi-shot echo-planar functional MRI. NeuroImage 2008;39:1142–1150.

128. Van Gelderen P, de Zwart JA, Starewicz P, Hinks RS, Duyn JH. Real-time shimming to compensate for respiration-induced B0 fluctuations. Magn. Reson. Med. 2007;57:362–368.

129. Vannesjö J, Brunner D, Barmet C, Pruessmann KP. Correction of breathing-induced artefacts in high-field brain MRI using concurrent field monitoring. In: Proceedings of the 19th Annual Meeting of ISMRM, Montreal, Canada; 2011. p 284.

130. Beatty PJ, Nishimura DG, Pauly JM. Rapid gridding reconstruction with a minimal oversampling ratio. IEEE Trans. Med. Imaging 2005;24:799–808.

131. Stone SS, Haldar JP, Tsao SC, Hwu W -m. W, Sutton BP, Liang Z-P. Accelerating advanced MRI reconstructions on GPUs. J. Parallel Distrib. Comput. 2008;68:1307–1318.

132. Bieri MA, Barmet C, Wilm BJ, Pruessmann KP. Versatile higher-order reconstruction accelerated by a graphics processing unit (GPU). In: Proceedings of the 19th Annual Meeting of ISMRM, Montreal, Canada; 2011. p 2545.

133. Mason GF, Harshbarger T, Hetherington HP, Zhang Y, Pohost GM, Twieg DB. A Method to measure arbitrary k-space trajectories for rapid MR imaging. Magn. Reson. Med. 1997;38:492–496.

134. Dürst Y, Wilm BJ, Dietrich BE, Vannesjö SJ, Pruessmann KP. Real-Time Shim Feedback for Field Stabilization in Human MRI Systems. In: Proceedings of the 20th Annual Meeting of ISMRM, Melbourne, Australia; 2012. p 702.

130. Wilm BJ, Duerst Y, Dietrich BE, Wyss M, Vannesjo SJ, Schmid T, Brunner DO, Barmet C, Pruessmann KP. Feedback field control improves linewidths in in vivo magnetic resonance spectroscopy. Magn. Reson. Med. 2013;DOI:10.1002/mrm.24836.

136. Zaitsev M, Dold C, Sakas G, Hennig J, Speck O. Magnetic resonance imaging of freely moving objects: Prospective real-time motion correction using an external optical motion tracking system. Neuroimage 2006;31:1038–1050.

137. Ooi MB, Krueger S, Thomas WJ, Swaminathan SV, Brown TR. Prospective real-time correction for arbitrary head motion using active markers. Magn. Reson. Med. 2009;62:943–954.

138. Haeberlin M, Kasper L, Brunner DO, Barmet C, Pruessmann KP. Continuous motion tracking and correction using NMR probes and gradient tones. In: Proceedings of the 20th Annual Meeting of ISMRM, Melbourne, Australia; p 595.

List of Publications

Papers

Vannesjo SJ, Haeberlin M, Kasper L, Pavan M, Wilm BJ, Barmet C, Pruessmann KP. Gradient system characterization by impulse response measurements with a dynamic field camera. Magn Reson Med 2013;69:583–593.

Wilm BJ, Duerst Y, Dietrich BE, Wyss M, Vannesjo SJ, Schmid T, Brunner DO, Barmet C, Pruessmann KP. Feedback field control improves linewidths in in vivo magnetic resonance spectroscopy. Magnetic Resonance in Medicine 2013; DOI:10.1002/mrm.24836.

Vannesjo SJ, Dietrich BE, Pavan M, Brunner DO, Wilm BJ, Barmet C, Pruessmann KP. Field camera measurements of gradient and shim impulse responses using frequency sweeps. Magnetic Resonance in Medicine 2013; DOI:10.1002/mrm.24934.

Conference contributions

Vannesjö SJ, Häberlin M, Kasper L, Barmet C, Pruessmann KP. Measurement of gradient impulse response functions using a 3rd-order dynamic field camera. In: ESMRMB Book of abstracts, Antalya, Turkey, 2009. p. 667.

Vannesjö SJ, Kasper L, Pavan M, Barmet C, Pruessmann KP. On the feasibility of single-shot EPI during higher-order shim settling. In:

Proceedings of the 18th Annual Meeting of ISMRM, Stockholm, Sweden, 2010. p. 145.

Vannesjö SJ, Häberlin M, Kasper L, Barmet C, Pruessmann KP. A method for characterizing the magnetic field response of a gradient system. In: Proceedings of the 18th Annual Meeting of ISMRM, Stockholm, Sweden, 2010. p. 1536.

Pavan M, Vannesjö SJ, Barmet C, Brunner D, Pruessmann KP. Frequency-division multiplexing for concurrent imaging and field monitoring. In: Proceedings of the 18th Annual Meeting of ISMRM, Stockholm, Sweden, 2010. p. 1538.

Kasper L, Vannesjö SJ, Haeberlin M, Barmet C, Stephan KE, Pruessmann KP. Non-uniform density EPI acquisition improves the SNR of smoothed MR images. In: Proceedings of the 18th Annual Meeting of ISMRM, Stockholm, Sweden, 2010. p. 3040.

Henning A, Barmet C, Fuchs A, Vannesjö J, Boesiger P, Pruessmann KP. Characterization and correction of modulation sidebands in 1H MRS without water suppression by spatiotemporal field monitoring. In: Proceedings of the 18th Annual Meeting of ISMRM, Stockholm, Sweden, 2010. p. 3311.

Vannesjö J, Brunner D, Barmet C, Pruessmann KP. Correction of breathing-induced artefacts in high-field brain MRI using concurrent field monitoring. In: Proceedings of the 19th Annual Meeting of ISMRM, Montreal, Canada, 2011. p. 284.

Vannesjö J, Fillmer A, Barmet C, Boesiger P, Henning A, Pruessmann KP. Fast characterization of higher-order shim dynamics by impulse response measurements with a dynamic field camera. In: Proceedings of the 19th Annual Meeting of ISMRM, Montreal, Canada, 2011. p. 719.

Fillmer A, Vannesjö J, Barmet C, Boesiger P, Pruessmann KP, Henning A. Using spatio-temporal field monitoring for iterative higher order

DSU pre-emphasis calibration. In: Proceedings of the 19th Annual Meeting of ISMRM, Montreal, Canada, 2011. p. 1843.

Haeberlin M, Kasper L, Barmet C, Vannesjö SJ, Kozerke S, Pruessmann KP. Combined real-time prospective motion correction and concurrent field monitoring. In: Proceedings of the 19th Annual Meeting of ISMRM, Montreal, Canada, 2011. p. 4589.

Vannesjö J, Brunner DO, Barmet C, Pruessmann KP. Concurrent field monitoring for the correction of artefacts caused by breathing and limb motion in high-field brain MRI. In: ESMRMB book of abstracts, Leipzig, Germany, 2011. p. 374.

Fillmer A, Vannesjö SJ, Barmet C, Boesiger P, Pruessmann KP, Henning A. 3rd order DSU pre-emphasis calibration using spatio-temporal field monitoring. In: ESMRMB book of abstracts, Leipzig, Germany, 2011. p. 528.

Vannesjo SJ, Dietrich BE, Barmet C, Wilm BJ, Brunner DO, Pruessmann KP. Measurement and pre-emphasis of shim responses using frequency sweeps. In: Proceedings of the 20th Annual Meeting of ISMRM, Melbourne, Australia, 2012. p. 142.

Vannesjo SJ, Barmet C, Duerst Y, Gross S, Brunner DO, Pruessmann KP. Higher-order monitoring of physiological field fluctuations in brain MRI at 7T. In: Proceedings of the 20th Annual Meeting of ISMRM, Melbourne, Australia, 2012. p. 216.

Dürst Y, Wilm BJ, Dietrich BE, Vannesjö SJ, Pruessmann KP. Real-Time Shim Feedback for Field Stabilization in Human MRI Systems. In: Proceedings of the 20th Annual Meeting of ISMRM, Melbourne, Australia, 2012. p. 702.

Busch J, Vannesjoe SJ, Giese D, Barmet C, Pruessmann K, Kozerke S. Pre-emphasis Compensation of Oscillatory Phase Offsets in Phase-Contrast Flow Measurements. In: Proceedings of the 20th Annual Meeting of ISMRM, Melbourne, Australia, 2012. p. 1172.

Testud F, Gallichan D, Barmet C, Vannesjö J, Welz AM, Cocosco CA, Prüssmann K, Hennig J, Zaitsev M. Characterization of PatLoc Gradient with a Field Camera. In: Proceedings of the 20th Annual Meeting of ISMRM, Melbourne, Australia, 2012. p. 2598.

Fillmer A, Vannesjo SJ, Pavan M, Pruessmann KP, Boesiger P, Henning A. Echo Planar Imaging at 7T with 3rd Order Slice-Wise Dynamic Shim Update (DSU) and Full Eddy-Current Compensation (ECC). In: Proceedings of the 20th Annual Meeting of ISMRM, Melbourne, Australia, 2012. p. 2604.

Busch J, Vannesjoe SJ, Giese D, Barmet C, Pruessmann KP, Kozerke S. Pre-emphasis compensation of oscillatory phase offsets in phase-contrast flow measurements. In: ESMRMB Book of abstracts, Lisbon, Portugal, 2012. p. 119.

Klein S, Kasper L, Vannesjo SJ, Prüssmann KP. Concurrent magnetic field monitoring of EPI time series on different time scales: intra-session, inter-session and inter-day differences confounding image reconstruction. In: ESMRMB Book of abstracts, Lisbon, Portugal, 2012. p. 198.

Duerst Y, Wilm BJ, Dietrich BE, Vannesjo SJ, Barmet C, Pruessmann KP. Feedback control to address magnetic field drifts and fluctuations. In: ESMRMB Book of abstracts, Lisbon, Portugal, 2012. p. 289.

Fillmer A, Vannesjo SJ, Pavan M, Pruessmann KP, Boesiger P, Henning A. Full eddy-current compensated (ECC) dynamic shim updated (DSU) echo planar imaging (EPI). In: ESMRMB Book of abstracts, Lisbon, Portugal, 2012. p. 291.

Vannesjo SJ, Dietrich BE, Brunner DO, Wilm BJ, Barmet C, Pruessmann KP. Shim impulse response measurements using frequency-swept pulses. In: ESMRMB Book of abstracts, Lisbon, Portugal, 2012. p. 290.

Busch J, Vannesjo SJ, Barmet C, Pruessmann KP, Kozerke S. Analysis of Thermal Stability of Background Phase Errors in Phase-Contrast Flow Imaging. In: Proceedings of the 21th Annual Meeting of ISMRM, Salt Lake City, USA, 2013. p. 69.

Wilm BJ, Duerst Y, Dietrich BE, Wyss M, Brunner DO, Barmet C, Schmid T, Vannesjo SJ, Pruessmann KP. Higher-Order Feedback Field Control Improves Linewidths in MR Spectroscopy at 7T. In: Proceedings of the 21th Annual Meeting of ISMRM, Salt Lake City, USA, 2013. p. 529.

Graedel NN, Vannesjo SJ, Kasper L, Gross S, Dietrich BE, Barmet C, Pruessmann KP. Image Reconstruction Using the Gradient Impulse Response for Trajectory Prediction. In: Proceedings of the 21th Annual Meeting of ISMRM, Salt Lake City, USA, 2013. p. 552.

Duerst Y, Wilm BJ, Dietrich BE, Brunner DO, Barmet C, Schmid T, Vannesjo SJ, Pruessmann KP. Full 3rd Order Real-Time Shim Feedback for Field Stabilization and Its Application in Brain MRI at 7T. In: Proceedings of the 21th Annual Meeting of ISMRM, Salt Lake City, USA, 2013. p. 669.

Vannesjo SJ, Dietrich BE, Pavan M, Barmet C, Pruessmann KP. Digital Cross-Term Pre-Emphasis for Higher-Order Dynamic Shimming. In: Proceedings of the 21th Annual Meeting of ISMRM, Salt Lake City, USA, 2013. p. 671.

Vannesjo SJ, Wilm BJ, Duerst Y, Dietrich BE, Brunner DO, Barmet C, Pruessmann KP. Snapshot Field Monitoring Enables Correction of Slow Field Perturbations in High-Resolution Brain MRI. In: Proceedings of the 21th Annual Meeting of ISMRM, Salt Lake City, USA, 2013. p. 2569.

Klein S, Kasper L, Vannesjo J, Häberlin M, Gross S, Dietrich B, Prüssmann KP. Concurrent Magnetic Field Monitoring of EPI Time Series: Characterizing Encoding Field and Image Fluctuations Using Principal Component Analysis. In: Proceedings of the 21th Annual Meeting of ISMRM, Salt Lake City, USA, 2013. p. 2715.

Curriculum Vitae

Signe Johanna Vannesjö
Date of Birth: 2nd Nov. 1981
Citizenship: Swedish

Education

2008-2013   PhD candidate
             Supervisor: Prof. Klaas P. Pruessmann
             Institute for Biomedical Engineering, Deptartment of
             Information Technology and Electrical Engineering
             ETH Zurich, Zurich, Switzerland

2000-2008   University Medical Degree
             Karolinska Institutet, Stockholm, Sweden

2002-2007   MSc, Engineering Physics
             KTH, Stockholm, Sweden

1997-2000   High school
             Rudbeckianska Upper Secondary School, Västerås,
             Sweden

1999   Doshisha International High School, Kyoto, Japan
             Exchange year at high school level

Work & research projects

2008	Neuroradiology
	6 months working as a junior resident
	Karolinska University Hospital, Stockholm, Sweden
2008	Elective project within medical studies:
	Diffusion tractography of crossing fibre tracts in the developing brain
	Supervisor: Serena Counsell
	Imperial College, London, UK
2007	Diploma thesis, engineering physics:
	LARIS - a modern laser resonance ionization spectroscopy lab in development
	Supervisor: Lars-Erik Berg
	Dept. of Applied Physics, KTH, Stockholm, Sweden
	In collaboration with CERN, Geneva, Switzerland
2003-2004	Research assistant, project on influence of steroids on bone growth
	Supervisor: Prof. Lars Sävendahl
	Deptartment of Women's and Children's Health
	Karolinska Institutet, Stockholm, Sweden
2001-2002	Research assistant, projects on epilepsy and olfaction
	Supervisor: Ivanka Savic
	Department of Neuroscience
	Karolinska Institutet, Stockholm, Sweden
Languages	Swedish (native), English (fluent), German (good), Japanese (conversational)
Interests	Swing dances, Skiing, Hiking, Music, Literature

Acknowledgments

This thesis would never have seen the light of day without the contribution of a great number of people and I am much indebted to all those who have assisted me with the work, as well as all those who helped making the journey a pleasant one.

First and foremost I am deeply grateful to my PhD supervisor, Klaas Pruessmann, who provided me with an opportunity to join his group. I highly appreciate the collegial and scientifically minded atmosphere in the group and have always benefited from his guidance and support. Many thanks also go to the co-referee, Prof. Robert Turner, for taking his time to read the thesis and to provide insightful comments and suggestions for improvements.

To no lesser degree, I want to thank my office mates - Max, Lars and Giorgos - for making it a joy to go to work. These years wouldn't have been the same without all those wide-ranging discussions on science, society, and life in general, and I consider myself lucky to work in an environment where my colleagues are also my friends. Max and Lars were also great company while taking our first steps into the world of field monitoring.

I would hardly have been making my way forward through the thesis projects without extensive assistance in mastering the art of field